Multipactor in Coaxial Transmission Lines

by

Stephen Volosov Langellotti

A dissertation submitted in partial fulfillment
of the requirements for the degree of
Doctor of Philosophy
(Nuclear Engineering and Radiological Sciences)
in the University of Michigan
2023

Doctoral Committee:

Professor Ronald M. Gilgenbach, Co-Chair
Associate Research Scientist Nicholas M. Jordan, Co-Chair
Professor Igor Jovanovic
Professor Emeritus Yue Ying Lau
Professor Kamal Sarabandi
Associate Professor Peng Zhang, Michigan State University

Stephen Volosov Langellotti
svlangel@umich.edu
ORCID iD: 0000-0002-3266-7622

DEDICATION

For Jessica. I hope it was worth the wait.

ACKNOWLEDGMENTS

When I finally sat down and started writing this dissertation, I knew that it would only have one author's name; it is supposed to be a statement of all of my achievements during my time at the University of Michigan. However, anyone who has gone through this process knows that no dissertation is the product of just one man. In truth, there have been many people who have helped me over the years. I'd like to take this time to briefly acknowledge the assistance they have given me. I would first like to thank my advisors, Prof. Ronald Gilgenbach, Prof. Y.Y. Lau, and Dr. Nicholas Jordan. Thank you, not only for giving me this opportunity, but also for all of your advice and instruction. More than anything else, I thank you for your patience. You have always been willing to work for me, especially during these last couple years when I frequently needed to travel out of state. Your flexibility as advisors shows that you truly believe that when the students come first, our research will excel.

I have worked with many fantastic students during my time at the University of Michigan. Each of these students have provided a sense of community within Beamteam that made our lab a joy to work in. I give my thanks to Dr. Foivos Antoulinakis, Adam Brusstar, Dr. Paul Campbell, Joseph Chen, George Dowhan, Dr. Steven Exelby, Emma Guerin, Dr. Abhijit Jassem, Dion Li, Stephanie Miller, Dr. Drew Packard, Ryan Revolinsky, Dr. Akash Shah, Trevor Smith, Brendan Sporer, Chris Swenson, Sunkeerth Tummala, Donovan White, Levi Welch, Dr. Patrick Wong, Dr. Jeffrey Woolstrum, and Grant Young. Thank you for working with me and making me a part of the group.

I want to highlight the assistance Adam Brusstar has given me. Adam, you have been an extremely valuable resource for me over these last few months. Though our partnership had begun as a simple training program for you to inherit the multipactor experiment, it turned into so much more. Over this last summer, you have helped me rebuild every component in my experiment and troubleshoot issues with the Scandinova. Often, you were the only reason I could ever take a break and get the rest I so sorely needed. Thank you for everything. Without you, this last year would have taken twice as long.

I'd like to highlight a few of my fellow students who have taught me how to use several of the technologies that were essential for running my experiments. Thank you, Brendan, for teaching me about designing Arduino-based control systems and 3D-printing. My discussions with you were

invaluable when I was designing the controller for my variable attenuator. I also want to thank Ryan Revolinsky for teaching me that I should not always buy the cheapest components available; your suggestion to use the STR-3 stepper motor controller proved to be far more reliable than the generic boards I had used before. Finally, I want to thank Drew for teaching me how to use CST Particle Studio. Your initial lessons on CST became the foundation for all of the simulations in this dissertation.

I have faced many challenges while working on this project. Aside from the backdrop of a global pandemic, I have dealt with issues ranging from a temporary loss in funding to a myriad of equipment failures. I thank Prof. Gilgenbach for helping me work through each of these challenges. When my original contract was canceled, he found alternative sources of funding so I could continue my work at the university as I waited for the new project to be approved. He also showed me infinite patience as I dealt with my many technical challenges. When the Stanford modulator—a venerable relic from the 1950s—failed and my experiment seemed doomed, Prof. Gilgenbach did not let that be the end. Even though it cost as much a new car, he used his research incentive funds to purchase the Scandinova modulator. Without this machine, I would never have been able to complete this work. I'd also like to thank Doug Eaton from Scandinova for providing the modulator's control software, even though we had purchased the device from an unaffiliated third party.

I am grateful for the friends that I have made during my time in Michigan. In particular, I'd like to thank my Dungeons and Dragons group for keeping things interesting over the last few years and providing me support in both the real and fantasy worlds. Chris, other Chris, Katie, Sunny, and Tim, thank you for everything.

Finally, I'd like to thank my family for always supporting me. My parents have always been there for me. Whenever things seemed hopeless, my parents have always been ready to give me whatever help I needed. I also want to thank my brother, David, for always reminding me that I can always reach higher. And last, but certainly not least, I thank my wife, Jessica. Ever since I met you, you have always been at my side. You are the stone that supports me. I could never have done it without you.

This research was supported by the AFOSR MURI Grant Nos. FA9550-18-1-0062 and FA9550-21-1-0367 through Michigan State University, by L3Harris Electron Devices Division, and the Directed Energy Professional Society graduate student scholarship. The authors also acknowledge financial support from the University of Michigan College of Engineering and technical support from the Michigan Center for Materials Characterization.

TABLE OF CONTENTS

LIST OF FIGURES

FIGURE

LIST OF TABLES

TABLE

LIST OF APPENDICES

LIST OF ACRONYMS

ADAM Atomic Diffusion Additive Manufacturing

EMT Electron Multiplier Tube

MURI Multi-University Research Initiative

SEM Scanning Electron Microscopy

SEY Secondary Electron Yield

SLM Selective Laser Melting

TWT Traveling Wave Tube

VNA Vector Network Analyzer

XEDS Energy-Dispersive X-Ray Spectroscopy

ABSTRACT

In vacuum systems where conducting or dielectric surfaces are exposed to oscillating electric fields, multipactor discharges carry the potential to significantly disrupt normal and efficient operation. Multipactor breakdown occurs when free electrons are accelerated into transmission line surfaces and undergo secondary electron emission. These secondary electrons can then repeat this process and multiply, allowing the system to develop into a growing electron discharge. Preventing multipactor is essential for ensuring long-term, efficient operation of vacuum electronic systems. At the University of Michigan, we have developed an S-band (3.05 GHz), coaxial multipactor test cell that operates in a new, high-fd regime, where f is the signal frequency and d is the gap spacing. This test cell is used to characterize multipactor discharges and to test methods for suppressing multipactor.

Multipactor relies on a resonance between the electron motion and the oscillating electric field. In rectangular geometries, this resonance condition can be solved analytically and then used to generate rough approximations of the breakdown threshold (the minimum power level necessary to sustain multipactor). However, in coaxial systems this resonance is more difficult to represent theoretically. While there are several theoretical models for coaxial multipactor, they are computationally expensive, and their implementation is often impractical. To aid in the design of the multipactor test cell, we have used electromagnetic-particle-in-cell (EM-PIC) simulations to characterize the multipactor discharges and provide predictions of the experimental test cell's susceptibility to multipactor.

Initial experiments explored the multipactor self-conditioning phenomenon. During multipactor, electrons bombard the transmission line surfaces, processing oxide layers and releasing trapped gases. This can reduce secondary electron emission and increase the multipactor breakdown threshold. This process also enabled our experimental hardware to more closely match the SEY model we assumed in our PIC simulations. After fully conditioning the transmission line surfaces, the experimental measurements of the breakdown threshold agreed with our predictions to within 10–15%. We also found that that the multipactor self-conditioning process is relatively rapid when considering the cumulative timescale of the multipactor discharges.

Multipactor cannot be allowed to occur in vacuum electronic systems; it will disrupt normal signal transmission and can potentially lead to catastrophic failure. The key to preventing mul-

tipactor is to suppress secondary electron emission. One method explored here relies on using textured materials. Textured surfaces can trap secondary electrons and inhibit multipactor. Traditional manufacturing techniques cannot be easily used to produce a textured coaxial transmission line.

We explored whether 3D-printing processes—which are inherently textured—can be used to produce multipactor-resistant components. We experimentally tested two partially 3D-printed coaxial transmission lines—each manufactured using either Selective Laser Melting (SLM) or Atomic Diffusion Additive Manufacturing (ADAM)—to demonstrate proof-of-concept. Before our experimental investigation, we used a Monte-Carlo algorithm to predict the modification of the secondary electron yield due to surface roughness; these data were then used to run multipactor PIC simulations. Our experimental measurements consistently outperformed the simulations. The 3D-printed transmission lines were extremely effective for preventing multipactor. In particular, the ADAM-printed outer conductor nearly doubled the breakdown threshold power at our low-fd limit. These experiments suggest that 3D-printed, textured, coaxial transmission lines could act as drop-in replacements in existing devices and provide valuable microwave power margin from multipactor onset.

CHAPTER 1

Introduction and Theory

The peak power limits in all electronic systems are ultimately defined by breakdown. This is true for components at every level of complexity; extremely high voltages may punch through small resistors while microelectronics may be damaged by a modest power surge. In RF and microwave systems, particularly in passive components such as transmission lines or dielectric windows, high-power oscillating fields can promote various forms of plasma breakdown. At high pressure, this may lead to conventional gas discharges and quasineutral plasmas. Vacuum electronic systems, however, may need to contend with a different phenomenon: multipactor.

Multipactor is a form of resonant RF breakdown that occurs in vacuum systems [1]. Oscillating electric fields accelerate unbound electrons into surfaces where they may undergo secondary electron emission. If the electrons strike the surfaces with sufficient energy, they will multiply by secondary electron emission, and the electron density will grow rapidly. The continued bombardment of electrons against the surfaces can result in potentially dangerous effects.

When a device undergoes multipactor, its operation will be disrupted by a combination of three effects: the rapid growth of space charge, the loss of energy to the accelerating electrons, and the energy deposited by the electron bombardment. The growing cloud of space-charge can de-tune RF cavities [2] and disrupt coupling structures in particle accelerators [3, 4]. In communications systems, the signal quality will be damaged and data may be lost [5]. When the electrons are accelerated, they consume energy from the RF drive signal and reduce the device's overall efficiency [1]. This energy is then deposited into the structure's wall, potentially leading to uncontrolled increases in temperature [1] and even catastrophic failure of the device [6, 7].

Preventing multipactor is essential for reliable, long-term operations of vacuum electronic devices. Unfortunately, predicting when multipactor will occur is not a trivial matter. Theoretical representations may be extremely simplified [1] or depend on nonphysical assumptions [8, 9]. Analytic models are limited to planar geometries; other systems, such as coaxial transmission lines, are forced to rely on highly approximate solutions [10]. More robust theories based on statistical analyses [11] or nonlinear dynamics [12] are difficult to implement and require significant numerical computations.

Because multipactor is so difficult to represent theoretically, simulations are often used to generate more realistic predictions. Secondary electron emission is not particularly well characterized and is extremely dependent on material properties. As a result, comparing simulations to experiments relies on a realistic representation of the device's surface characteristics. Since this is not always possible, experiments are necessary to confirm any predictions about multipactor. This is particularly true when testing multipactor suppression technologies; many of these techniques are based on modifications to the surfaces' secondary electron yield.

This work presents an experimental platform for researching multipactor in a coaxial transmission line. This test cell was developed as part of a multi-university research initiative (MURI) to study multipactor in all its forms. This collaboration also includes test cells for rectangular [13] and microstripline [14] geometries. Each of these experimental platforms share a goal to validate newly developed theoretical models and demonstrate methods for eliminating multipactor.

Previous coaxial multipactor experiments have generally been limited to RF-frequencies below 1 GHz. The two classic coaxial multipactor experiments by Woo [15] and Graves [16] both operated in the lower half of the VHF and HF bands (10–150 MHz). More recent experiments have been performed in higher frequency bands, though many have been limited to L-band operations [17–19] or lower [20]. S-band experiments [21] (and coaxial multipactor experiments in general [15, 16, 20]), have been limited to cases with $fd < 5\ \mathrm{GHz} \cdot \mathrm{mm}$, where f is the frequency and d is the gap spacing[1]. Few, if any, experimental investigations have explored multipactor with high fd. The coaxial multipactor test cell presented in this work, and previously described in [22], operates at S-band frequencies (3.05 GHz) and $fd > 4.8\ \mathrm{GHz} \cdot \mathrm{mm}$. This will facilitate multipactor research in a regime that has never been explored.

After a brief overview on multipactor theory, this dissertation will discuss simulations and experiments on characterizing multipactor in a coaxial transmission line. Following this work, we will present a model for the secondary electron yield from 3D-printed, textured surfaces. Finally, we will present experimental results demonstrating proof-of-concept for suppressing multipactor with a 3D-printed transmission line.

1.1 Multipactor Fundamentals

The classical representation of multipactor is as a resonance between electron motion and RF electric fields. There are two basic forms of multipactor, depending on the arrangement of the transmission line surfaces. We will begin with two-surface multipactor, which is typically considered to occur on conductive surfaces [1].

[1] According to the classical theory, which we will discuss in Sec. 1.3, fd is one of the primary scaling parameters for multipactor.

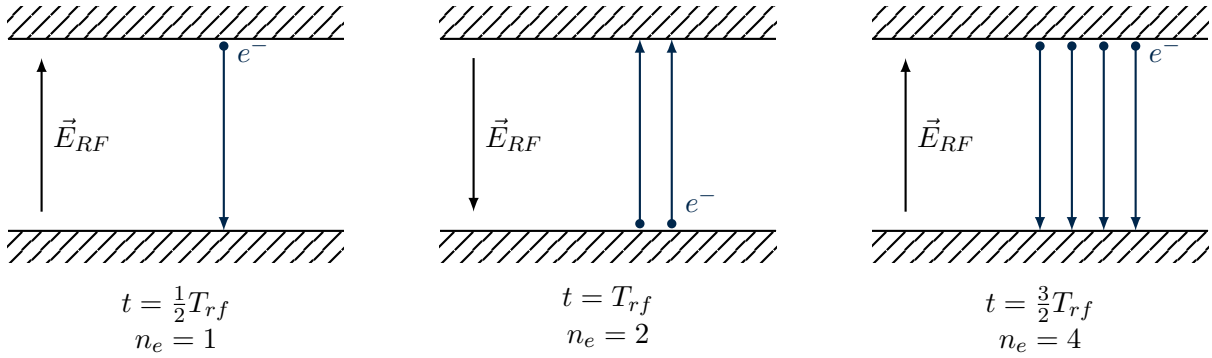

Figure 1.1: Illustration of a two-surface multipactor discharge.

Consider two conductive, parallel plates suspended in vacuum, as illustrated in Fig. 1.1. An oscillating electric field, with some frequency f exists between the two conductors. Now, let us assume that a single electron[2] is born near the top surface at time $t = 0$. For simplicity, we assume that the electron appears exactly when the electric field begins to point upward, so the electron is accelerated toward the lower surface. After impacting the surface, the electron undergoes secondary electron emission and some number of electrons are emitted; for simplicity, let us assume that there are two secondary electrons.

If the original electron's transit time was exactly half an RF-period,[3] then the electric field will be reversed. The two secondary electrons will be accelerated back to the upper surface where they will impact and emit four new electrons. This process will repeat every half RF-cycle, and the electron population will double after each generation. For a 1-GHz drive signal, this is an extremely rapid process. A single seed electron would (in the absence of any feedback effects) multiply to 1.13×10^{15} (2^{50}) in only 25 ns (50 doublings). A multipactor discharge will never reach this scale as space-charge effects will interfere with the electron motion well before it ever reached that point. A combination of space-charge and cavity loading effects will halt the rapidly growing electron cloud, and the multipactor discharge will reach saturation [23].

The second form of multipactor occurs over a single, dielectric surface [24][4]; this is illustrated in Fig. 1.2 which shows an oscillating electric field passing through a dielectric window. When an electron is emitted from the surface, it carries away a small amount of charge. In two-surface multipactor discharges, this charge is replenished immediately due to the surfaces' high conductivity.

[2]The source of the electron is not important. Many natural processes can generate this initial seed electron, including cosmic radiation or spontaneous field emission.

[3]Strictly speaking, the resonance condition only requires the travel time to be an odd number of RF half-cycles; the number of half-cycles defines the order of the multipactor discharge.

[4]Single surface multipactor can also occur on conductive surfaces, particularly in non-planar geometries such as in coaxial transmission lines. However, the electron dynamics more closely resemble two-surface multipactor, and can be considered a special case. This will be discussed in further detail in Sec. 1.4 when we examine the multipactor's chaotic behavior.

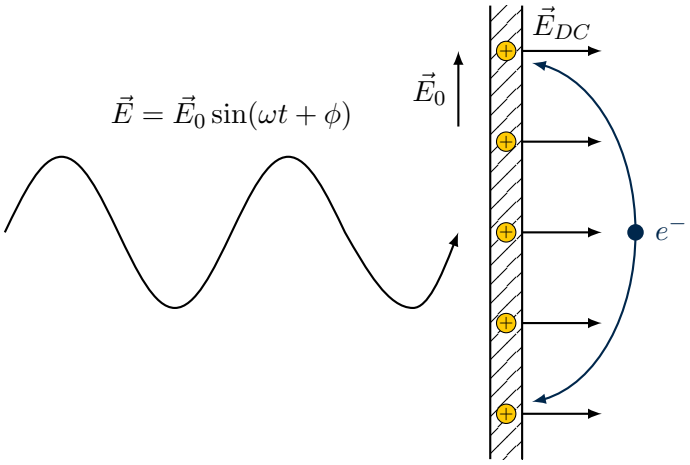

Figure 1.2: Illustration of a single-surface multipactor discharge.

Since dielectrics are poor conductors, the window will now retain a small, positive electrostatic charge. This creates a DC electric field pointing away from the surface that will pull the electrons back.

The DC electric field provides very little energy to the unbound electrons. However, since the RF signal is passing through the dielectric, the oscillating electric field, $\vec{E}_0$, is parallel to the surface. As a result, the multipactor electrons gain the bulk of their energy when they are accelerated across the surface. If the RF fields are sufficiently strong, each electron will emit several secondary electrons after impacting the surface, and the discharge will grow.

Multipactor is most dangerous on dielectric materials because single surface multipactor discharges are extremely localized. As a result, all of the RF energy that is absorbed by the electrons will be deposited over a small surface area. This will lead to rapid, uncontrolled increases in temperature. If the dielectric is polymer based, it may deform or melt. Ceramic windows (such as alumina), on the other hand, may crack or shatter [6, 25]; when this happens, the vacuum seal is broken and the device is (often irreparably) damaged. This is particularly troublesome for diamond windows because of their high cost.

Although multipactor can be extremely dangerous, it can only occur under certain circumstances. The parameter space that supports multipactor is represented by a susceptibility diagram. For two-surface multipactor discharges, susceptibility diagrams plot the RF voltage, V_{rf} as a function of the product of the frequency, f, and the gap spacing, d, between the conductors.[5] An example of this is shown in Fig. 1.3. These data are from Woo's classic experiment on coaxial multipactor [15].

[5]The ratio, $d/\lambda = fd/c$, of the gap spacing to the wavelength, λ, can be used as a nondimensional alternative to fd. However, fd is convenient because it appears in the fixed phase relation when using the classical representation of multipactor and the gaps involved are a small fraction of the wavelength. The experiments we will discuss in this dissertation fall in a range of $4.84 \leq fd \leq 7.63$ GHz $\cdot$ mm, or $1.62 \times 10^{-2} \leq d/\lambda \leq 2.54 \times 10^{-2}$.

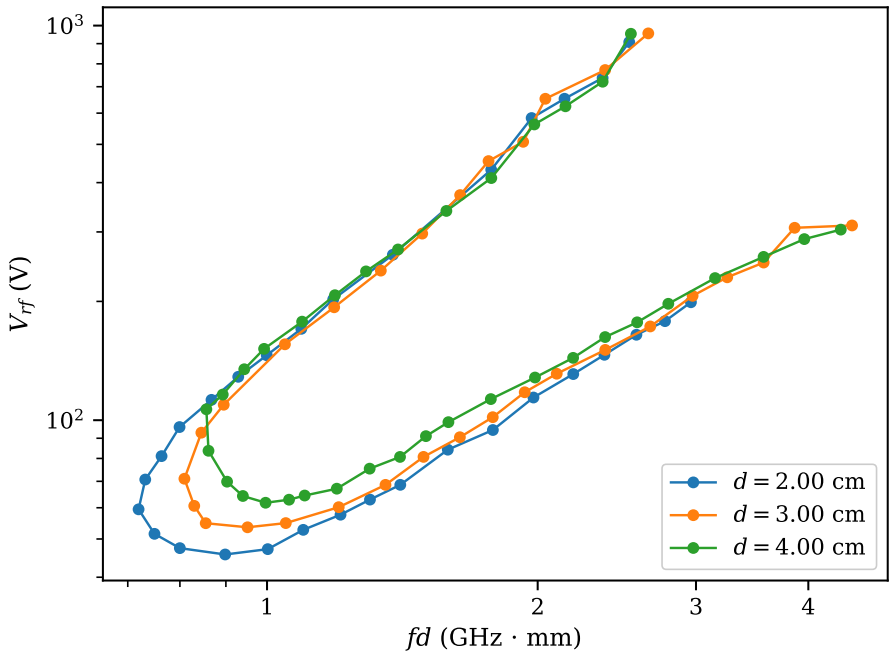

Figure 1.3: An example of a typical multipactor susceptibility diagram. Multipactor discharges can occur when the RF voltage is within this U-shaped curve. These experimental data are from Woo [15] and represent a 50-Ω, characteristic impedance coaxial transmission line.

The lower bound of the curve also represents the breakdown threshold voltage: the minimum RF voltage to sustain multipactor.[6]

Two main factors control a system's susceptibility to two-surface multipactor. The first condition is based on the resonance between the electrons and the RF signal. During multipactor, electron emission will tend to converge towards a single phase relative to the oscillating electric field. This fixed phase is defined by the geometry and the RF voltage. However, only some of these phases are stable [1]. This places upper and lower bounds on V_{rf} at a particular value of fd. This resonance condition will be discussed further in Sec. 1.3.

Multipactor is further constrained by the conductors' secondary electron yield (SEY); multipactor can only grow if each electron impact results in the emission of more than one secondary electron. The SEY is dependent on the energy and angle at which the primary electron hits the surface. Although it is material dependent, the SEY, δ, follows a general trend, which is illustrated in Fig. 1.4. As the impact energy, E, rises beyond a threshold, E_0, the SEY increases rapidly until it reaches a maximum and drops off in a long tail. This leads to the SEY curve's two most important features:

[6]The breakdown threshold can also be expressed in units of power. We will use this definition when we discuss the majority of our experimental results.

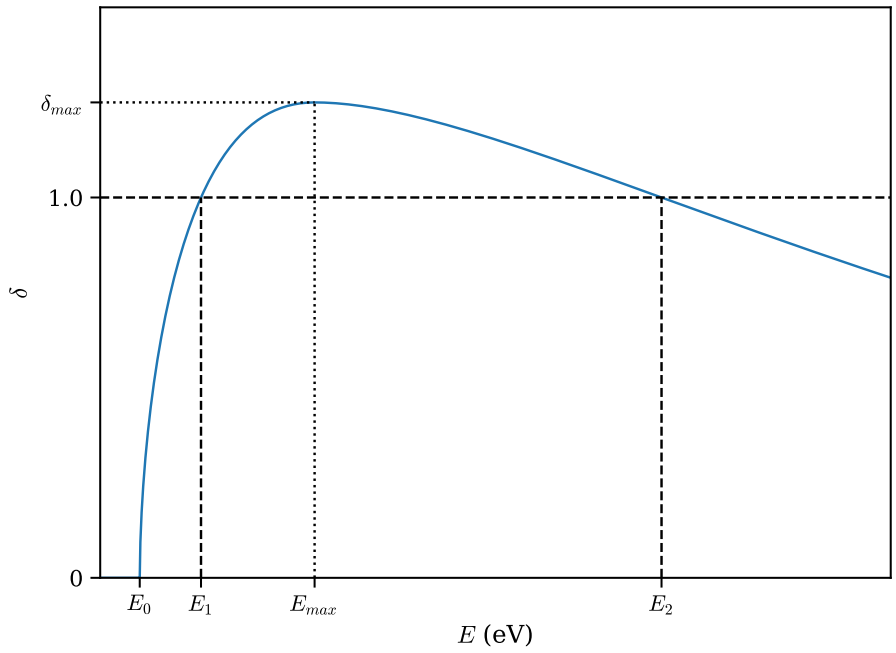

Figure 1.4: Illustration of a typical secondary emission yield curve based on the Vaughan SEY model.

the first and second crossover points, E_1 and E_2, at which $\delta = 1$.

The crossover points represent the range of impact energies that will result in the emission of more than one secondary electron. This places a further limit on multipactor: multipactor can only occur if electrons impact at energies higher than E_1 and lower than E_2, regardless of whether or the electron motion is stable. As a result, if V_{rf} is very low, then the electrons will not gain enough energy to reach the first crossover point; this causes the U-shaped bend in Fig. 1.3. Conversely, extremely high power systems cannot undergo multipactor because the electrons are accelerated far beyond the second crossover point.

The SEY curve in Fig. 1.4 is based on the original Vaughan model [26, 27]. This semi-empirical model generally provides good agreement with experimentally measured SEY data. It does not, however, provide any information for impact energies below E_0. Primary electrons below this cutoff cannot trigger the release of "true" secondaries. However, they may instead be reflected back into the vacuum. The Vaughan model can be modified to assume that some fraction of these low-energy electrons are reflected by the surface [28]. In the original model, the value for the energy threshold, E_0, was chosen arbitrarily; the modified Vaughan model instead selects E_0 iteratively such that the first crossover point, E_1, is a particular value[7].

[7]Although it is still an arbitrary choice, the first crossover point, E_1, is a more convenient control parameter than E_0 because it more directly affects multipactor susceptibility.

The modified Vaughan model is widely used in recent multipactor research [5, 11, 12, 29, 30], primarily because its implementation is extremely simple. A more robust model, developed by Furman and Pivi [31], considers three distinct modes for secondary electron emission. However, this semi-empirical model is difficult to implement and relies on 44 fitting parameters. Very few sets of these parameters exist; the present author is only aware of the two datasets[8] provided by Furman and Pivi in their original publication [31].

1.2 History of Multipactor

Unlike many other natural phenomena, multipactor was not discovered;[9] it was invented. Today, we generally treat multipactor as a problem that must be eliminated. However, in the 1930s multipactor was the solution to one of Philo Farnsworth's biggest problems [32, 33]. The original television camera was based on an "image dissector tube". These tubes converted incoming light to electronic signals. The earliest versions of these tubes produced extremely weak signals; their photocathodes emitted tiny electron currents. Although these were strong enough to demonstrate the transmission of simple images (single lines), Farnsworth needed a high efficiency, high bandwidth electron amplifier if he ever wanted to make a usable television.

Farnsworth wanted to use secondary electron emission, which had only recently been discovered, as a multiplication mechanism inside an electron amplifier [33, 35, 36]. Figure 1.5 shows a simplified illustration of the concept driving Farnsworth's original amplifier tube. This simplified tube uses two sets of electrodes. Electrons are initially generated from incoming photons interacting

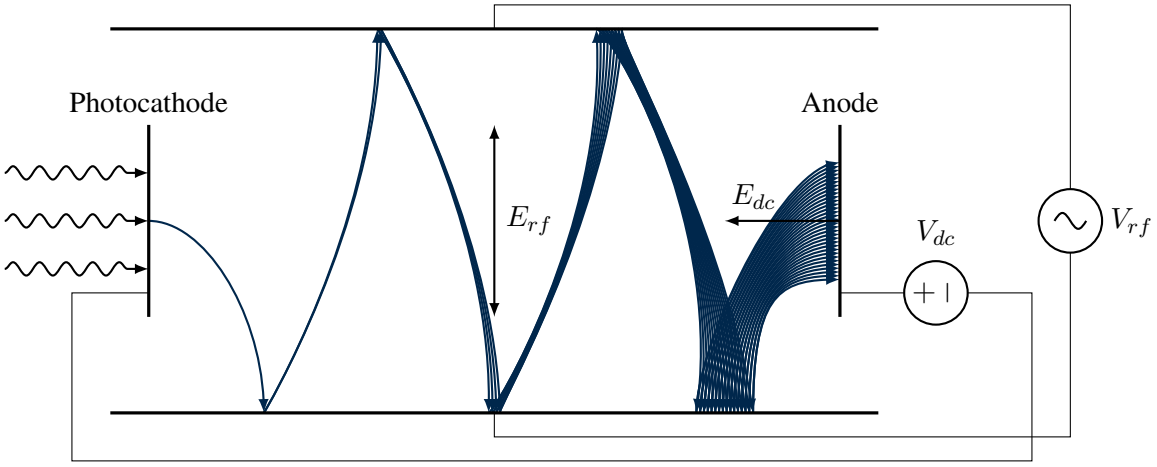

Figure 1.5: Simplified illustration of Philo Farnsworth's multipactor amplifier tube.

[8]For copper and stainless steel.

[9]Although it was first observed in 1924 by the Guttons, their results were not attributed to multipactor until the 1950s [8, 9, 34], two decades after Farnsworth developed his multipactor amplifier.

with the photocathode. A DC potential causes these electrons to drift towards the anode. As the electrons drift across the tube, the oscillating RF electric field accelerates them towards the upper and lower electrodes where they undergo secondary electron emission. This multiplies the electron current before it is collected at the anode.[10] This efficient gain mechanism enabled Farnsworth's image dissector tubes to produce usable television signals [32, 33]. And thus, the AC electron multiplier, or *multipactor*, was born.

By the 1940s, Farnsworth's dissector tubes were largely supplanted by Zworykin's Iconoscope, and multipactor amplifiers struggled to find any long-term applications [1]. At this point, multipactor began to refer to the phenomenon rather than the device. Continued research led to the earliest theories on the mechanics driving multipactor. In 1943, Danielsson proposed a theory based on the resonance between the RF drive signal and the secondary electron motion [8]. This theory, which assumed secondary electrons were emitted with zero kinetic energy, contained early descriptions of the phase focusing and stability mechanisms [34].

In 1948, Gill and von Engel conducted one of the first systematic multipactor experiments [43] and proposed their own resonance-based description for multipactor. This formulation was based on the parameter k—defined as the ratio of the electrons' emission and impact velocities—which they assumed to be constant. Although the formulation proposed by Gill and von Engel had poor correlation to experiments, their constant-k condition was later adopted by Hatch and Williams in the 1950s who developed a robust theory for multipactor [8, 9].

The Hatch and Williams formulation became the basis of classical multipactor for the next thirty years. It contained many of the features of later theories, such as the fixed phase relation, and provided formulations for the multipactor breakdown threshold [8]. In their later extension, Hatch and Williams also provided the first detailed description of higher order multipactor modes [9]. However, this theory still relied on the constant-k assumption. Values for k were chosen arbitrarily to provide the best fit between experimental and theoretical data. Although these assumptions are non-physical, they remained in use for decades due to the ease of their implementation [34].

In the 1960s through the 80s, continued experiments were performed to advance our understanding of multipactor. These experiments include Woo's investigation [15] of multipactor in coaxial transmission lines, which would later become the basis for many modern works, including Graves's 2006 dissertation [16] and the simulations presented in this thesis. At this time, Vaughan began investigating multipactor due to the discharges he observed in magnetrons and klystrons. He and other researchers began to note that multipactor can cause significant damage to RF structures; in particu-

[10]This mode of operation acts like an AC version of the photomultiplier tubes (PMTs) used with scintillation crystals for detecting ionizing radiation. Farnsworth's patents even included designs for multipactor amplifiers that only used DC electric fields [33, 37], but amplifiers that more directly resemble modern PMTs were developed by his rival, Zworykin [38, 39], at the Radio Corporation of America based on earlier designs by Slepian [40], Jarvis [41], and Iams and Salzberg [42].

lar, multipactor was found to be responsible for electrons fracturing dielectric windows [6, 7, 25]. Multipactor can absorb significant quantities of RF energy, leading to uncontrollable heat-up [44] which may eventually reach extreme temperatures that may melt or deform components [1].

To better combat multipactor, Vaughan abandoned the constant-k theory to develop a new model based on first principles [1]. This model, which considers monoenergetic emission of secondary electrons, would become the basis of the modern representation of classical multipactor. Vaughan used a phase-focusing based approach to develop predictions for the multipactor breakdown threshold. He also proposed an early model of multipactor saturation [1].

In the 1990s, a number of researchers adopted Vaughan's multipactor model. Riyopoulos, Chernin and Dialetis extended Vaughan's model to account for crossed magnetic fields [45] and for randomized delay-times and emission energies for secondary electrons [46]. At the University of Michigan, Kishek and Lau developed a model for the interaction between multipactor and RF cavities, finding that saturation is primarily caused by cavity loading and detuning [23]. Other theories that were developed during this time period include a phase focusing mechanism based on the interaction between opposing sheets of electrons [47]. Finally, Kishek and Lau developed the first comprehensive theory for single surface multipactor [34]. Single-surface, dielectric multipactor discharges were later investigated experimentally at the University of Michigan by Anderson [48, 49].

At the beginning of the twenty-first century, multipactor research began to focus on geometries outside of planar systems. So far, the majority of experiments, and virtually all of the theoretical models, focused entirely on planar geometries. A renewed interest in coaxial multipactor, coupled with advancements in computing technology, led to several numerical studies [50, 51]. In 2006, these were followed by Graves's coaxial multipactor experiment [16, 52]. The next year, Udiljak *et al.* [10] proposed an approximate analytic model for coaxial multipactor. This model would later be extended to include space-charge effects [53] and angular momentum [54].

Theoretical multipactor research has begun to move away from the classical model. This shift is largely because the classical theory, as outlined in Sec. 1.3 below, does not account for distributed electron emission energies or the effects due to low-energy backscattered electrons. There are two forms of modern multipactor theory. The first is based on nonstationary statistical analysis [11, 55]. Instead of forcing an assumption of monoenergetic electron energies, these statistical methods use nonuniform emission energies and replace the discrete phase analysis with probability distribution functions.

The discovery of ping-pong and high periodicity multipactor modes suggested that multipactor is inherently chaotic [30]. This led to a second advanced theory for multipactor. By throwing away all assumptions regarding electron motion (except the removal of space-charge effects), Siddiqi and Kishek developed an entirely new representation of multipactor based on the principles of nonlinear

dynamics and chaos theory. Because this model makes virtually no assumptions, it can be used to describe almost any form of multipactor discharge [12, 56–61]. The only requirement is that there must be a simple mechanism by which additional phenomena can be parameterized. We will discuss this chaos theory representation of multipactor further in Sec. 1.4.

Although multipactor research continues across the globe, we highlight the current nationwide effort, of which we are a part, that is underway in the United States. This multi-university research initiative (MURI), sponsored by the Air Force Office of Science Research, represents a unified effort to study multipactor. As a part of this joint effort, experimental test beds have been developed to analyze multipactor discharges in various geometries: rectangular waveguides at Texas Tech University [13]; microstriplines at the University of Wisconsin [62]; and our present work on coaxial transmission lines at the University of Michigan [22]. Additional work on characterizing secondary electron emission is being performed at the University of New Mexico [63, 64], and theoretical models are being developed at Michigan State University [5, 65, 66] and the University of Michigan [67, 68].

1.3 Classical Multipactor Theory

The classical theory of multipactor is based on the resonance between the oscillating electric field and the electrons' motion. We will focus our discussion on the simple model developed by Vaughan in 1988 for describing multipactor between two conductive parallel plates [1].

Consider two parallel plates at $x = 0$ and $x = d$. An RF voltage, V_{rf}, is applied between the two plates with frequency ω. This generates an electric field with equation

$$E(t) = -\frac{V_{rf}}{d}\sin(\omega t). \tag{1.1}$$

We use the negative sign so that at time $t = 0^+$, an electron will be accelerated in the positive x-direction. This electron appears at $x = 0$ at a phase $\omega t = \theta$ relative to the electric field. Its equation of motion is then

$$\frac{d^2x}{dt^2} = \frac{dv}{dt} = -\frac{q_e V_{rf}}{m_e d}\sin(\omega t) \tag{1.2}$$

where m_e and $q_e = -e$ are the electron mass and charge, respectively. If we assume the electron had some initial velocity v_0, then the initial conditions are

$$x(\omega t = \theta) = 0 \tag{1.3}$$

and

$$\frac{dx}{dt}(\omega t = \theta) = v(\omega t = \theta) = v_0. \tag{1.4}$$

Integrating (1.2) once and applying the initial condition gives the velocity as a function of time:

$$\frac{dx}{dt} = v(t) = v_0 + \frac{q_e V_{rf}}{m_e \omega d} \left[\cos \omega t - \cos \theta\right]. \tag{1.5}$$

Integrating a second time gives:

$$x(t) = \frac{v_0}{\omega}(\omega t - \theta) + \frac{q_e V_{rf}}{m_e \omega^2 d} \left[(\theta - \omega t)\cos\theta + \sin \omega t - \sin\theta\right]. \tag{1.6}$$

The resonance condition requires the electron to cross the gap after an odd number, N, of RF half-cycles: $x(\omega t = \theta + N\pi) = d$. If we substitute this into (1.6), we can now solve for the RF-voltage:

$$V_{rf} = \frac{m_e}{q_e} \frac{\omega d(N\pi v_0 - \omega d)}{N\pi \cos\theta + 2\sin\theta}. \tag{1.7}$$

This is the fixed phase relationship which states that, for a system with a particular voltage, frequency, and gap spacing, all electrons are emitted with phase θ relative to the electric field. Note that the initial velocity only appears in the numerator in (1.7). As a result, the minimum voltage for multipactor, V_{min}, occurs at the phase that maximizes the denominator.

The existence of the fixed phase relation implies that there is some mechanism that will allow randomly emitted electrons to reach *the* appropriate phase [1]. We can solve for this phase focusing mechanism by considering some error, ε, in the electron's emission phase. The electron's trajectory now has the boundary conditions $x(\omega t = \theta + \varepsilon) = 0$ and $x(\omega t = \theta + \varepsilon' + N\pi) = d$. By re-solving the equation of motion and dropping second-order terms, we can show that the phase error at impact, ε', is

$$\varepsilon' = \varepsilon \frac{N\pi}{2} \tan\theta. \tag{1.8}$$

If $\varepsilon'/\varepsilon < 1$, then the electrons will tend to approach the fixed phase, θ. Otherwise, the electron phases will tend to drift apart and the discharge cannot be sustained. As a result, a stable multipactor discharge will only occur when $\theta < \arctan(2/N\pi)$.

This stability condition will define the upper and lower voltage limits in our susceptibility diagram. Conveniently, the stable phase limit also minimizes (1.7) so the minimum RF voltage is

$$V_{min} = \frac{m_e}{q_e} \frac{\omega d(N\pi v_0 - \omega d)}{\sqrt{(N\pi)^2 + 4}}. \tag{1.9}$$

A multipactor discharge operating at the maximum voltage will occur at the most negative stable phase that allows an electron to overcome the retarding electric field and reach the opposite plate. If

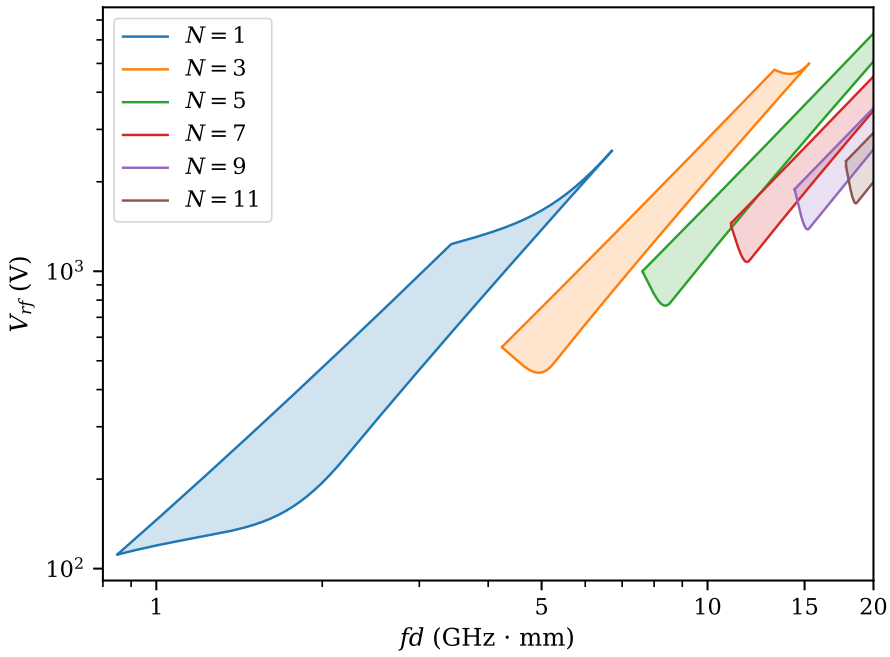

Figure 1.6: Example of a susceptibility diagram based on the classical theory. Monoenergetic electrons have an emission energy of 2 eV, the conductors' surfaces are assumed to have crossover points at $E_1 = 100$ eV and $E_2 = 1000$ eV.

the electrons are emitted when $v_0 = 0$, then $\theta = 0$ and

$$V_{max,0} = -\frac{m_e \omega^2 d^2}{q_e N \pi}. \tag{1.10}$$

For non-zero emission velocities, the equation for V_{max} becomes transcendental and must be solved numerically. The susceptible voltage range can be further restricted by requiring that the electrons' impact energies are between the two crossover points, E_1 and E_2 (see Fig. 1.4). By substituting (1.7) for V_{rf} in (1.5) and evaluating at $\omega t = N\pi$, we can solve for the impact velocity, v_i:

$$v_i = \frac{2\omega d \cos\theta}{N\pi \cos\theta + 2\sin\theta} + v_0. \tag{1.11}$$

Solving (1.11) for θ at the impact velocities corresponding to the two crossover points provides an additional constraint on the stable electron phases.

An example of the susceptibility diagram produced using the classical theory is shown in Fig. 1.6. To better illustrate the properties of a real device, we have adopted a fictional material with crossover points at $E_1 = 100$ eV and $E_2 = 1000$ eV. Electrons are assumed to be monoenergetic with an emission energy of 2 eV. Each shaded region represents the parameter space that supports a

particular order of multipactor. As the multipactor order increases, the susceptibility curves are more closely spaced and will eventually overlap; using a realistic, distributed emission energy model will further enhance this effect. When the curves overlap, multiple multipactor modes may be present within a single discharge; this will become the basis for the multipactor chaos model. Also note that the upper and lower boundaries of the overall susceptibility diagram exhibit significant jumps as the multipactor discharge transitions between modes.

The classical theory has been extended to describe other forms of multipactor discharges, such as single-surface dielectric breakdown [24] or in cross-field devices [45]. However, these are generally limited to planar geometries. Extending this theory to coaxial systems, for example, is difficult largely because the electric field is no longer uniform. As a result, resonance-based theories will require either numeric [50, 51] or highly approximate [10] solutions to the equation of motion; many studies on coaxial multipactor have focused on either particle-in-cell simulations [68–70] or experimental [15, 16, 22] investigations.

1.4 Multipactor Chaos Theory

So far, our discussions on multipactor have been in terms of a resonance between the oscillating electric field and the electrons' motion. This classical representation has been the basis of multipactor theory ever since it was first described by Philo Farnsworth [36]. However, recent analyses have found that the resonance condition is not as strict as we once thought [29, 30].

The resonance model begins to fail when we consider low-energy electrons impacting the surfaces. Although low-energy electrons cannot trigger true secondary electron emission, they can be reflected back into the bulk vacuum. In the classical theory of multipactor, when an electron is emitted against a retarding electric field, it must have sufficient initial energy so it can cross the gap and impact the opposite surface. If this is not the case, it is promptly returned to its original surface and is reabsorbed. Such an electron would represent an unsuitable phase for multipactor. We now know, however, that one of these low-energy impacts may scatter the electron back into the vacuum. If enough time has passed during this process, the electron may be re-emitted during a more favorable phase for multipactor.

This "ping-pong" mode—where an electron bounces off of its original surface before crossing the gap—will not release more than one electron for each primary impact, but the final impact, after finally crossing the gap, may instead release several electrons. Since electron backscattering is relatively efficient, the *average SEY over an RF-cycle* may be greater than unity. If this occurs, then multipactor will continue to grow.

Ping-pong modes and other forms of high periodicity multipactor are ignored in the classical theory, which assumes that every electron impact must release more than one secondary. Although

it is difficult to demonstrate experimentally, numerical investigations have shown that low-energy electrons—and therefore ping-pong modes—significantly affect electron dynamics and multipactor susceptibility [71]. Because of this, we will move away from the classical theory and its dependence on multipactor resonance.

Recently, Siddiqi and Kishek have proposed a new model for multipactor that is based on nonlinear dynamics and chaos theory [12]. This model has been extended from simply describing two-surface multipactor to include DC electric fields [12], dielectric surfaces [58], crossed magnetic fields [57], coaxial geometries [56], and multi-carrier signals [60, 61]. The flexibility of the chaos model for multipactor is highlighted by the fact that all of these extensions were published over a span of a single year.

We now present a brief overview of Siddiqi and Kishek's multipactor chaos theory. We begin by revisiting the two-surface planar system we previously analyzed using the classical theory [12]. Since this dissertation is focused on coaxial systems, we will continue with a brief discussion on extending the chaos theory to coaxial geometries and the challenges involved with doing so [56].

1.4.1 Planar Geometry

The chaos theory of multipactor makes no assumptions about the electron motion, aside from ignoring space-charge effects. Instead, it treats multipactor as a complex, dynamical system [12]. Since we make no presumptions regarding the electron dynamics, every possible combination of multipactor modes will be considered. This is achieved by using a map-based approach to iteratively track the development of the multipactor discharge.

In the chaos theory, we only need to consider two points in an electron's lifespan: its birth and its death. Every point in between is unimportant. Instead of tracking the trajectory of each individual electron, we will construct phase-maps that relates the phase of an electron's birth to the phase at which it impacts a surface.

We begin by considering the two infinite conductive parallel plates that we previously analyzed using the classical theory. We will identify these two surfaces as surface-0 at $x = 0$ and surface-1 at $x = d$. Because this system is perfectly symmetric, we can restrict our analysis to electrons that are emitted from surface-0; in an asymmetric system, such as in coax, we would need to construct two separate phase-maps to account for motion originating from each surface. We also adjust our temporal reference frame from our classical analysis such that the electrons are emitted at time $t = 0$ with a perpendicular velocity component v_0. Because of this shift in reference frame, the electric field is now

$$E(t) = E_0 \sin(\omega t + \theta) \tag{1.12}$$

with the field magnitude now expressed as $E_0 = V_{rf}/d$. From this, an electron's equation of motion

is

$$\frac{d^2x}{dt^2} = \frac{dv}{dt} = -\frac{q_e}{m_e} E_0 \sin(\omega t + \theta) \tag{1.13}$$

with initial conditions $x(0) = 0$ and $v(0) = v_0$. We will now adopt a normalization scheme so we can continue this analysis non-dimensionally. Our normalized variables are:

$$\tau = \omega t \tag{1.14a}$$

$$\bar{x} = \frac{x}{d} \tag{1.14b}$$

$$\bar{v} = \frac{v}{\omega d} \tag{1.14c}$$

$$\bar{E}_0 = -\frac{q_e E_0}{m_e \omega^2 d}. \tag{1.14d}$$

Recall that we have defined the electron charge as $q_e = -e$, so $\bar{E}_0$ is positive. The normalized equation of motion is now

$$\bar{x}'' = \bar{v}' = E_0 \sin(\tau + \theta) \tag{1.15}$$

with primes representing derivatives with respect to τ, and the initial conditions are now $\bar{x}(0) = 0$ and $\bar{v}(0) = \bar{v}_0 = v_0/\omega d$. Solving the equation of motion gives us the electron's velocity

$$\bar{v}(\tau, \theta) = -\bar{E}_0 \left[\cos(\tau + \theta) - \cos\theta\right] + \bar{v}_0 \tag{1.16}$$

and trajectory

$$\bar{x}(\tau, \theta) = -\bar{E}_0 \left[\sin(\tau + \theta) - \sin\theta - \cos\theta\right] + \tau \bar{v}_0 \tag{1.17}$$

as functions of τ. Note that we are also expressing these solutions in terms of the emission phase θ which is the primary independent variable in our maps.

In the classical theory, we would now implement a resonance condition; electrons emitted from surface-0 must return at $\tau = M\pi$ [24] or impact surface-1 at $\tau = N\pi$ [1], where M and N are even and odd integers, respectively. We no longer make this assumption. Instead, we will solve for the time of impact directly. To solve for the time of impact, we now set $\bar{x}(\tau_{00}) = 0$ and $\bar{x}(\tau_{01}) = 1$ for the single-surface and two-surface cases, respectively. Whichever event happens first determines whether or not an emission phase, θ, corresponds to a two-surface or single-surface mode. With the mode identified, we can now relate the impact phase to the emission phase. This gives us our phase map:

$$\theta_i(\theta) = \begin{cases} \mathrm{mod}(\tau_{00}, 2\pi) & \tau_{00}(\theta) < \tau_{01}(\theta) \\ \mathrm{mod}(\tau_{01} + \pi, 2\pi) & \tau_{01}(\theta) < \tau_{00}(\theta) \end{cases}. \tag{1.18}$$

Separate phase maps can be generated to represent a range of initial conditions, such as variations

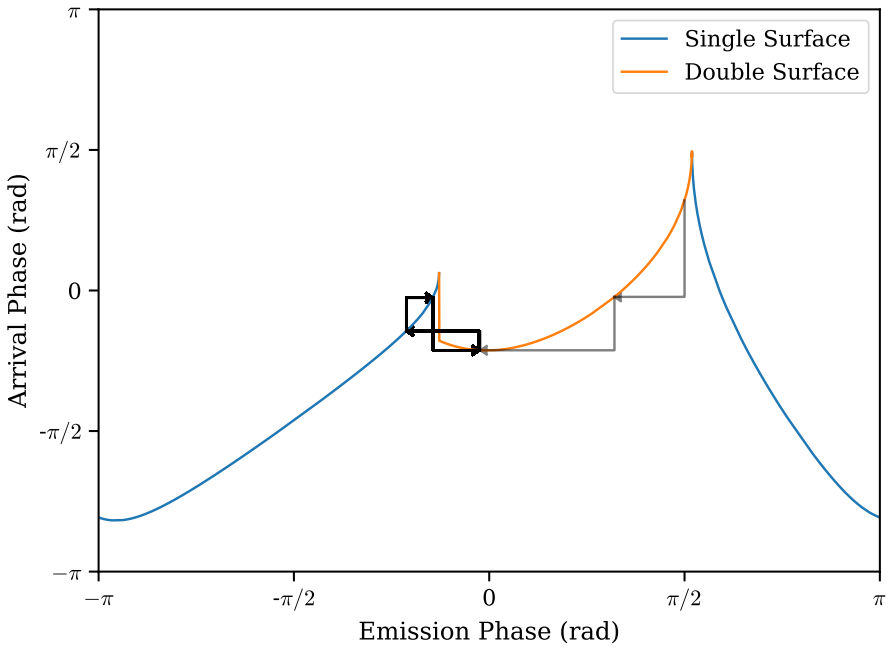

Figure 1.7: Example of a multipactor phase map and the iterative convergence procedure. These data correspond to the case where $\bar{E} = 0.5$ and $\bar{v}_0 = 0.03$. The phase progression of a seed electron born at $\pi/2$ is shown in black, with darker lines representing the final, converged ping-pong mode.

in the normalized electric field or emission velocity.

Describing a multipactor discharge now becomes a matter of iterating the phase map and tracking the electrons' motion. We begin with a collection of random seed phases; Siddiqi and Kishek determined that 64 seed phases are sufficient [12]. The evolution of each seed is tracked by using our maps to relate their emission phases to their impact phases. After several thousand iterations, the electrons' phases will converge onto the discharge's stable modes. Since we are primarily interested in the long-term behavior of a fully developed multipactor discharge, we will only analyze the last few iterations. Typically, we will use a total of 5,000 iterations, and retain only the final 1,000. The phases that remain at the end of this procedure, referred to as the attractor phases, represent the dominant modes of the multipactor discharge.

This iteration process is illustrated in Fig. 1.7, which shows the phase map for the case where $\bar{E} = 0.5$ and $\bar{v}_0 = 0.03$. Phases corresponding to single-surface multipactor events are shown in blue; two-surface events are in orange. An initial seed electron is born with phase $\theta = \pi/2$. This electron quickly converges to the dominant multipactor mode after only two impacts. In this case, there are three attractor phases at -0.67, -0.45, and -0.08 rad. During this ping-pong mode, the electron bounces off of one surface twice before finally crossing the gap.

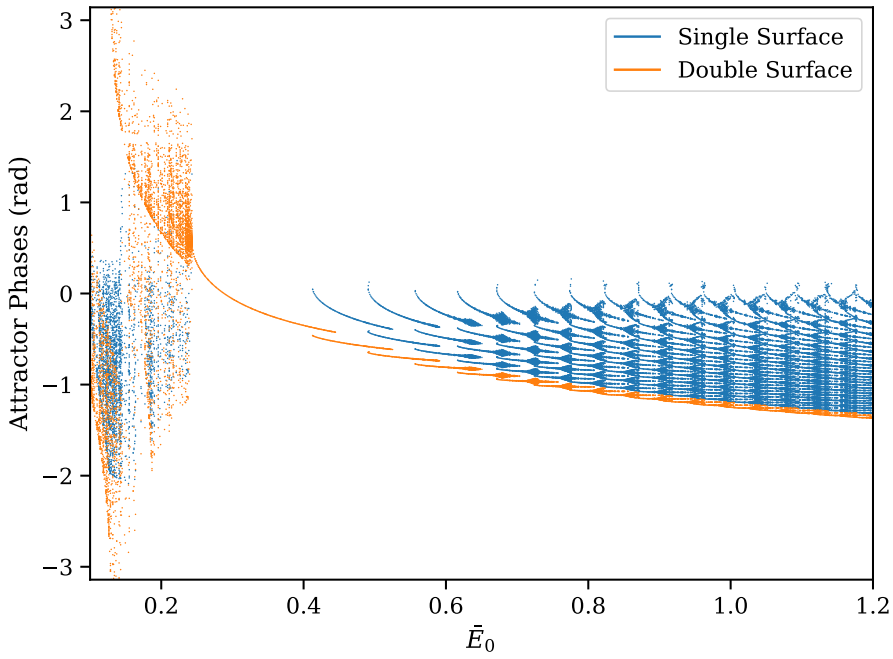

Figure 1.8: Example of a bifurcation diagram representing the attractor phases of a multipactor discharge as a function of the normalized electric field. These data were independently reproduced based on the formulation by Siddiqi and Kishek [12, see Fig. 2a].

To better illustrate the global multipactor behavior, we can construct a bifurcation diagram. Bifurcation diagrams plot the attractor phases as a function of some independent variable. An example of this is shown in Fig. 1.8, which is plotted as a function of the normalized electric field. Attractor phases for the single and double-surface multipactor modes are indicated by blue and orange lines, respectively. These data were generated using phase-maps corresponding to a normalized emission velocity of $\bar{v}_0 = 0.03$ and 1,000 values of $\bar{E}_0$, and each phase-map was generated using 10^4 discrete phases. The bifurcation diagram presented in Fig. 1.8 replicates data from Siddiqi and Kishek [12, see Fig. 2a] and was independently reproduced by the present author. Differences between the two datasets can likely be attributed to the reduced number of phases (10^4 versus 10^6) used in generating our phase-maps.

In Fig. 1.8, the attractor phases fall into three distinct regimes. The first occurs when the normalized electric field is low. This regime is chaotic—the attractor phases have no discernible pattern, and small changes in $\bar{E}_0$ will radically alter the dominant modes. There is no resonance between the electrons' motion and the electric field, directly contradicting the classical multipactor theory. As the normalized electric field increases, the attractor phases abruptly converge to a single value. This corresponds to the boundary of classical, two-surface, first-order multipactor. Further

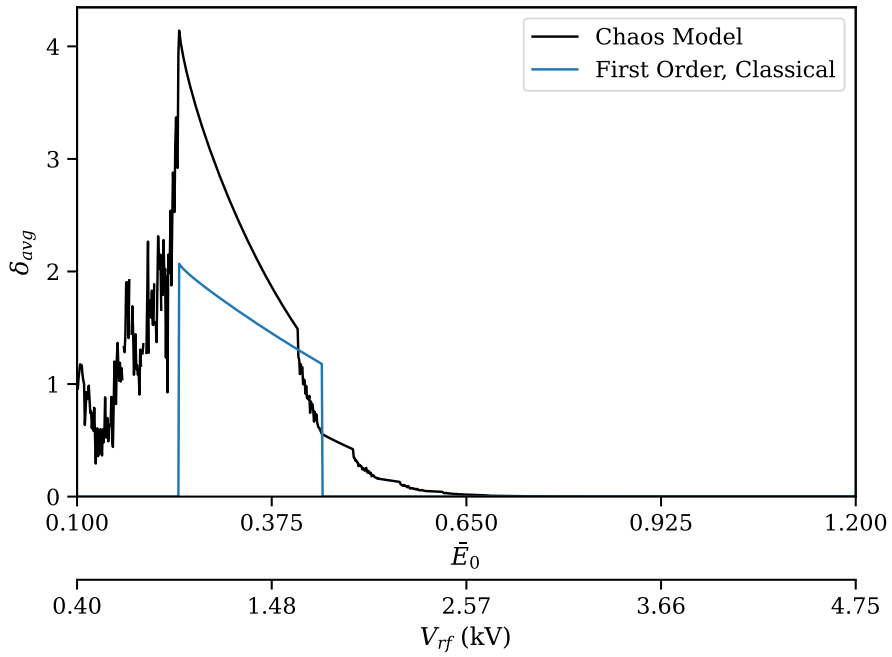

Figure 1.9: Average SEY of a planar multipactor discharge based on chaos theory. These data were independently reproduced based on the formulation by Siddiqi and Kishek [12, see Fig. 5].

increases in the normalized electric field will reveal single-surface multipactor modes. This final regime represents a combination of classical two-surface and ping-pong modes.

Obtaining susceptibility data from the chaos theory is simply a matter of finding the average SEY over an RF-cycle. The multipactor growth rate can be obtained by averaging over all of the attractor phases:

$$\lambda(\bar{E}_0, \bar{v_0}) = \omega \frac{\ln\left(\prod_i \delta_i \prod_j \delta_j\right)}{\sum_i \tau_i + \sum_j \tau_j} \tag{1.19}$$

where δ_i (δ_j) and τ_i (τ_j) are the SEY and lifetime of the ith (jth) single-surface (double-surface) attractor phase; δ_i and δ_j are obtained by calculating the impact velocity from (1.16) and applying an SEY model. The SEY, averaged over an RF-cycle, is then:

$$\delta_{avg}(\bar{E}_0, \bar{v_0}) = \exp(\lambda T_{rf}) = \left(\prod_i \delta_i \prod_j \delta_j\right)^{\left(\frac{1}{2\pi\left(\sum_i \tau_i + \sum_j \tau_j\right)}\right)} \tag{1.20}$$

where $T_{rf} = 2\pi/\omega$ is the RF-period. If the effective SEY is greater than unity, then multipactor will occur.

The SEY curve for the bifurcation diagram from our prior example is shown in Fig. 1.9. These data, which were independently reproduced from Siddiqi and Kishek [12, see Fig. 5], are for a transmission line with $d = 7$ mm, $f = 500$ MHz, and $\bar{v}_0 = 0.03$. Secondary emission data was generated using the modified Vaughan model [27, 28] with parameters matching those used by Siddiqi and Kishek [12]. For comparison, the SEY of a classical, first-order multipactor discharge is also shown. Both models show that first-order, two surface multipactor is the primary contributor to the discharge, as indicated by the two curves' sharp, trapezoidal peaks. However, the chaos model clearly shows that non-resonant modes, which are completely ignored by the classical theory, are extremely important; these lower-power modes increase the susceptible voltage range by a factor of two.

Although our analysis thus far has only considered monoenergetic secondary electron emission, the chaos model is easily extended to consider realistic emission energy distributions by borrowing a method from single-fluid plasma modeling [12, 72]. The polyenergetic effective secondary emission yield is obtained by integrating over an emission velocity distribution, $f(\bar{v})$:

$$\delta_{eff} = \int \delta_{avg}(\bar{E}_0, \bar{v}_0) f(\bar{v}_0) d\bar{v}_0. \tag{1.21}$$

When using an emission energy distribution, separate maps must be generated for each discrete value of $\bar{v}_0$.

1.4.2 Coaxial Geometry

Extending the chaos theory to a coaxial geometry uses the same basic procedure [56]. We will consider a coaxial transmission line, which is illustrated in Fig. 1.10, with inner and outer radii a and b, respectively. We assume that the electric field follows a TEM mode, so the force law is

$$\ddot{r} - r(\dot{\phi})^2 = -\frac{1}{r}\frac{q_e V_{rf}}{m_e \ln(b/a)} \sin(\omega t + \theta), \tag{1.22}$$

and

$$r\ddot{\phi} + 2\dot{r}\dot{\phi} = 0. \tag{1.23}$$

Note that we are including the equation for the electrons' azimuthal motion; secondary electrons will carry angular momentum because they are emitted from the surfaces at an angle. The electrons' angular momentum will be conserved because there are no azimuthal forces; this allows us to reduce the equations of motion to a single, second-order differential equation:

$$\ddot{r} - \frac{1}{r^3}\left(\dot{\phi}_0 r_0^2\right)^2 = -\frac{1}{r}\frac{q_e V_{rf}}{m_e \ln(b/a)} \sin(\omega t + \theta) \tag{1.24}$$

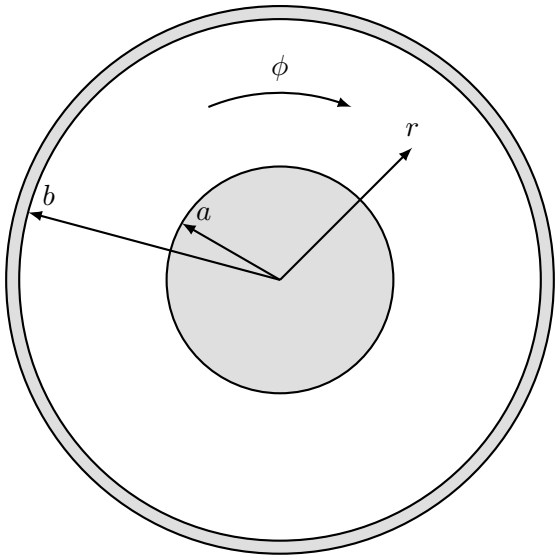

Figure 1.10: Illustration a coaxial transmission line modeled using the chaos theory of multipactor.

where r_0 and $\dot{\phi}_0$ are the electrons' initial radial position and angular velocity, respectively. Equation (1.24) does not have an analytic solution, so we must rely on numerical methods to produce the phase maps. However, once the maps have been generated, the attractor phases and the average secondary electron yield can be calculated using the same procedure as in the planar case. Since we are now also considering a distributed emission angle, $f(\phi_0)$, the effective SEY is the double integral over both angle and velocity:

$$\delta_{eff} = \int \int \delta_{avg}(\phi_0, \bar{v}_0) f(\phi) f(\bar{v}_0) d\bar{v}_0 d\phi_0. \tag{1.25}$$

Solving the equation of motion is the primary challenge when analyzing coaxial transmission lines. Numerical solutions are much more computationally expensive than the planar theory's analytic solution[11]. In the present author's experience, generating a single phase-map with 10^4 phases takes approximately one minute. Although this does not, at first, seem terribly significant, simulating realistic emission angle and velocity distributions increases the runtime dramatically. Calculating δ_{eff} using 25 velocities and 10 angles will require 250 phase-maps; this only provides a prediction for a single RF-voltage at a single impedance. To generate a susceptibility diagram for our experiment, we need to sweep both of these parameters.[12] Simulating 25 impedances and voltages each will now require 156,250 phase-maps; with a runtime of one minute each, this results

[11]Though analytic approximations to the coaxial equation of motion do exist, they either ignore angular momentum effects [10] or rely on difficult-to-evaluate elliptical integrals [54].

[12]As we will discuss in Chapter 3, adjusting fd in our experiment will require altering the transmission line's characteristic impedance.

in a total of runtime of 108.5 days. Then we will still need to iterate each phase map and find the attractor phases.

The chaos theory of multipactor is an extremely powerful tool. It provides an exact representation of multipactor's complex, dynamic nature, but it is extremely computationally expensive. Though Siddiqi and Kishek do provide some comparisons with experimental results [56]—with excellent agreement—using this theory for designing equipment will often be impractical. However, despite the chaos theory's high up-front computational cost, once the phase-maps and bifurcation diagrams have been produced, applying the SEY model is relatively inexpensive. This gives the theory some flexibility when designing a device: one could, after first finding the attractor phases, quickly simulate a wide range of material conditions.

1.5 Preventing Multipactor

As we have discussed, multipactor is extremely dangerous in vacuum electronic systems and must be avoided to ensure reliable, long-term operations. This is particularly true in satellite communication systems where replacing damaged components is impossible. Several methods have been explored to prevent multipactor. Simple methods rely on directly reducing the secondary emission yield, such as by adding surface coatings and using alternative materials [73–76] or undergoing multipactor self-conditioning [74, 77]. Other suppression techniques will rely on altering the electron dynamics by introducing external magnetic fields [17, 78–81] or DC electric fields [74]. External magnetic fields, in particular, can be very effective for preventing multipactor; in a coaxial system, sufficiently strong axial fields could block all electron motion between the two conductors. Altering the RF drive signals can also disrupt the multipactor resonance. These methods can range from using simple amplitude [82] or digital [19] modulation to abandoning sinusoidal wave-forms altogether [66]. One additional strategy for preventing multipactor is by trapping the emitted secondary electrons within the surface by introducing surface roughness, either at the microscopic [83] or macroscopic scale [84, 85]. This can be taken one step further by perforating the transmission line and allowing electrons to escape the multipactor discharge [86–89].

All of these methods rely on reducing the secondary electron yield, either directly by altering material properties (coatings, alternate materials) or by manipulating the electron dynamics to reduce impact energies (applying external electromagnetic fields). However, the last two methods (surface texture and porosity) instead take advantage of how the physical structure of the device can affect electron motion. This is illustrated in Fig. 1.11 which shows electron emission from flat, textured, and porous surfaces.

When an electron strikes a surface, a secondary electron will be emitted at some angle. On a flat surface, as in Fig. 1.11a, secondary electrons return directly to the bulk vacuum. Introducing

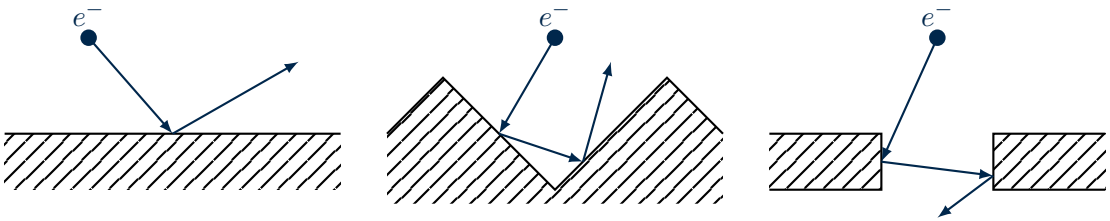

(a) Flat Surface (b) Textured Surface (c) Porous Surface

Figure 1.11: Illustration of how secondary electron emission is impeded by altering the surface morphology. Examples are shown for emission from flat, textured, and porous surfaces in **(a)**, **(b)**, and **(c)**, respectively.

surface structures may interrupt this process. Figure. 1.11b shows an electron impacting a textured surface. Instead of returning directly to the bulk vacuum, secondary electrons may instead collide with a protrusion from the surface. Secondary electrons are generally emitted with low energies; typically on the order of a few electron volts [1]. As a result, subsequent impacts against the surface structures may result in the re-absorption of secondary electrons into the material. This effect is enhanced further when we introduce surface porosity, as in Fig. 1.11c; secondary electrons will not only undergo multiple impacts, but they may pass through the surface and leave the system entirely.

This work will experimentally test the efficacy of using textured surfaces for preventing multipactor. These experiments, which will be discussed in Chapter 5, will use a partially 3D-printed transmission line. Many additive manufacturing processes share a unique tendency to produce inherently textured components, and such parts can be used as drop-in replacements for traditionally manufactured components. We will demonstrate proof-of-concept for using these 3D-printed structures to prevent multipactor.

CHAPTER 2

Particle-in-Cell Simulations

As we discussed in Chapter 1, multipactor discharges are extremely difficult to describe theoretically, particularly in coaxial geometries. Particle-in-cell (PIC) codes help bypass this difficulty by directly simulating the electron trajectories and electromagnetic responses during a multipactor discharge. In this chapter, we discuss a method for using CST Particle Studio to simulate multipactor discharges and predict the breakdown characteristics of our experimental hardware.

2.1 Method for Quantifying Multipactor Susceptibility

Our simulations will focus on finding the lower bound of the susceptibility diagram. This breakdown threshold is the minimum RF-power necessary to sustain a multipactor discharge. We can quantify this threshold by considering the evolution of the electron population, n_e, as a function of time. Since multipactor is driven by secondary electron emission, the electron population at time $t + \tau$ is

$$n_e(t + \tau) = \delta(t) n_e(t) \tag{2.1}$$

where τ is the average electron lifespan and $\delta(t)$ is the effective secondary electron yield as a function of time. Thus, from (2.1), a stable, growing multipactor discharge will occur when the secondary electron yield is greater than unity. By rearranging (2.1), we can solve for the effective secondary emission yield

$$\delta(t) = \frac{n_e(t + \tau)}{n_e(t)}. \tag{2.2}$$

Since the multipactor electrons are generally resonant (albeit chaotically) with the RF drive signal, $\delta(t)$ will oscillate with respect to time. When determining the boundaries of the operating regime for multipactor discharges, it becomes convenient to define an average effective secondary emission

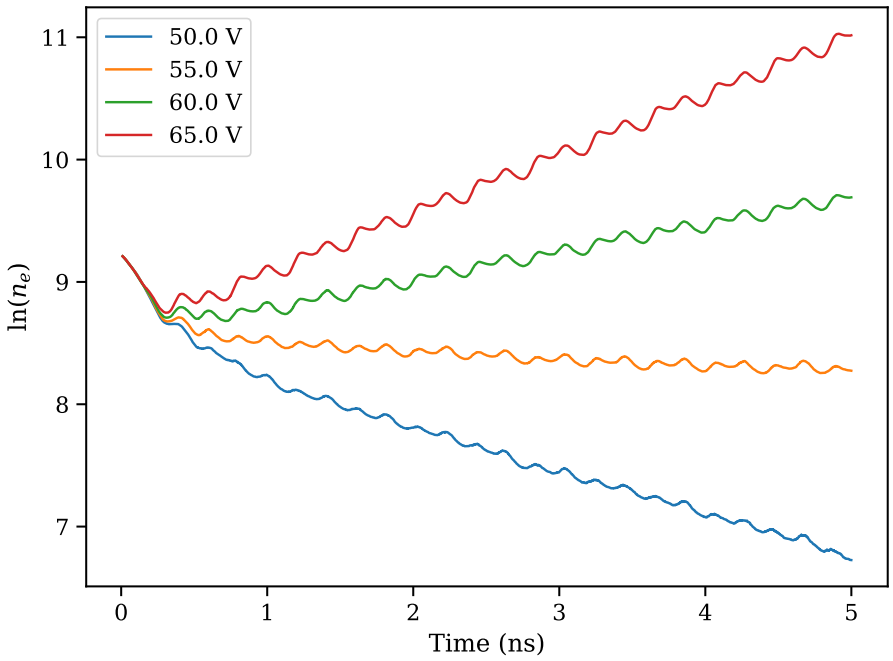

Figure 2.1: Evolution of the electron population in a multipacting 50-Ω coaxial transmission line with $fd = 1.0\ \mathrm{GHz} \cdot \mathrm{mm}$ operating at 2.45 GHz with several RF-voltages.

yield, δ_{ave}. The average effective SEY is defined as the time average of $\delta(t)$ over an RF-period:

$$\delta_{ave} = \frac{1}{T_{rf}} \int_0^{T_{rf}} \delta(t) dt \tag{2.3}$$

where $T_{rf} = 1/f$ is the RF-period. During a stable, growing multipactor discharge, the average effective secondary emission yield must be greater than unity; thus, we can define the multipactor breakdown threshold voltage as the minimum RF-voltage such that $\delta_{ave} = 1.0$.

In our CST simulations, we track the growth of the electron population as a function of time; an example is shown in Fig. 2.1 for a 50-Ω transmission line with $fd = 1.0\ \mathrm{GHz} \cdot \mathrm{mm}$ operating at RF-voltage amplitudes ranging from 50 to 65 V. In the two highest-power cases, we see that their electron populations are steadily increasing in time, indicating that they are stable multipactor discharges. Conversely, the electron population steadily dies off when the voltage is only 50 V. When the RF-voltage is 55 V, the electron population declines much more slowly, suggesting that the discharge is only slightly below the multipactor breakdown threshold.

Figure, 2.2 shows the effective SEY as a function of time for this example case calculated using (2.2). For simplicity, we assume the system is undergoing first-order, two-surface[1] multipactor so $\tau \approx T_{rf}/2$. The values for the average, effective SEY, δ_{ave}, are shown as horizontal dotted lines

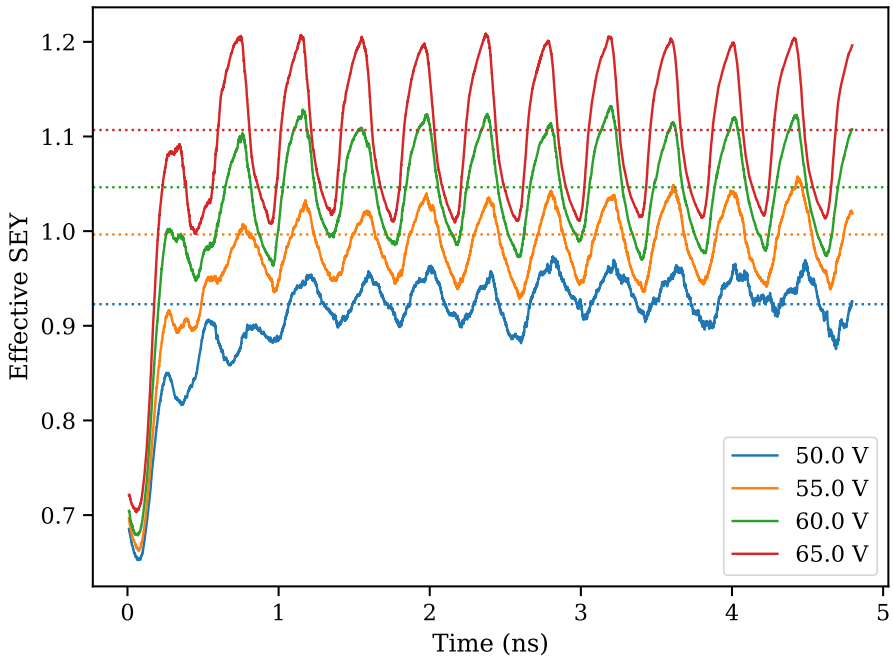

Figure 2.2: Evolution of $\delta(t)$ in a multipacting 50-Ω coaxial transmission line with $fd = 1.0\ \mathrm{GHz} \cdot \mathrm{mm}$ operating at 2.45 GHz with several RF-voltages. The average effective SEY, δ_{ave} is shown as horizontal dotted lines.

and were generated by averaging over the last RF-cycle of each simulation. After the discharges develop, they reach a steady oscillation around δ_{ave}. From these data, we can clearly see that the slow decline in electron population for the 55-V discharge corresponds to an average effective secondary emission yield slightly below unity. This further supports our observation that the breakdown threshold must be slightly higher than 55 V. The average effective secondary emission yield becomes a simple tool for measuring the breakdown threshold. Since we are only concerned with finding the conditions necessary to support stable, growing multipactor discharges, δ_{ave} filters out oscillations on the time-scale of a single RF-cycle and provides long-term insight on whether or not a discharge will tend to grow or decay.

To generate our susceptibility diagrams, we perform CST PIC simulations over a range of RF-voltages (typically in steps of 5 or 10 V) and generate a relationship between δ_{ave} and RF input power. We then obtain the predicted breakdown threshold by interpolating these data to find the

[1]When determining the multipactor susceptibility, the choice of τ is arbitrary, so long as the data are averaged over several RF-cycles. Although the magnitude of the multipactor growth rate may be affected, the overall trend of growth or decay will be preserved. Determining the true value of τ requires precise knowledge of the dominant multipactor modes.

RF-voltage such that $\delta_{ave} = 1$. To obtain the threshold in units of power, we use the relation

$$P_{rf} = \frac{V_{rf}^2}{2Z_0} \tag{2.4}$$

where V_{rf} is the peak RF-voltage and Z_0 is the transmission line's characteristic impedance.

When determining the multipactor susceptibility, our simulations ignore space-charge effects. During the onset of multipactor, the electron population is very small. Thus, space-charge should have a negligible effect on susceptibility. This is contrary to a recent paper by Iqbal *et al.* [65] which had suggested that, under certain circumstances, space-charge effects may alter the breakdown threshold. However, this paper initiated their simulations with a very high initial space-charge; this is not representative of a multipactor discharge developing from a small seed electron population.

2.2 Validating CST Particle Studio

Before simulating experimental structures, it is necessary to investigate under what conditions CST Particle Studio reproduces existing experimental multipactor results. This test is necessary for two reasons: first, we must ensure that multipactor discharges simulated by CST exhibit realistic, physical behavior; secondly, we must choose a secondary emission model that accurately represents the surface conditions of the multipacting transmission line. While secondary emission data are extremely important for predicting multipactor, choosing the correct model can be difficult when surface conditions are unknown. We tested several emission models to ensure our simulations can reproduce published experimental data and provide reliable predictions of for our experiment.

For these verification tests, we compared our CST predictions of the multipactor breakdown threshold to results from Woo's 1968 experiment. We simulated a simple, 50-Ω characteristic impedance coaxial transmission line, which is illustrated in Fig. 2.3. Two wave ports at either end of the coaxial structure allow a constant-amplitude, TEM traveling wave to pass through the system and stimulate the multipactor discharge. Particles that reach these wave ports are removed from the simulation; a random-walk analysis showed that, on the length and time-scales of these simulations, this particle loss is negligible [68]. These simulations were performed at a frequency of $f = 2.45$ GHz, and fd ranges from 1 to 3 GHz $\cdot$ mm. Since the frequency was held constant, fd was adjusted by altering the gap between the inner and outer conductors while maintaining an aspect ratio of $b/a = 2.3$. A cloud of electrons was introduced at the beginning of the simulation to seed the multipactor discharge. These seed electrons were randomly distributed in position, direction, and energy and fill the full volume of the transmission line vacuum. During these simulations, we ignored space-charge effects, which should be negligible during multipactor onset.

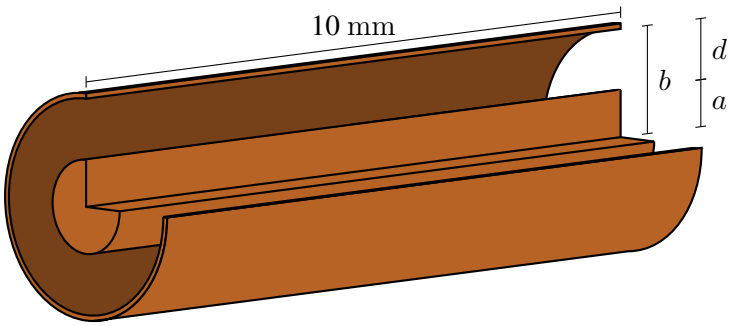

Figure 2.3: Simple coaxial model used for verifying CST PIC simulations. The transmission line characteristic impedance is held constant at 50 Ω with $b/a = 2.3$ and $d = b - a$. The length of the transmission line is also held constant at 10 mm.

2.2.1 Multipactor Susceptibility from Different SEY Models

When simulating multipactor discharges, the SEY model chosen to represent the surfaces is of crucial importance. In particular, the breakdown threshold can be extremely sensitive to the SEY model; in [90], Fil *et al.* tested six SEY models, all fit to the same experimentally measured SEY data, and found that the threshold electric field could vary by as much as 364%. This implies that it may be impossible to run an accurate multipactor simulation without first calibrating the SEY model against existing experimental data. Ultimately, this means that we must test several SEY models to ensure that our simulations are accurate.

CST Particle Studio uses three main models for representing secondary electron emission [91]. The first model is simply the direct import of tabulated SEY data. Imported data can only represent electrons impacting normal to a surface; angular effects are represented using a correction factor that is based on the formulation used in the Vaughan model [27, 91]. The last two models are both semi-empirical: the Vaughan [27] and Furman [31] models. The Vaughan model is relatively simple; it only requires the maximum secondary emission yield (and the energy at which it occurs). The form implemented in CST also allows for a smoothness parameter (assumed to be unity for smooth surfaces; higher values correspond to rougher materials) and a threshold energy below which the SEY is zero. The Furman model is the second semi-empirical model offered by CST. Unlike the Vaughan model which only considers the total number of secondary electrons emitted, the Furman model includes the emission of "backscattered" and "rediffused" electrons (those that had been reflected by the surface) in addition to the "true" secondary electrons (which are fully absorbed and then re-emitted). While the Furman model is the most physically descriptive, it relies on forty-four fitting parameters, of which there are few sets available. Note that modified Vaughan model does include reflected secondary electrons [26, 28], but it has not been implemented in CST Particle Studio [91]. Additionally, unlike the Vaughan model, the Furman model does provide a model for

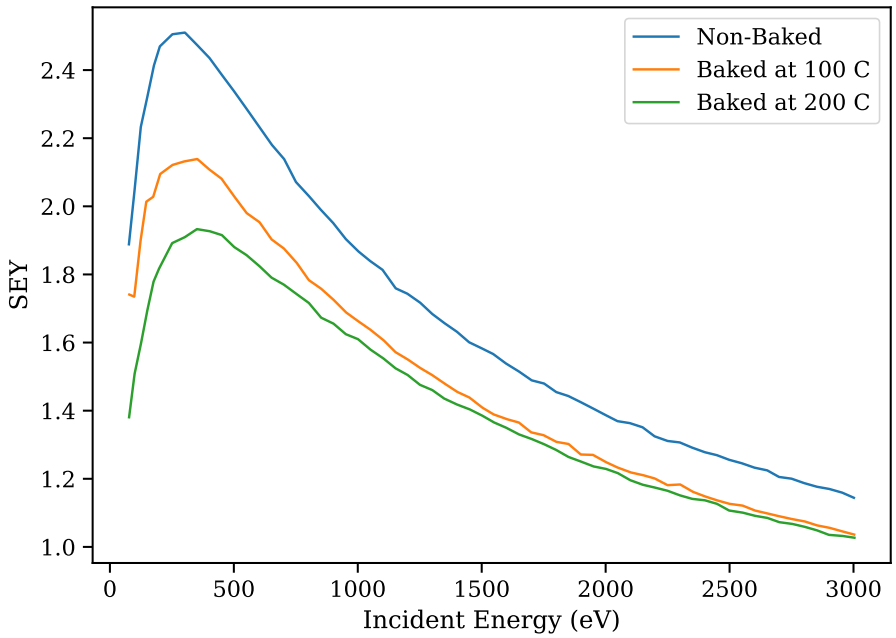

Figure 2.4: Tabulated copper SEY data from Bojko *et al.* [92] used for CST PIC simulations.

the electrons' emission energy. CST uses a simplified form of this model when using tabulated data or the Vaughan model and is weighted by a user-input temperature [91].

In these tests, we compared CST PIC simulations performed using tabulated data from Bojko *et al.* [92] to those using the Furman model in an attempt reproduce Woo's experiment [15]. For the Furman model, we will use the fitting parameters for copper from his original paper [31]. The tabulated SEY data, which are plotted in Fig. 2.4, represent copper that is either non-baked, or has been baked for 24 h at 100 $^{\circ}\mathrm{C}$ or 200 $^{\circ}\mathrm{C}$ [92].

The simulated multipactor susceptibility diagram based on each SEY model is shown in Fig. 2.5. These data are compared to Woo's experiment [15], which is shown in black. It is unsurprising to note that the data for non-baked copper provided the best agreement with the experiment. At higher values of fd, the simulated breakdown voltage agreed with Woo's data to within 5% (or 10% in power units), as indicated by the shaded region. In Woo's experiment, he used copper electrodes that had been abrasively cleaned, but had otherwise been left untreated [15]. These conditions most closely match those used for the non-baked tabulated data, where the copper had only been chemically cleaned [92]. Since both these methods are performed in air, the oxide layers should remain relatively undisturbed and thus have relatively similar secondary emission yields. This agrees with Graves's experiment where the presence of these oxide layers was essential for reproducing Woo's data [16]. This is further demonstrated when using the SEY data for

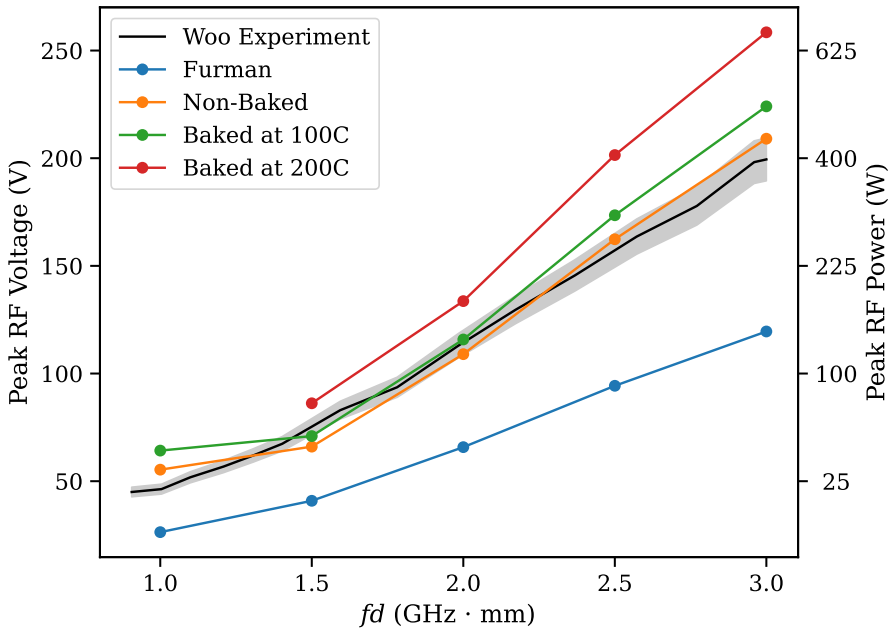

Figure 2.5: Multipactor susceptibility diagram from PIC simulations of a 50-Ω coaxial transmission line using several SEY models. Axes are scaled for both voltage (left) and power (right) units. Shaded regions represent an agreement, in voltage units, within 5% (or 10% in power units) with data from Woo's 1968 experiment [15].

baked surfaces; increasing the bake-out temperature tended to increase the multipactor breakdown threshold, as was the case in Graves's experiment.

While the simulations using the tabulated SEY data generally agreed with Woo and Graves's experiments, those generated using the Furman model did not fare as well. Over the full range of fd, the Furman model significantly under-predicted the multipactor breakdown threshold. The exact cause of this mismatch is difficult to identify conclusively, but is most likely due to differences between the materials used in Bojko *et al.* [92] and the experimental data used to define the Furman model [31]

2.2.2 General Multipactor Behavior

While we are ultimately using CST Particle Studio for generating predictions of multipactor susceptibility, it is also important to ensure that the simulated multipactor discharges display realistic dynamic behavior. This is visualized in Fig. 2.6 which shows a multipactor discharge developing from a single seed electron. This simulation was performed using the SEY data for non-baked copper in a 50 Ω transmission line with $fd = 2.00\ \mathrm{GHz} \cdot \mathrm{mm}$. We see that the discharge has grown to over 3000 electrons and is azimuthally uniform after only a few nanoseconds, which

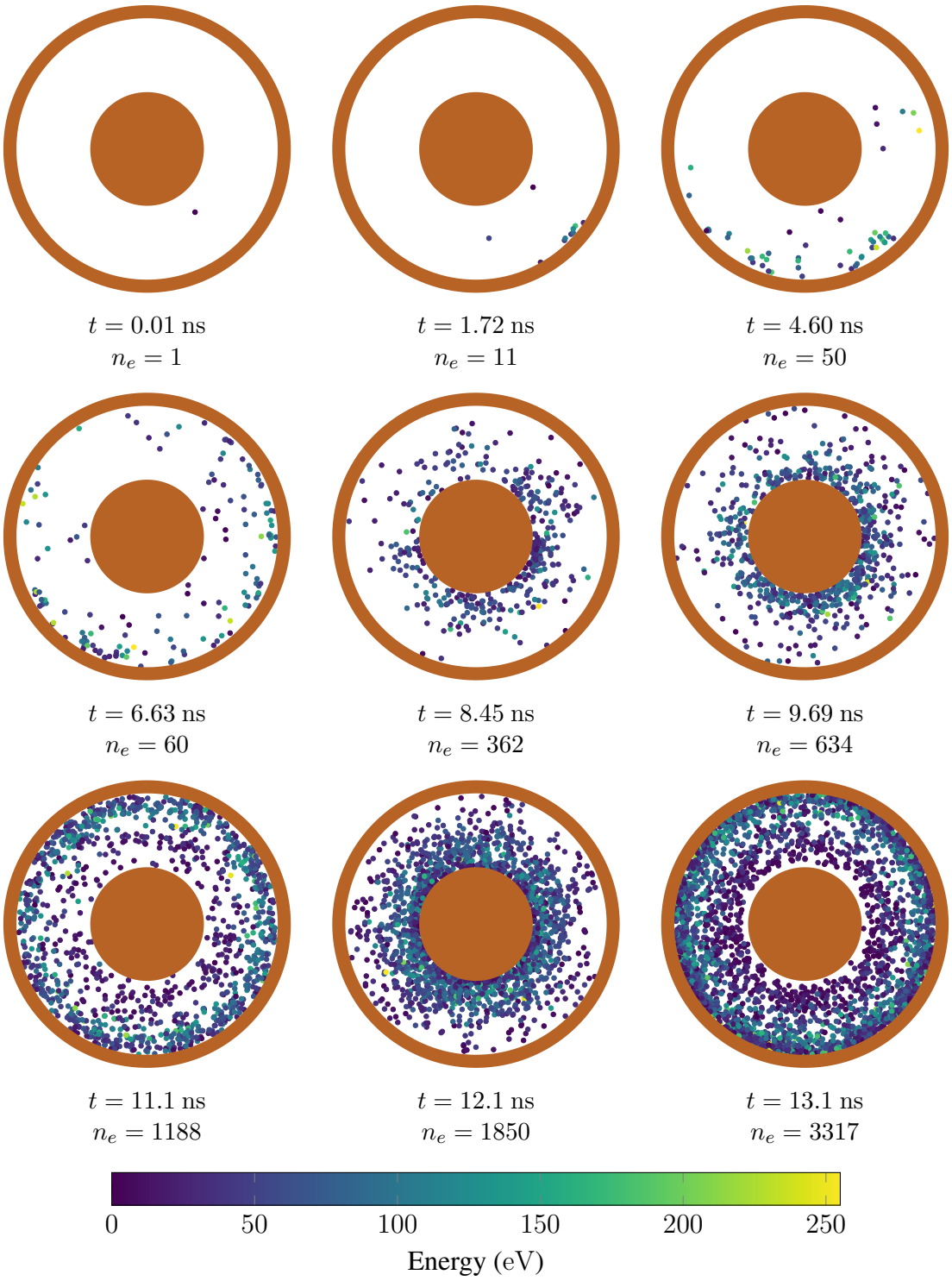

Figure 2.6: Visualization of the evolution of a multipactor discharge from a single seed electron. These data were generated in CST Particle Studio with $V_{rf} = 120$ V, $fd = 2$ GHz $\cdot$ mm, $f = 2.45$ GHz, and $b/a = 2.3$ (50-Ω characteristic impedance).

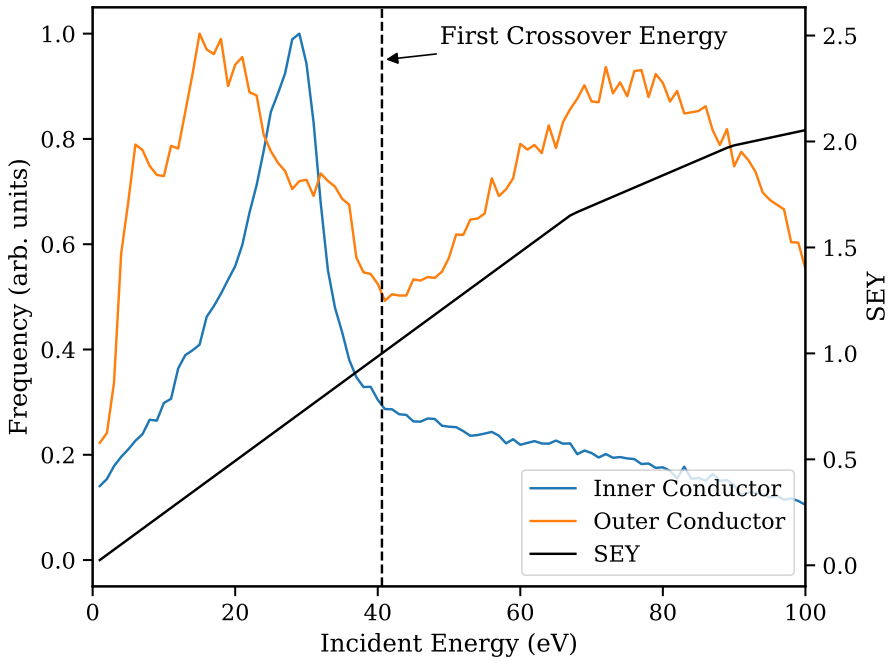

Figure 2.7: Energy spectrum of electrons impacting the inner and outer conductors of the coaxial transmission line during a multipactor discharge operating at the breakdown threshold.

is consistent with published experimental measurements [16].

Another interesting behavior concerns the energy spectrum of electrons impacting the two coaxial conductors. Such a spectrum is shown in Fig. 2.7 for a multipactor discharge operating with an RF-voltage slightly above the breakdown threshold. These spectra are superimposed over the non-baked SEY data used in this simulation. A vertical dotted line indicates the first crossover energy—the energy at which impacting electrons emit exactly one secondary. Electrons tend to impact the inner conductor at relatively low energies, below the first crossover point. This suggests that multipactor discharges are driven primarily by the higher-energy impacts that occur on the outer conductor. This implies that multipactor suppression is more heavily dependent on the surface characteristics of the outer conductor. We will take advantage of this property in Chapter 5 where we will explore multipactor-suppressive technologies. It is also intriguing to note that the spectrum of electrons impacting the outer conductor is double peaked. The second, lower energy peak is most likely due to single-surface and higher order multipactor modes, which generally have relatively low impact energies [12, 56]. These results also agree with other studies which used the idealized model of infinitesimally thin, axisymmetric, sheets of multipacting electrons with monoenergetic emission velocities [5, 10, 53].

When we take space-charge into account, a multipactor discharge should eventually reach

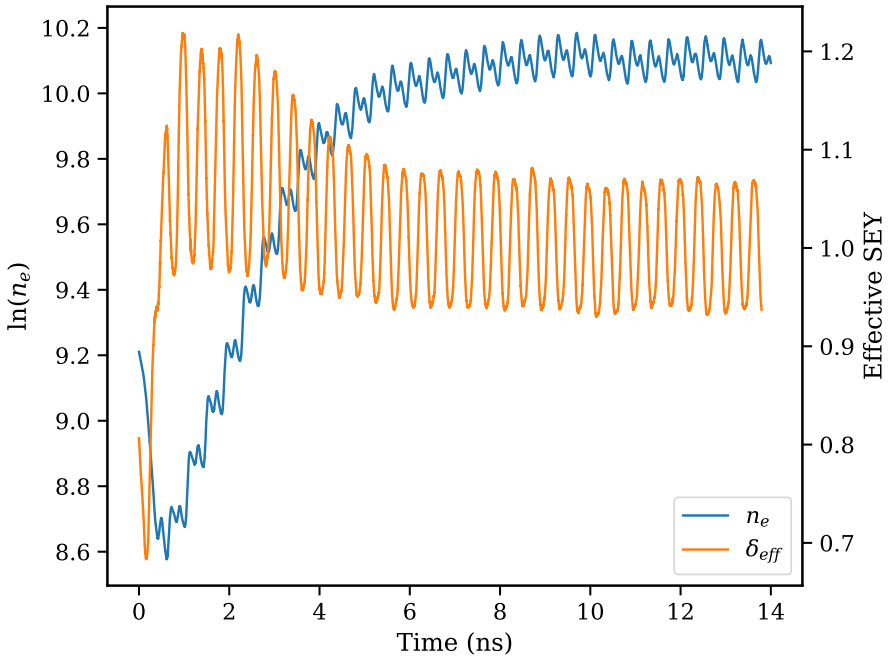

Figure 2.8: Evolution of the electron population and effective SEY during a saturated multipactor discharge.

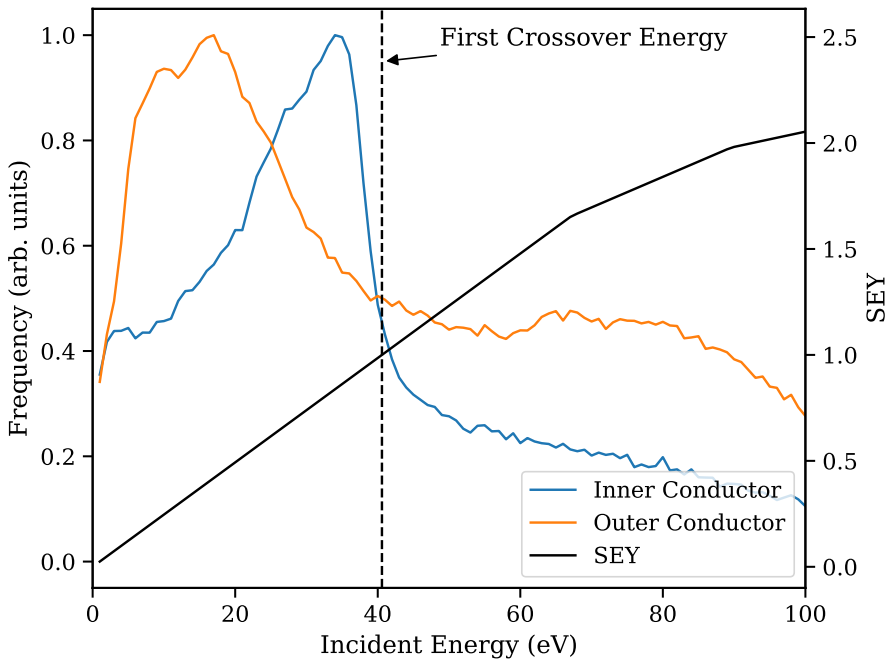

Figure 2.9: Energy spectrum of electrons impacting the inner and outer conductors of the coaxial transmission line during a saturated multipactor discharge.

saturation. During saturation, the background, charge-induced electric field disrupts the multipactor resonance and prevents further growth. We demonstrate this by performing a simulation that now considers space charge effects. This simulation was performed using the non-baked SEY data and a transmission line with $fd = 2\ \mathrm{GHz} \cdot \mathrm{mm}$ operating with $V_{rf} = 120\ \mathrm{V}$. Since multipactor discharges reach saturation at extremely high electron densities, we use macro-particles weighted with the charge and mass of 10,000 electrons.

The evolution of the electron population and effective secondary emission yield during this saturated discharge is shown in Fig. 2.8. After an initial phase of rapid growth, the electron population slows down after approximately 4 ns before reaching steady state after 10 ns. We also see that the effective SEY oscillates around unity at this point. This behavior is a clear indication that the discharge has reached saturation.

We also expect the impact energy spectrum to be altered somewhat during a saturated discharge. This is shown in Fig. 2.9 where we see that fewer high-energy electrons (~80 eV) now impact the outer conductor, significantly inhibiting their contribution to the discharge's growth.

2.3 Simulations of the Experimental Configuration

To ensure that the test cell will undergo multipactor at the desired experimental parameters, PIC simulations were performed to provide predictions of the multipactor breakdown threshold. A schematic representation of the coaxial transmission line used in the test cell is shown in Fig. 2.10.

The test cell uses a stepped coaxial transmission line. At its center lies the multipacting region where the gap between the two conductors is smallest. The relatively small gap ensures that the local multipactor breakdown threshold is reduced; this concentrates the discharge into this region.

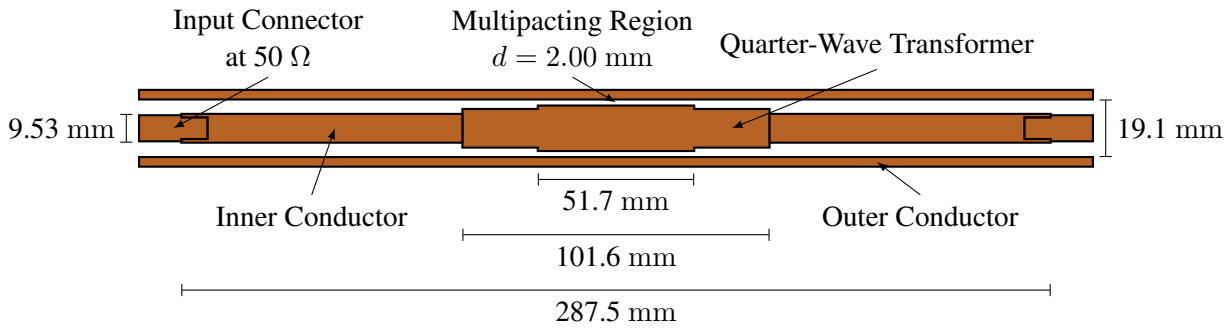

Figure 2.10: Schematic of the stepped coaxial structure used in this experiment. Dimensions are shown for the case where $d = 2.00\ \mathrm{mm}$. Simulations for other values of d were performed using dimensions matching the as-built hardware detailed in Appendix C.

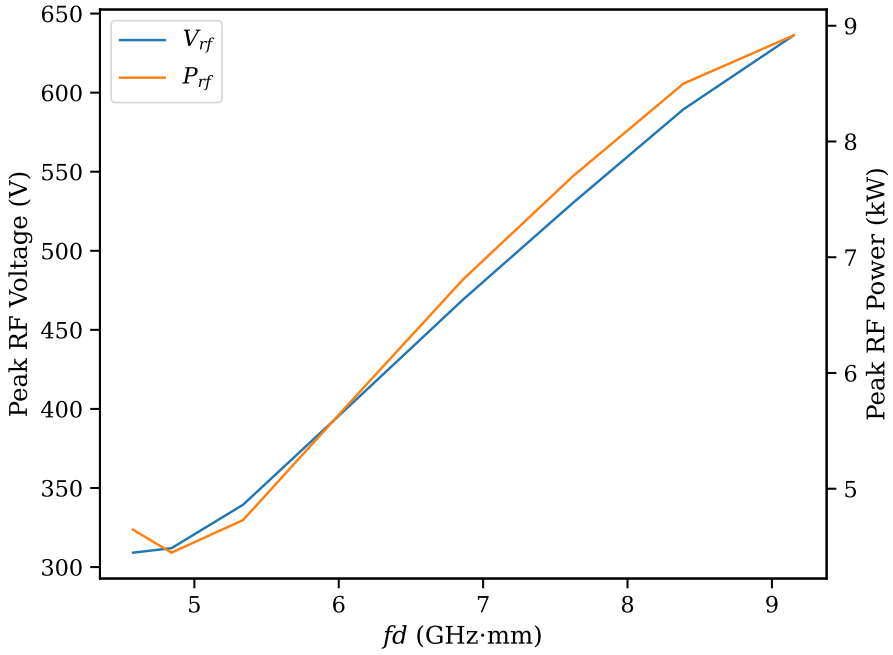

Figure 2.11: Simulated breakdown threshold of the stepped coaxial transmission line.

At the ends of the transmission line are the 50-Ω input/output segments. In the experiment, these regions adapt to the external microwave hardware and allow power to enter and leave the vacuum chamber. Two quarter-wave transformers, each between the 50-Ω segments and the multipacting region, ensure an impedance match across the transmission line. Since the diameter of the outer conductor is held constant at 19.1 mm, any changes in d will alter the impedance of the multipacting region. As such, the quarter-wave transformers are adjusted for each value of d that is examined.

During these simulations, the discharge is driven by a 3.05-GHz signal that enters and leaves the system through two wave-ports at either end of the transmission line. At the beginning of the simulation, the multipacting region is seeded with a cloud of 10,000 electrons with randomized position, energy, and direction.

We use the methodology described in Sec. 2.1 to determine the multipactor breakdown threshold of the experimental transmission line. These data are shown in Fig. 2.11. Since the impedance of the transmission line is not constant with respect to d, for convenience the breakdown threshold is presented in both voltage and power units. Note that the power-axis is not perfectly proportional to the square of the voltage-axis (as opposed to the axes in Fig. 2.5); this is because the transmission line's characteristic impedance varies with respect to d. From these simulations, we see that the breakdown threshold ranges from 4 to 9 kW. Although these data show that this experiment requires relatively high power levels (compared to other multipactor experiments [17, 20, 21]), the

multipactor breakdown threshold is consistently below the 10-kW limit imposed by our experimental microwave hardware. This added margin also provides space for testing multipactor suppression technologies; the breakdown threshold can be significantly increased and still be experimentally measurable.

CHAPTER 3

Experimental Apparatus

In this chapter, we discuss the design and construction of the coaxial multipactor test cell, which is photographed in Fig. 3.1. This work is an expansion of our previous discussion in the *Review of Scientific Instruments* [22] and includes updates to our experimental hardware.

3.1 Vacuum Chamber and Transmission Line

At its heart, the multipactor test cell consists of a coaxial transmission line suspended in a vacuum chamber. This is depicted in Fig. 3.2 which displays CAD renderings of the vacuum chamber and transmission line structure. A block diagram representation of the vacuum system is also shown in Fig. 3.3 Vacuum is provided by a Varian Turbo-V 250 turbomolecular pump backed by an Agilent IDP-15 dry scroll pump. When the chamber is vented to atmospheric pressure, a gate valve isolates the turbomolecular pump and prevents it from needing to be deactivated. A separate roughing line allows the scroll pump to bring the chamber to pressures below 100 mTorr before opening the gate valve. Pressure measurements are provided by a Kurt J. Lesker KJL-6000SS thermocouple gauge (pressures above 1 mTorr) and a Kurt J. Lesker KJL-C354401YE ionization guage (pressures below 1 mTorr); base pressures are consistently below 1 $\mu\mathrm{Torr}$.

The multipactor test cell uses a stepped coaxial transmission line whose design was based on the simulations discussed in Chapter 2. Multipactor is concentrated in the central region where the gap between the inner and outer conductors is minimized. Two quarter-wave transformers adapt this central multipacting region to the 50-Ω segments at the input and output of the chamber. The transmission line is designed such that both the inner and outer conductors can each be separated into three segments, as is shown in Fig. 3.4. This segmented structure allows the central multipactor region to be interchangeable. This has two main purposes: adjusting the gap between the inner and outer conductors (and thus fd) requires replacing the center segment of the inner conductor, and the segmented outer conductor enables the placement of multipactor-suppressive technologies over the multipacting region.

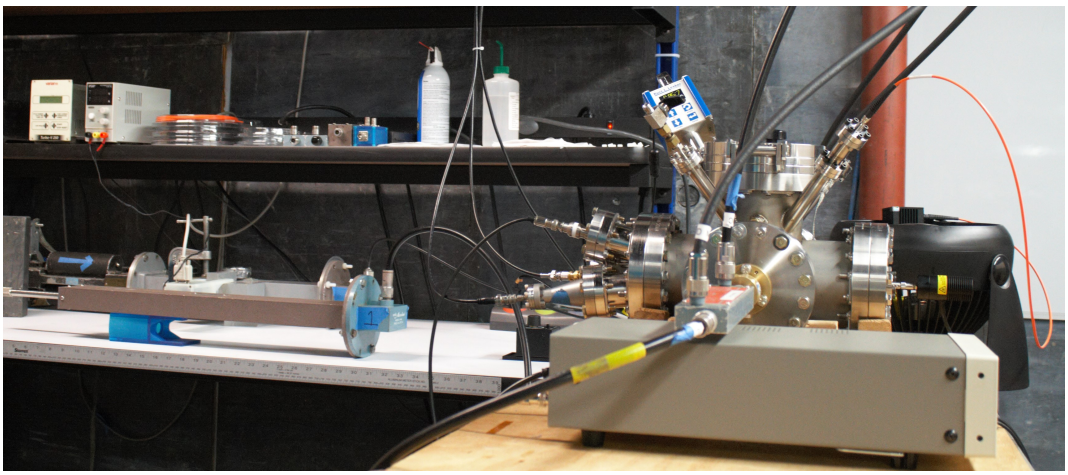

Figure 3.1: Photograph of the complete multipactor test cell.

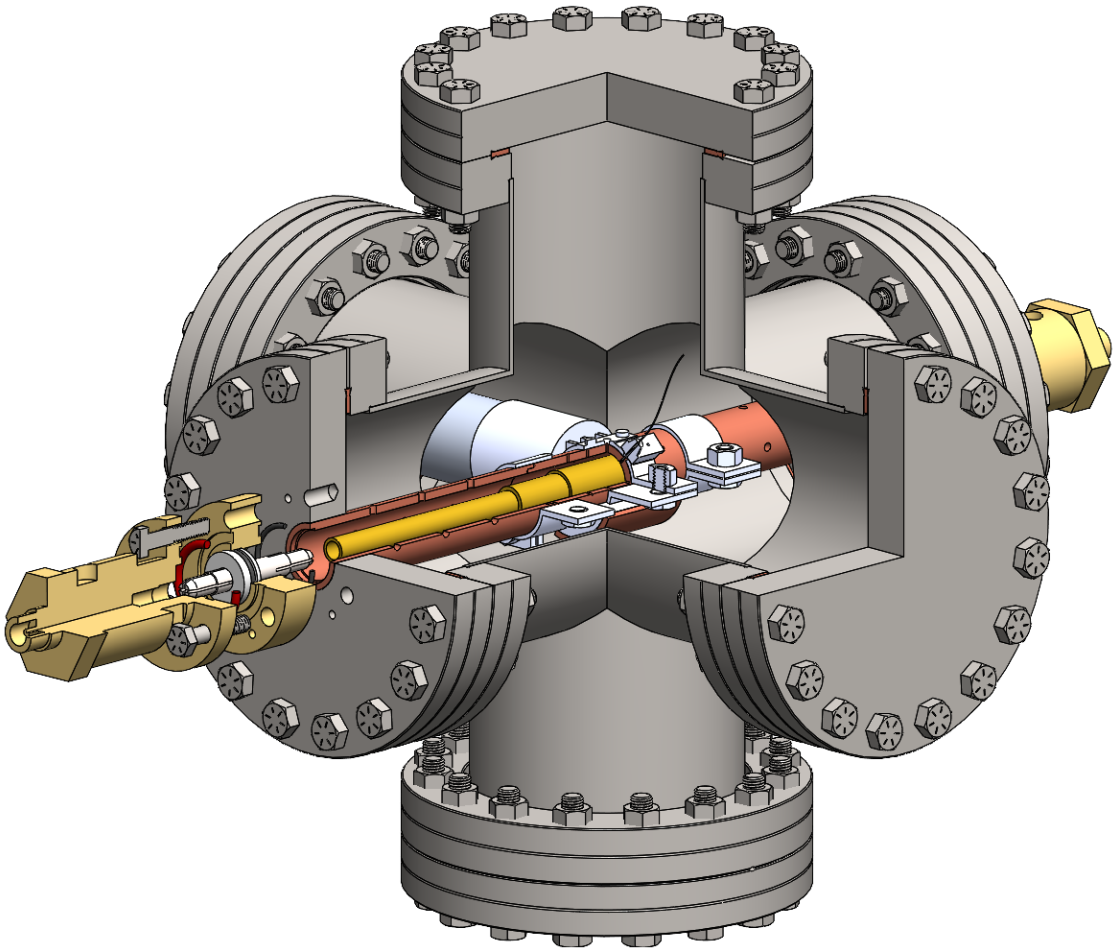

Figure 3.2: CAD rendering of the full coaxial multipactor test cell. A cutaway view reveals the internal structure of the coaxial transmission line and the placement of the electron diagnostics and UV seeding source. An exploded view highlights the connection between the MYAT adapters and the internal transmission line.

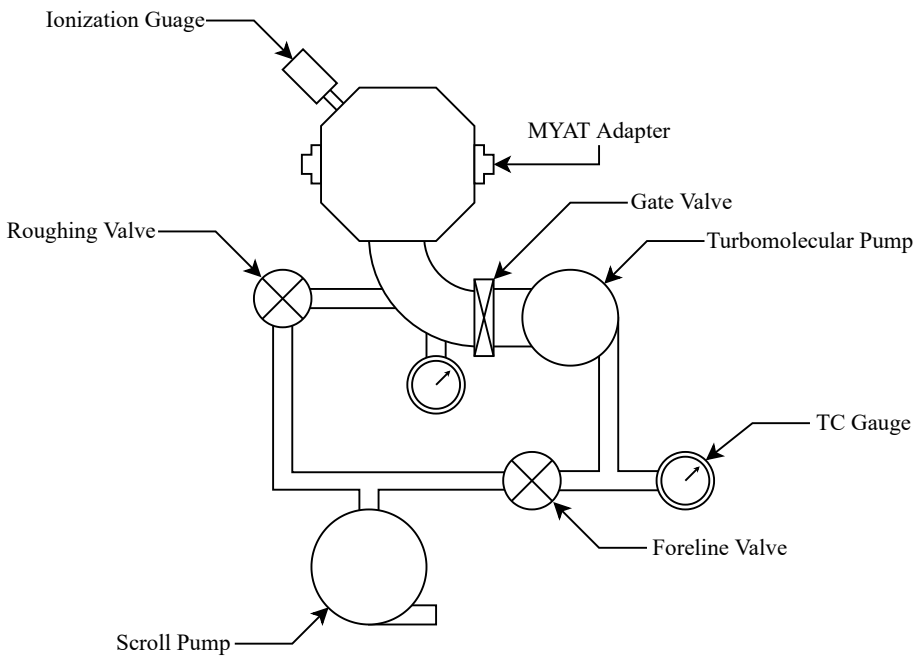

Figure 3.3: Block diagram representation of the vacuum system for the multipactor test cell.

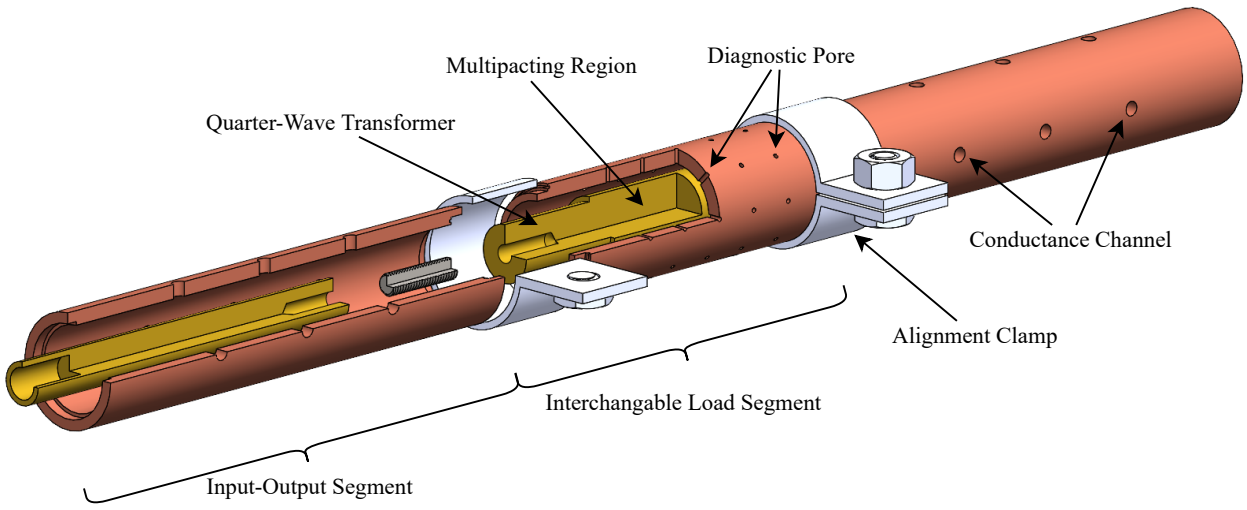

Figure 3.4: CAD rendering of the coaxial transmission line. Cutaway and exploded views highlight the construction of the segmented inner and outer conductors.

At the input and output of the chamber, two MYAT 101-059 reducers adapt external N-type connections to the internal transmission line. Although these adapters are hermetically sealed, additional MYAT 101-050 gas barrier flanges act as RF windows separating atmosphere from vacuum. These ensure that the internal structure of the Type-N adapters remain at atmosphere, and prevent multipactor from occurring inside of them.

The outer conductor has a constant inner diameter of 19.1 mm along its full length. As is illustrated in Fig. 3.4, the three segments of the outer conductor are designed to interlock. Two 3D-printed ring clamps reinforce the connections' seams and prevent the segments from separating. Indium wire (not pictured) acts as a conductive gasket to ensure good electrical contact between the segments. The center segment has an array of 1-mm pores that provide diagnostic access to the interior of the multipacting transmission line. A set of 3.18-mm channels in the two input/output segments ensure good vacuum conductance between the transmission line and the rest of the vacuum chamber.

The three segments of the inner conductor, as illustrated in Fig. 3.4, are connected using two short segments of threaded rod. The center segment of the inner conductor includes both the multipacting region and the two quarter-wave transformers. Since the outer conductor has a constant diameter and the quarter-wave transformers can only pass a single frequency, fd is altered by adjusting the radius of the central multipacting region. The two 50-Ω segments have a constant diameter of 9.53 mm. Insets at their ends are press-fit with the MYAT adapters.

Cold tests of the coaxial transmission line were performed to demonstrate good impedance matching across the multipactor test cell. These data were measured using an HP 8772D vector network analyzer (VNA) and were calibrated using an Agilent 85052-D SMA calibration kit; additional effects due to the use of SMA-to-N-type adapters were separately measured and compensated for. These cold test results are shown in Fig. 3.5 with S_{11} (reflected power) in **(a)** and S_{21} (transmitted power) in **(b)**. In general, these structures show reasonably good performance. When averaged over each of the five values for d, $S_{11} = -13.3$ dB and $S_{21} = -0.27$ dB. These suggest that relatively little power is lost in the structure (5.95% overall); however, it must be taken into account when determining the amount of power delivered to the multipacting region. If we assume that the loss in each MYAT adapter and quarter-wave transformer pair is equal, then we can assume that the corrected power, P_{MP}, delivered to the multipacting region is

$$P_{MP} = P_{in} + \frac{S_{21}}{2} \tag{3.1}$$

where P_{in} is the total power input into the vacuum chamber.

The quarter-wave transformers were designed based on CST Microwave Studio simulations (shown as dashed lines in Fig. 3.5) and are intended to resonate at 3.05 GHz. However, the as-built

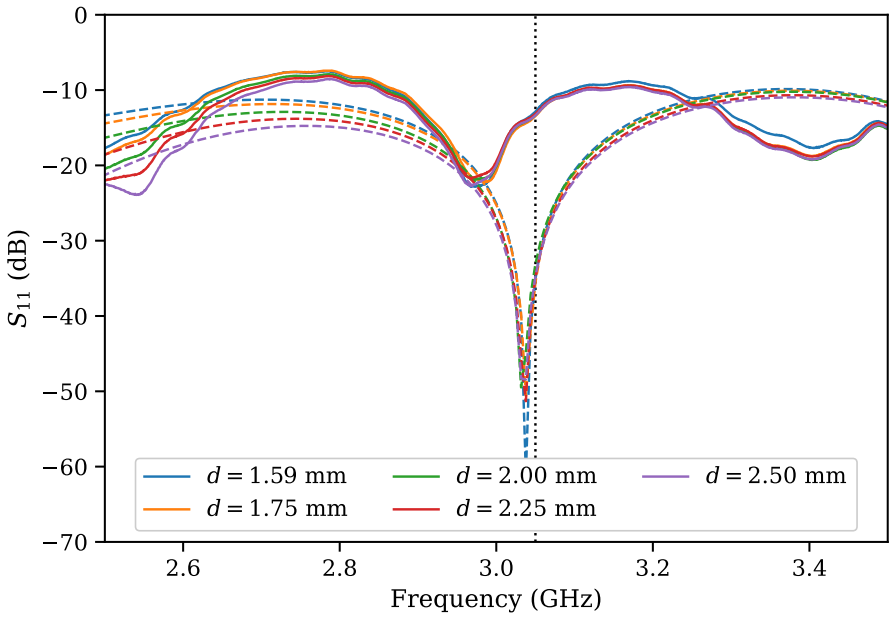

(a) Reflected power, S_{11}

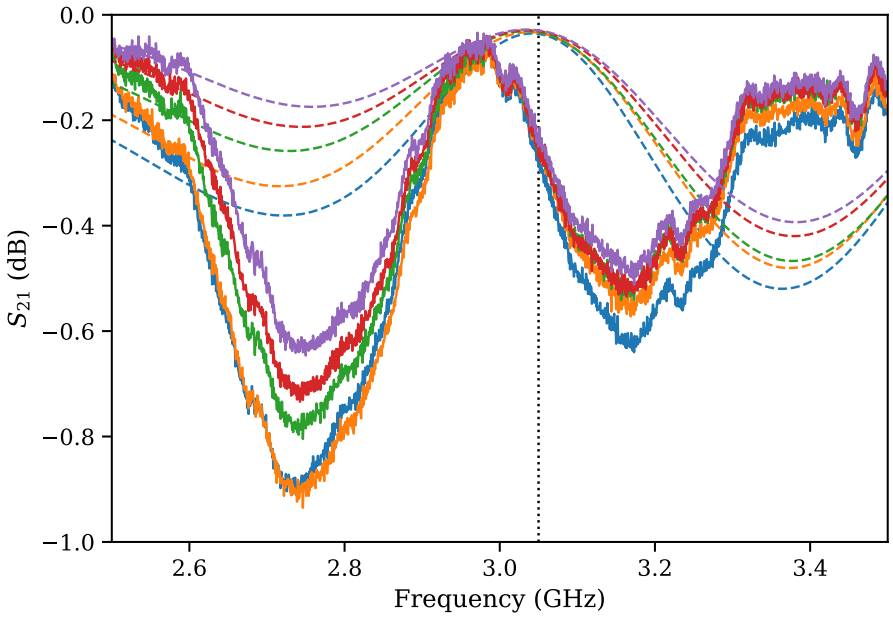

(b) Transmitted power, S_{21}

Figure 3.5: Results from cold tests of the coaxial transmission line. Data for S_{11} and S_{21} for each value of d used in the experiment are shown in **(a)** and **(b)**, respectively. A vertical, dotted line represents the operating frequency of $f = 3.05$ GHz. These data are compared to CST Microwave Studio simulations, which are indicated by dashed lines.

transformers resonate at only 2.96 GHz, suggesting a minor error in their design or manufacture. Such an error is not unexpected since quarter-wave transformers are extremely sensitive. The length-scale of one of these transformers is on the order of one quarter-wavelength, and an error of less than 0.5 mm can cause the observed shift in frequency [93].

3.2 RF Power Generation and Measurement

The multipactor test cell uses an external microwave source to generate the RF fields that drive the discharge. A block diagram of the microwave circuit is shown in Fig. 3.6. RF power is generated by an E2V MG5223F S-band magnetron. This magnetron, originally intended for marine radar applications, emits 2.5-μs, 40-kW pulses[1] of microwaves at a frequency of 3.05 GHz into WR-284

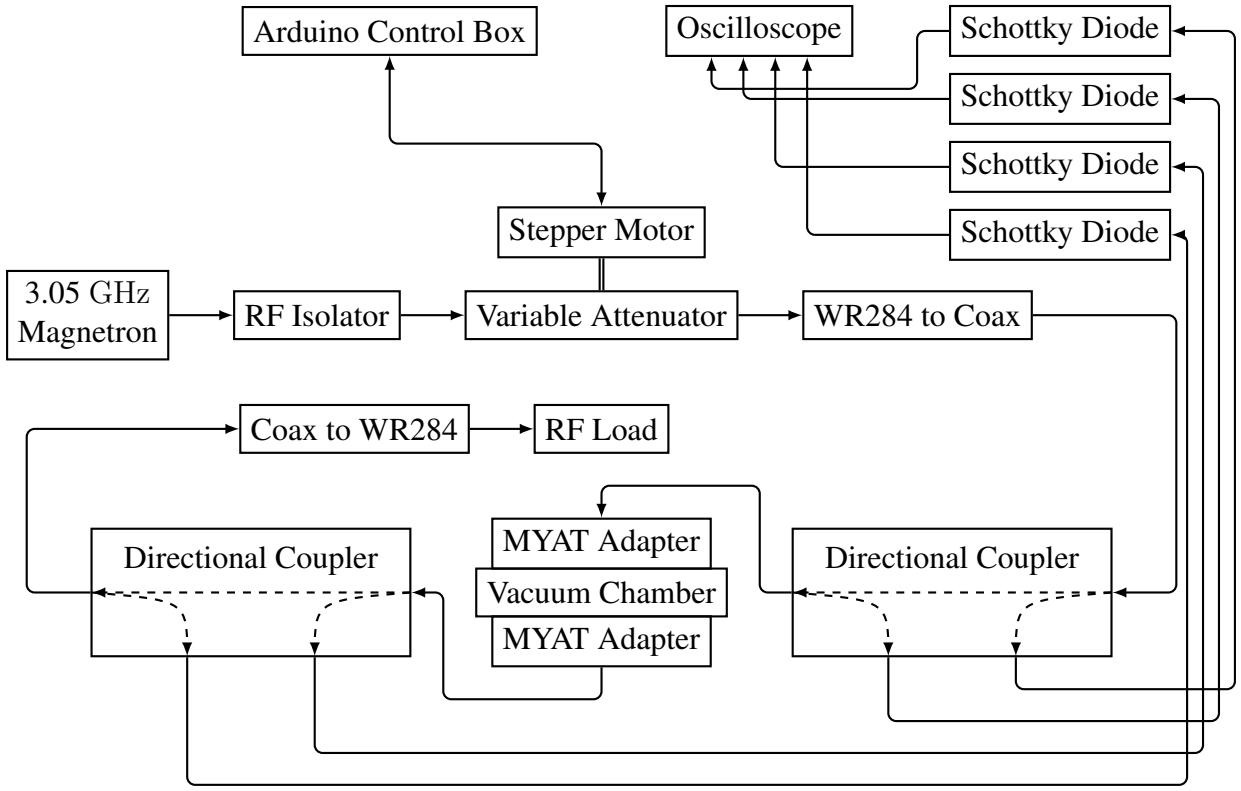

Figure 3.6: Block diagram representation of the microwave hardware used in the experiment.

[1]The pulse-length reflects the time at peak RF-power. Due to the long rise time that occurs when using the Scandinova modulator, this peak power is defined based on when the Schottky diode signal is above 90% of its peak value. This is discussed further in Appendix A.

rectangular waveguide. Two high voltage modulators have been used to drive the magnetron at various stages of the experiment. Earlier tests were performed using the Stanford Model 344M Pulse Modulator, a 40-kV, 30-A hard-tube modulator. Final experiments used the 70-kV, 100-A Scandinova M1 solid-state modulator. The characteristics of these two modulators, as well as their effect on the RF and multipactor diagnostic signals, are discussed further in Appendix A.

A waveguide isolator placed at the magnetron output protects the source from power reflected by the rest of the system. Power levels are then controlled by a variable attenuator that is remotely-adjustable by an Arduino-controlled stepper motor. The design and operation of this stepper-motor controller is discussed in more detail in Appendix C.

At the end of the input leg of the microwave circuit, the signal is converted from waveguide to a coaxial, Type-N connection. RF power then passes through an RG-9 cable into a Narda 3022 directional coupler before entering the vacuum chamber. A second directional coupler at the chamber output samples the RF signal before it is adapted back into the rectangular waveguide and deposited in an absorptive load. The two directional couplers sample the forward, reflected, and transmitted power signals which are then measured using several HP/Agilent 8472B Low Barrier Schottky diodes. These diodes are calibrated relative to two calibrated bolometers using the procedure described by Greening [94] and updated in Appendix B.2. Calibration of all other RF components, particularly of the line attenuation used to reduce the power exposed to the Schottky diodes, were initially performed using an HP 8772D vector network analyzer; these calibrations have an uncertainty on the order of 0.2 dB. During later experiments, higher precision measurements of the line attenuation were performed using the calibrated bolometers with the procedure described in Appendix B.1. Due to a reduction in the usage of coaxial gender adapters, these measurements have an uncertainty of only 0.1 dB

The Narda directional couplers have a peak-power limit of 10 kW; this sets the upper limit for experiments conducted on the test cell. Higher power measurements[2] were performed successfully and the couplers were not observed to undergo breakdown. In addition, routine measurements on a vector network analyzer did not show any significant shift in directivity or insertion loss, implying that the couplers saw no long-term damage or loss in performance.

3.3 Electron Seeding and Diagnostics

The array of pores in the outer conductor enable the placement of a number of diagnostics around the multipacting region. The multipactor test cell uses several electron diagnostics to directly detect and measure the multipactor discharges. These diagnostics, whose typical placements are illustrated

[2]Higher power measurements have become necessary for some multipactor-suppression tests where the breakdown threshold approaches the directional couplers' 10-kW limit.

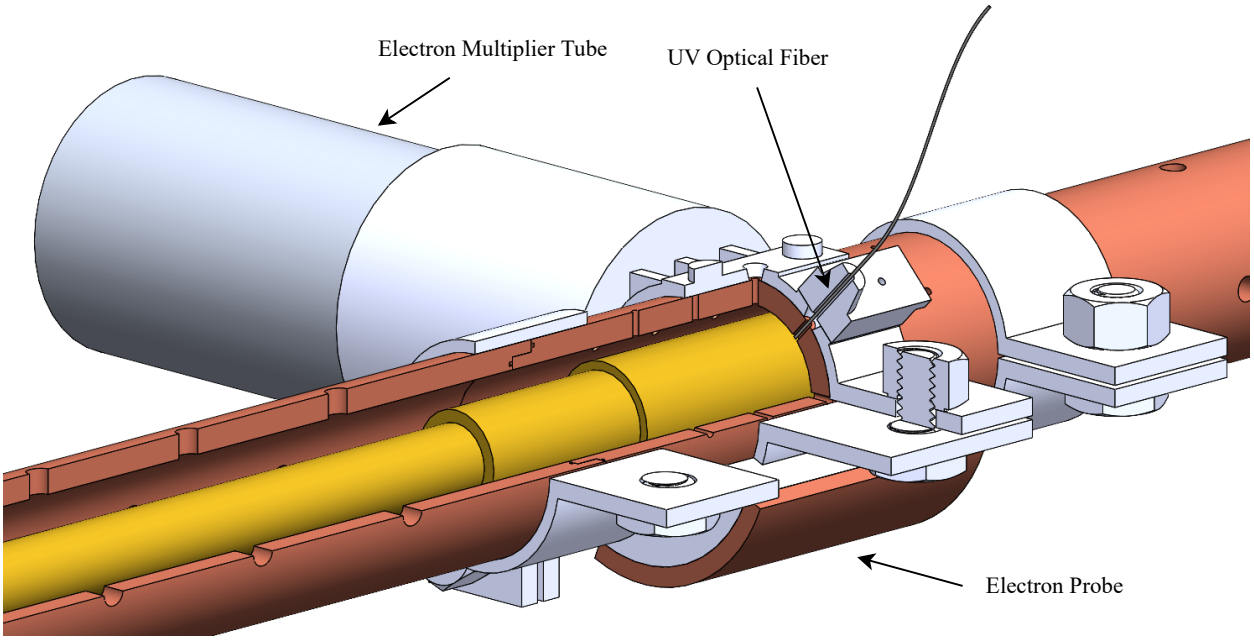

Figure 3.7: CAD rendering of the placement of the electron diagnostics and UV seeding source.

in Fig. 3.7, fall under two categories: electron probes and electron multiplier tubes (EMTs). The two sets of diagnostics operate on similar principals; both collect a sample of the multipactor electron current and convert it into voltages that are read on an oscilloscope. In addition to these diagnostic systems, Fig. 3.7 also shows the placement of an optical fiber for coupling UV photons from an external LED for generating seed electrons.

3.3.1 Ultraviolet Seeding Source

A reliable seed electron source is essential for characterizing multipactor. This is particularly important when observing discharges near the breakdown threshold where relatively few electrons will satisfy the multipactor resonance condition. In the multipactor test cell, this seeding is achieved by using two ultraviolet LED sources to stimulate electron emission inside the transmission line. The seed electrons are emitted when the ultraviolet photons undergo photoelectric absorption on the copper transmission line surfaces.

Two UV LEDs are used as electron seeding sources. Polycrystallic, oxygen-free copper has a work function of approximately 4.4 eV [95], so 265-nm (4.679-eV) photons emitted by the LEDs should stimulate sufficient photoelectric emission to trigger multipactor [62, 96]. The first UV source is a Mightex FCS-0265-001 fiber coupled LED, driven by a Mightex SLC-MAO2-U software-controlled driver. This LED is operated in continuous mode. A second LED (Thorlabs

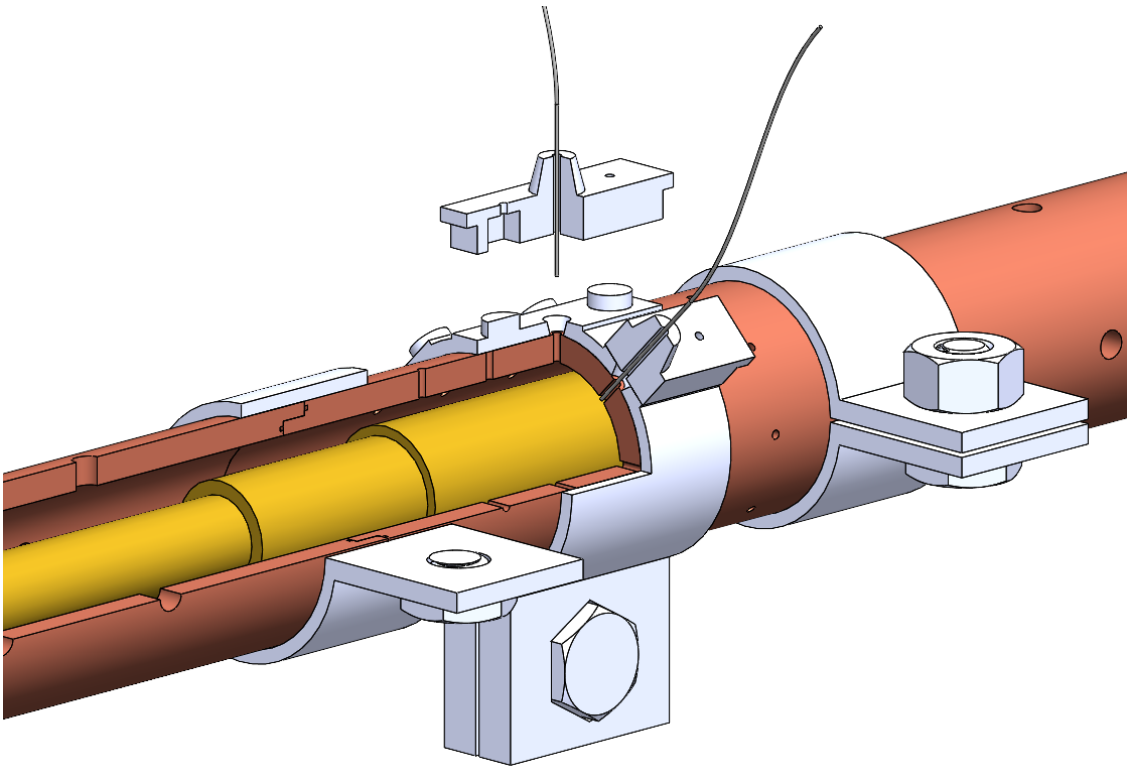

Figure 3.8: CAD rendering of the 3D-printed connectors for securing the UV fibers to the coaxial transmission line

model M265L5) is operated in 1-ms pulses, timed such that they end 5 µs after each microwave pulse. This pulsed operation minimizes LED heat-up and maximizes brightness [97].

The UV photons from each LED source are coupled into the vacuum chamber via two UV fiber SMA feedthrough adapters (Accuglass model F04UV-133 and Kurt J. Lesker model FIBM1-UV00-04-S-2). On the atmosphere-side of the system, the Mightex LED is connected to one of the feedthroughs using a Thorlabs M113L01 solarization-resistant multimode patch cable, which contains a 400 µm, 0.22 NA fiber (Thorlabs model FG400AEA). The Thorlabs LED is connected directly to the second fiber feedthrough.

Inside the vacuum chamber, a bare FG400AEA fiber adapts the SMA connection at the two feedthroughs to custom, 3D-printed connectors.[3] These custom connectors, pictured in Fig. 3.8, secure the UV fiber to the multipactor transmission line using 3D-printed, LEGO-style connection points [98]. These fiber attachment points are frequently incorporated into the support structures for the EMTs and electron probes to ensure the seeded multipactor discharges occur near the electron diagnostics. This can be seen in Fig. 3.7 which shows the arrangement of all of the diagnostic systems.

[3]Printed in Formlabs Durable V2 resin using a Formlabs Form2 3D-Printer.

The Mightex UV source is designed to provide 400 $\mu\mathrm{W}$ of 265-nm photons when coupled with the 400 $\mu\mathrm{m}$ fiber. If we assume a quantum efficiency on the order of 10^{-3} [99], this should correspond to a seed electron current of approximately 85 nA. A similar number of electrons should also be generated by UV photons from the Thorlabs LED. This suggests that the combination of the two LEDs should generate seed electrons on the order of 10^6 $\mu\mathrm{s}^{-1}$. While this should be a sufficient number of electrons to immediately trigger multipactor during each RF pulse, in practice long wait-times (on the order of 10s of seconds to a few minutes) are observed at power levels near the breakdown threshold. This is likely because the true source rate is much lower than our estimates.

Several factors can reduce the generation of seed electrons in the multipacting region. The most obvious suspect is reduced intensity of the UV photons. Aside from attenuation within the optical fibers, the UV intensity is highly sensitive to the temperature of the LED source. To minimize heat-up, the Mightex LED is placed directly over a large fan while the Thorlabs source is pulsed at a low duty cycle ($< 10\%$). The seed electron rate is also potentially reduced due to uncertainties in the quantum yield and work function of the copper surfaces. Although the transmission line is machined from oxygen free copper, it is frequently exposed to air and is never baked. This means that significant oxide layers form on all of the surfaces. These oxide layers can significantly increase the work function; simulations from Sami *et al.* showed that a CuO monolayer can increase the work function to values ranging from 5.34 to 5.75 eV (depending on crystal plane) [100]. This is well above the energy of the two UV sources, suggesting that even small oxide layers can significantly reduce UV-stimulated seed electrons.

Another interesting item to note is that once an initial multipactor discharge is observed, subsequent RF pulses will undergo multipactor. This is particularly prominent when the UV LEDs are disabled; when operated at 10 kW (nearly double the breakdown threshold power), the multipactor test cell has been observed to resist breakdown for nearly a minute. However, once a naturally occurring seed electron appeared, multipactor began to occur during a majority of RF-pulses.

3.3.2 Electron Probe

The electron probes are capacitive sensors that collect charge from the current of multipactor electrons leaking from the transmission line. Figure 3.9 shows a cutaway view of an electron probe placed around the coaxial transmission line. Each electron probe has two main components: a 3D-printed[4] support structure and a copper collector plate. During multipactor, some of the multipacting electrons leak out of the transmission line through 1-mm perforations in the outer conductor. These electrons will then pass through larger electron channels in the 3D-printed structure before striking the collector plate. A coaxial cable attached to the collector allows this small electron current to be

[4]Printed in Formlabs Durable V2 resin using a Formlabs Form2 3D-Printer.

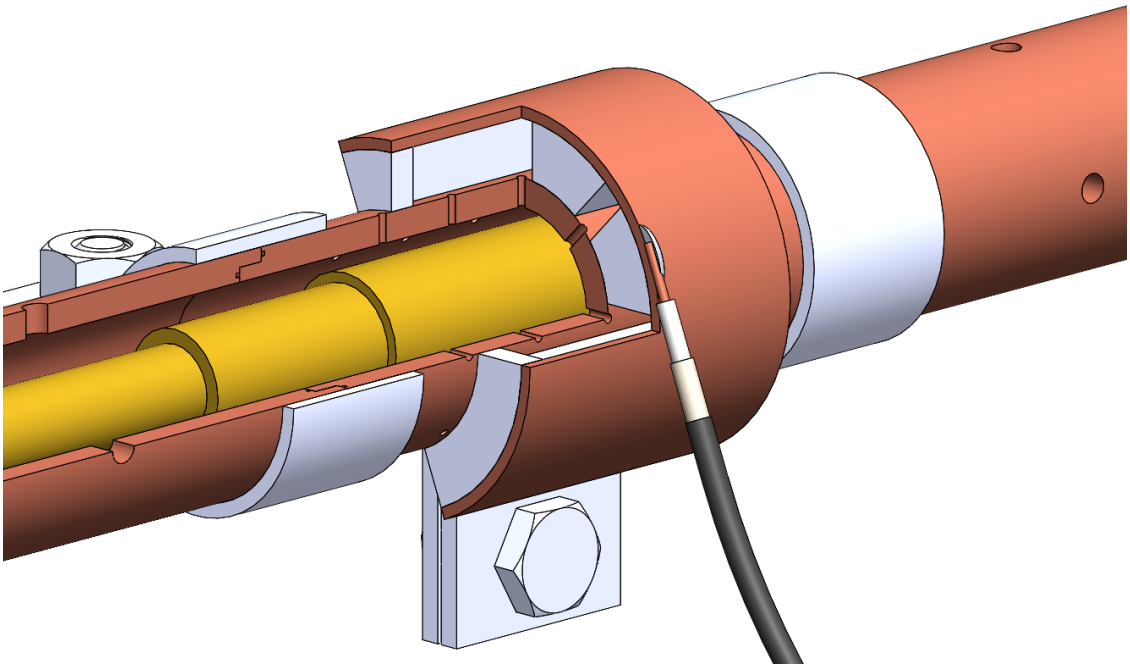

Figure 3.9: Cross-sectional CAD rendering of the basic electron probe design. More complex geometries can be manufactured to accommodate placement of other diagnostic systems.

coupled externally from the chamber and measured on an oscilloscope. A 4 MHz low pass filter was placed at the input of the oscilloscope to remove high frequency interference from the probes' output signals.

The basic structure of the electron probes is reminiscent of a simple capacitor: two conductors (the collector plate and the grounded outer conductor) separated by a dielectric (the 3D-printed support structure). Since the probes' capacitance should be relatively constant (approximate measurements using a QuadTech 1730 LCR Digibridge suggest that the electron probes have a capacitance on the order of 50 nF) their response is highly dependent on their termination impedance. When terminated with a low impedance (50 Ω), $RC \approx 2.5$ µs. Since RC is on the order of the RF-pulse length, this will prevent the probes from charging significantly over time. Thus, this "fast" mode operation will result in a voltage signal that reflects the current of electrons striking the collector plate.

Conversely, "slow" mode operation will leverage a high termination impedance to cause the probe to gain an electrostatic charge over time. If the probe is terminated with $R = 1\ \mathrm{M}\Omega$, then $RC = 50\ \mathrm{ms}$; this is far longer than the RF pulse-length. When the multipactor electrons strike the collector plate, they will charge it up like a capacitor; this is indicated by an increasing voltage signal. Once multipactor ceases, no additional charge is collected, and the voltage signal will slowly dissipate. However, since RC is much longer than the pulse-length, this decay will be negligible

at the diagnostic signals' time-scale. Thus, the presence of multipactor will be indicated by a DC offset after the end of the RF pulse. This can serve as a reliable, binary indicator for multipactor. This will be discussed further in Sec. 4.1 when we examine the diagnostics' response to multipactor.

While both modes of operation produce signals that are analogous to each other, the choice of using one over the other is dependent upon several practical considerations. The electron probes are relatively insensitive, especially when compared to the EMTs. This is because they have no internal gain mechanism to amplify the multipactor current signal. Since the probes' signals are very small, they are highly sensitive to electromagnetic interference from external sources, particularly when operating in the fast mode (low termination impedance). When operating in the fast mode, an electron probe's signal amplitude may be very small ($\sim$5 mV). Such small signals can easily be masked by the noise generated by the high voltage modulator switching on and off. On the other hand, the DC offset produced in the slow mode (high termination impedance) will remain as a reliable indicator for multipactor. This interference effect is discussed in further detail in Appendix A where we examine signal noise introduced to the diagnostic channels by the operation of the high voltage modulator.

3.3.3 Electron Multiplier Tube

Electron multiplier tubes are ideal devices for detecting and measuring the multipactor electron current. Figure 3.10 shows a diagram of the basic structure of a typical EMT [38, 39]. Electron multiplier tubes amplify an electron current through the same mechanism as multipactor. When electrons enter the tube, they will impact a dynode's surface and undergo secondary electron emission. Instead of using alternating electric fields as in multipactor, each dynode in an EMT is

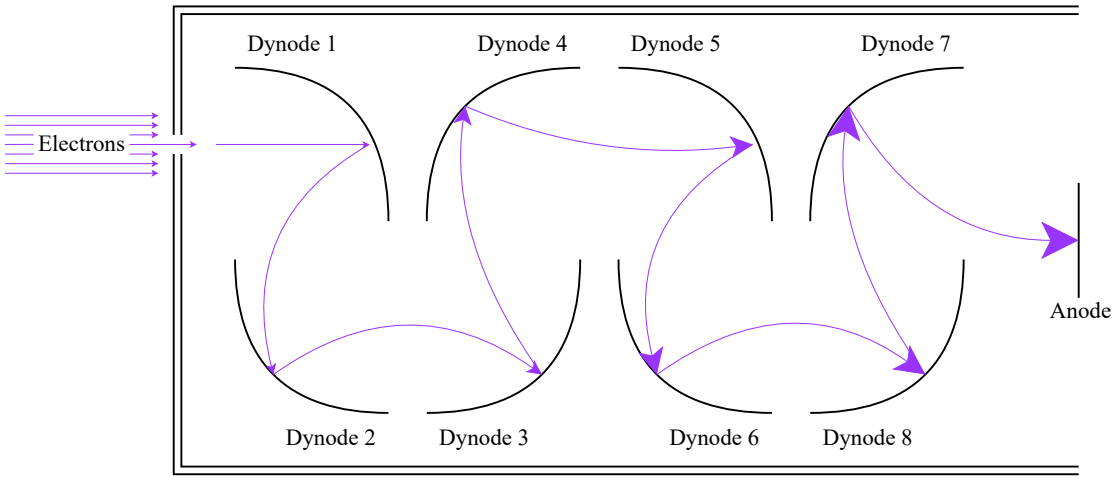

Figure 3.10: Basic diagram of a typical electron multiplier tube.

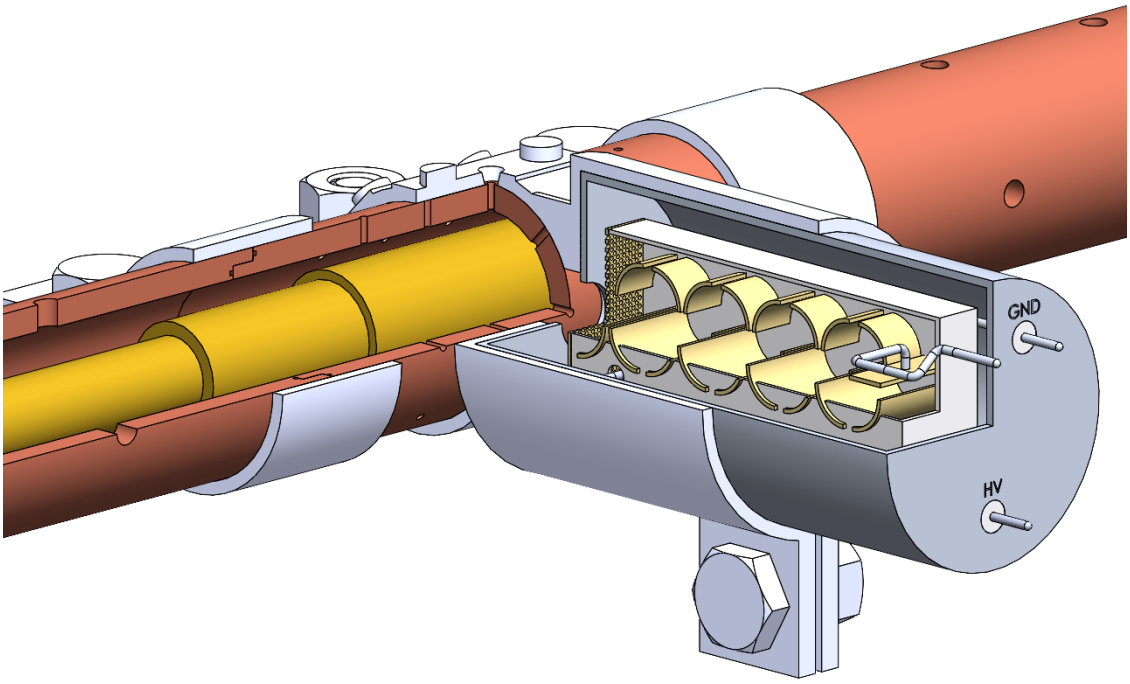

Figure 3.11: CAD rendering of the placement of the Hamamatsu EMT.

charged to a successively higher electrostatic potential. The re-emitted secondary electrons are then focused onto a second dynode. Additional dynode stages further amplify the electron current before it is collected at the anode and measured on an oscilloscope.

Two electron multiplier tubes are available for use in the multipactor test cell: an ETP model AF566 and a Hamamatsu model 5150-10. Both tubes provide a very similar signal response to multipactor and are effectively interchangeable. Figure 3.11 shows the placement of the Hamamatsu EMT around the coaxial transmission line. The EMTs are secured to the outer conductor by a 3D-printed[5] support structure, aligned such that one of the diagnostic pores is facing the EMTs' first dynode. High voltage for operating the EMTs is generated by a Stanford Research Systems PS350 5-kV power supply. Output from each of the EMTs' anodes is coupled to a 50-Ω-terminated RG-58 coaxial cable and recorded on an oscilloscope.

[5]Printed in Formlabs Durable V2 resin using a Formlabs Form2 3D-Printer.

CHAPTER 4

Experimental Characterization of Multipactor Discharges

In this chapter, we present experimental results from initial testing of the multipactor test cell. This includes a discussion on how the properties of the multipactor discharge can be inferred from the various diagnostic signals. We also demonstrate a method for characterizing the multipactor self-conditioning process and how this affects measurements of the breakdown threshold.

4.1 Multipactor Behavior and Response from Diagnostics

During multipactor, when the electrons are accelerated by the RF fields, they have a distinct effect on any signals passing through the transmission line. This effect is illustrated in Fig. 4.1 which shows the calibrated Schottky diode signals for the RF power delivered to, reflected by, and transmitted through the test cell. During multipactor, the power that is reflected by the transmission line is reduced. This is not due to an improvement in the impedance matching.[1] Instead, the multipactor electrons are absorbing power from both the forward and reverse waves [101], and this energy is deposited into the transmission line as heat. Since the reflected power tends to be particularly sensitive to multipactor, we will use this signal to examine the discharge's evolution. We break this down into three distinct phases: the pre-discharge phase, the growth phase, and the saturation phase.

During the pre-discharge phase, the multipactor discharge has either not yet occurred or is too small to observe. This phase is characterized by the time spent waiting for the initial seed electron that triggers an avalanching discharge. Once the seed electron appears and multipactor occurs, the electron cloud will continue to grow until it is absorbing sufficient energy to significantly perturb the power signals. When the discharge reaches this point, we observe a significant drop in the reflected power signal, as is shown in Fig. 4.1. During this growth phase, the increasing space charge effects

[1] During a conventional plasma breakdown, one would expect an *increase* in reflected power. This is because plasma will alter the transmission line's characteristic impedance [102]; the resultant mismatch causes the increased reflection. However, in this experiment this effect appears to be overshadowed by the power deposited into the electrons.

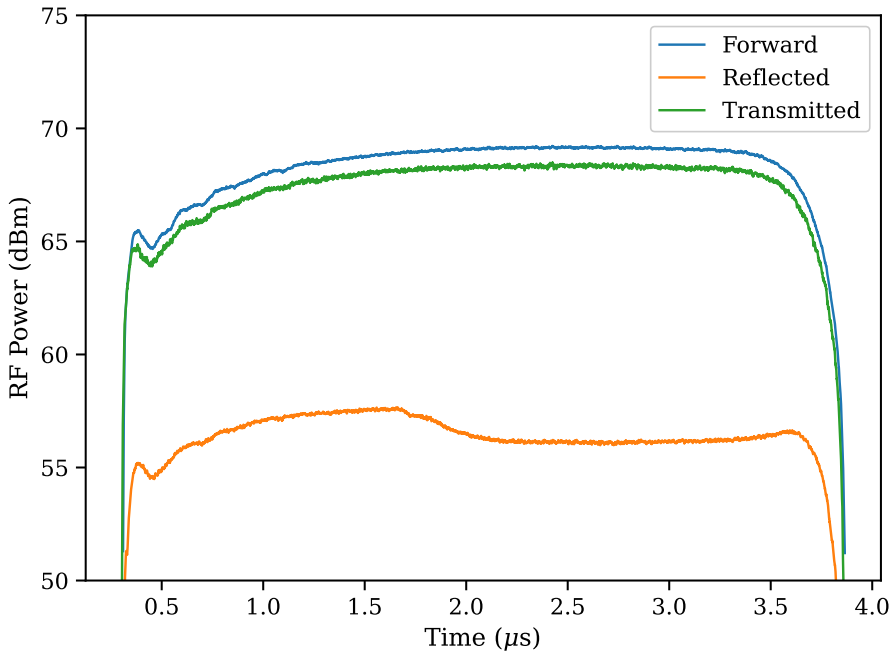

Figure 4.1: Example of the forward, reflected, and transmitted power signals during a multipactor discharge.

will eventually become sufficiently large to disrupt the electron motion and break the multipactor resonance. Once the discharge reaches this saturation point, it will cease growing. We can see this transition occur in Fig. 4.1 when the reflected power signal levels off and reaches a new flat-top.

We can compare this interpretation of our power signals to the electron diagnostics. Recall that these systems directly sample the current of electrons striking the outer conductor, which itself is proportional to the overall electron density within the transmission line structure. As a result, their signals should correspond to the evolution of the multipactor discharge we inferred from Fig. 4.1. This is particularly evident when we examine data from the electron probe operating in the fast mode. Figure 4.2 shows a comparison between the forward and reflected power signals and the fast mode electron probe signal. A vertical dotted line represents the point when the electron probe signal begins. Once the reflected power signal indicates that the discharge has reached the growth phase, the probe signal begins to reflect the current of electrons striking the collector plate. This signal continues to increase before leveling off when the discharge saturates. Once the RF-pulse is terminated, the electron probe no longer collects any current and the signal returns to noise levels. This behavior perfectly mimics the evolution of the electron population we expect during a multipactor discharge.

Note that the raw electron probe signal in Fig. 4.2 has a very poor signal-to-noise ratio. While simple post-processing algorithms (described in Appendix A) can reveal the true probe signal, these

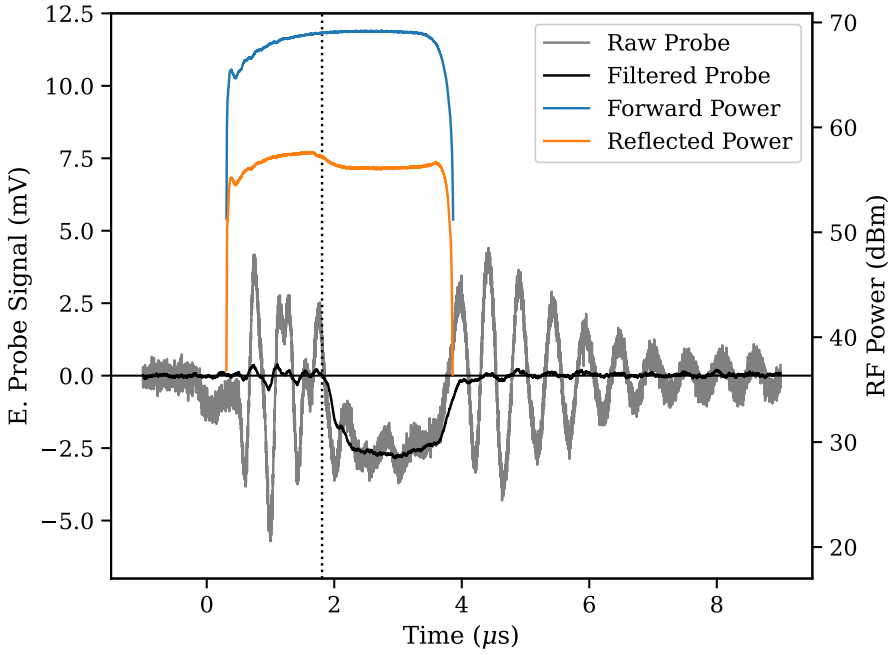

Figure 4.2: Example of the signal response of an electron probe operating in the fast (low termination impedance) mode. Also shown are the forward and reflected power signals to visualize the evolution of the multipactor discharge.

high noise levels limit the usefulness of fast mode operation for real-time signal monitoring. This is alleviated when we use the slow mode electron probe signal, which is shown in Fig. 4.3. A vertical dotted line, indicates the beginning of the electron probe's signal, highlighting the time correlation between the electron and power diagnostics.

When the electron probe is operating in slow mode, instead of measuring the current, its signal represents the cumulative amount of charge that is collected during a multipactor discharge. Once multipactor reaches saturation and the electron population stabilizes, the current collected by the probe will become constant. This causes the probe's signal to increase linearly with respect to time before reaching a constant DC-offset after the RF pulse ends and the discharge dissipates. Although Fig. 4.3 still shows significant noise, the DC-offset is easily recognizable in the raw, unfiltered signal. This becomes a very clear, binary indicator that an operator could use to detect the presence of multipactor in a pulsed system.

Figure 4.4 shows an example of a signal from the Hamamatsu electron multiplier tube. Signals from the ETP EMT exhibit similar behavior. Like the electron probe, the EMT directly samples the current of electrons impacting the outer conductor. However, this device does not appear to directly follow the evolution of the multipactor discharge. This suggests that the more complicated physical structure of the EMT has a relatively high capacitance that distorts the EMT's response

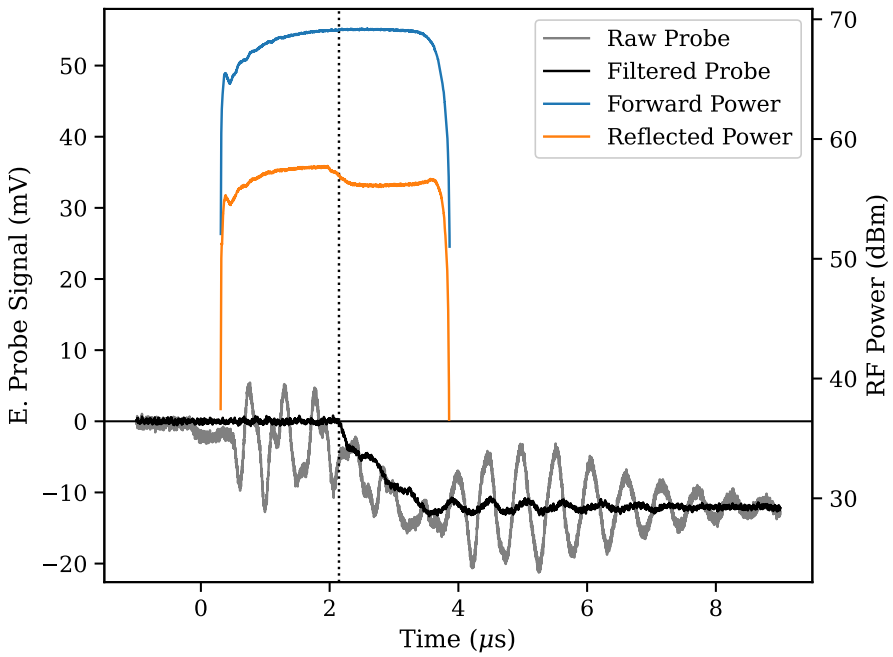

Figure 4.3: Example of the signal response of an electron probe operating in the slow (high termination impedance) mode. Also shown are the forward and reflected power signals to visualize the evolution of the multipactor discharge.

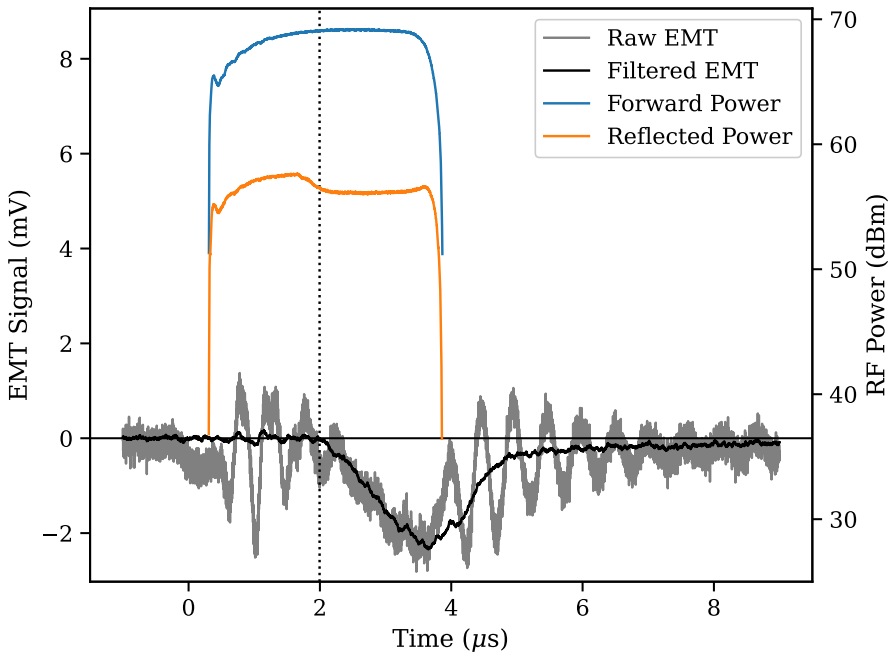

Figure 4.4: Example of the signal response of the Hamamatsu electron multiplier tube. Signals from the ETP EMT exhibit similar behavior.

to multipactor. Regardless, although the finer structure of the multipactor discharge appears to be lost, the EMT's high amplification factor allows it to respond to smaller multipactor discharges that occur closer to the breakdown threshold than those observable by the electron probe.

4.2 Multipactor Self-Conditioning

During multipactor discharges, electrons repeatedly bombard the transmission line surfaces. When electrons strike these surfaces, they can cause localized heating that may encourage the release of trapped gasses, and oxide layers on the metal surfaces may be removed. As the surface characteristics of the transmission line are altered, their secondary emission properties will also change. This can lead to a significant shift in the multipactor breakdown threshold.

This shift in breakdown threshold has been acknowledged for several decades and is known as multipactor self-conditioning [15, 74]. During this conditioning process, the multipacting electrons will "clean" the transmission line surfaces. In a copper transmission line structure like the one used in this experiment, this will remove surface impurities and reduce oxide layers. As we previously saw in Graves's experiment [16], "dirty" copper surfaces with an intact oxide layer will have a much lower multipactor breakdown threshold than a transmission line that has been rigorously cleaned and baked. In a similar vein, we expect the breakdown threshold to increase as a transmission line undergoes prolonged exposure to multipactor.

Experimentally, we investigated this phenomenon by measuring the breakdown threshold as a function of exposure to multipactor. During this process, we recorded several measurements of the breakdown threshold[2] before going to a higher power level and allowing the system to "cook" for a period of time. After this conditioning step, the threshold was remeasured. This process was repeated until we no longer observed increases in the breakdown threshold after further exposure to multipactor.

The results from this multipactor self-conditioning process are shown in Fig. 4.5. These data were generated by using the Stanford modulator driving the magnetron with 2-μs (at peak power) pulses at a repetition rate of 16.8 Hz, and they were measured using a 2-mm gap between the inner and outer conductors ($fd = 6.1\ \mathrm{GHz} \cdot \mathrm{mm}$). Figure 4.5 also shows a comparison with a prediction for the final breakdown threshold from CST PIC simulations. Between each data set, the system was allowed to rest in vacuum for a minimum of 22 h so the surfaces could decondition and reset.

Figure 4.5 shows that the breakdown threshold is inconsistent on a day-to-day basis and is well below the levels predicted by our simulations when the system has not yet undergone the conditioning process. However, after the first fifteen-minute-long conditioning step, the breakdown threshold increases very significantly before stabilizing after 45 min to 1 h of total multipactor

[2]The procedure for measuring the breakdown threshold is discussed below in Sec. 4.3.

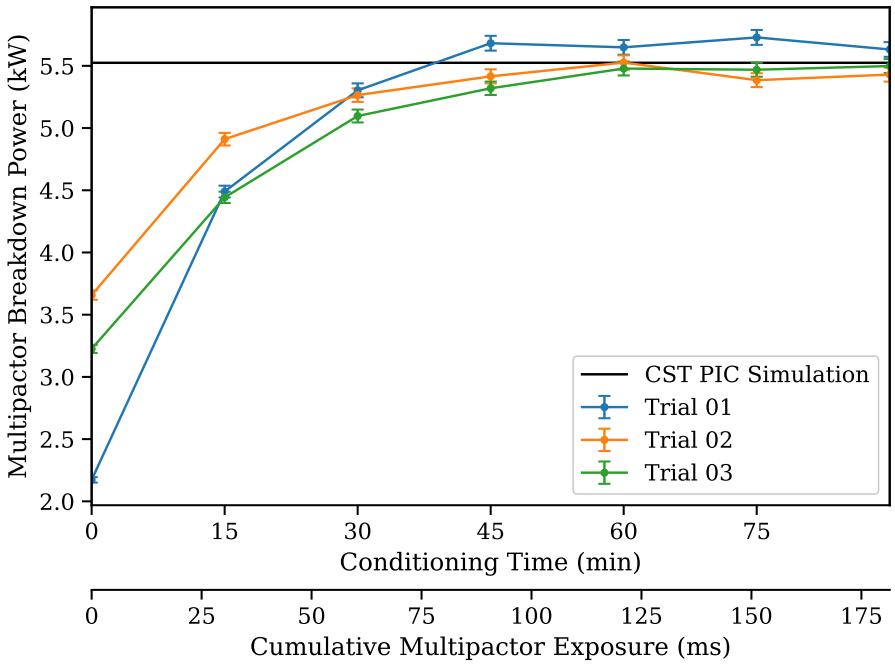

Figure 4.5: Multipactor breakdown threshold as a function of conditioning time. A black, horizontal line represents the breakdown threshold predicted by CST PIC simulations using SEY data for non-baked copper. These data are for the case where $fd = 6.10\ \mathrm{GHz} \cdot \mathrm{mm}$. RF-power was supplied in 2-µs pulses with a repetition rate of 16.8 Hz.

exposure. Once the conditioning process is complete, the final breakdown threshold is consistently within 5% of the CST predictions.

Recall that the data shown in Fig. 4.5 was generated using the magnetron operating with 2-µs pulses and a repetition rate of only 16.8 Hz. This extremely low duty cycle (3.36×10^{-5}) means that the cumulative exposure to multipactor is very low. Over the full 90-min run of this experiment, multipactor only occurs for a total of 181.4 ms. This is in contrast to other experiments where RF is applied in relatively long bursts (CW in Woo [15]; 4-s pulses in Graves [16]). Even other short-pulse experiments operated with much higher duty-cycles (2-µs pulses at 10% duty cycle in Mirmozafari *et al.* [62]). This suggests that during these experiments, the multipactor self-conditioning process will occur relatively rapidly compared to the time-scale of their human observers.

Recall that the SEY data used for the CST PIC simulations presented in Chapter 2 were benchmarked relative to Woo's published experimental data. In his article, Woo noted that he attempted to minimize exposure to multipactor to prevent this conditioning effect [15]. As a result, we may expect our simulations (with SEY data for non-baked copper from Bojko *et al.* [92]) to better correspond to data from before the surfaces undergo conditioning. However, this is likely

not the case because of how rapid the conditioning process is on human time-scales. In Woo's CW, manually operated experiment, the system will reach a fully conditioned state before any measurements could be taken.

Further testing with the Scandinova modulator also found that the full time-scale of the conditioning process appears to scale linearly with the duty cycle. Doubling the repetition rate to 33.6 Hz reduced the run-time from 90 min to 45 min without significantly altering the breakdown threshold. This further supports our conclusion that multipactor self-conditioning is only dependent on the total, cumulative exposure to multipactor and is consistent with computational results from Al Hajj Sleiman *et al.* [77].

4.3 Multipactor Susceptibility Measurements

Aside from general characterizations of the multipactor breakdown, the primary goal of this work is to measure the power thresholds necessary for a discharge to occur. To measure the breakdown threshold, the RF power level is slowly increased while the operator monitors the oscilloscopes displaying the various diagnostic signals. During this process, RF power is pulsed with a repetition rate of 16.8 or 33.6 Hz.[3] Once the diagnostics begin to respond to multipactor, power is then reduced until multipactor is no longer observed. This process is then repeated until the power level is precisely tuned such that multipactor is only barely observable. Once this is achieved, the oscilloscopes are frozen, their signals are recorded, and the RF-power is brought to low levels (100 to 200 W). This overshoot-then-tune method is used to accommodate for the test-cell's extremely low duty cycle and relatively small seed electron source rate. By briefly going to higher power levels, the transmission line can be seeded with residual charged species that can enhance the seed electron population and reduce the wait-time for multipactor.

Since this procedure for measuring the breakdown threshold is based on the operator's live interpretation of the diagnostic signals, it is repeated several times (typically five to ten) to account for variances in the operator's judgment. Final measurements of the breakdown threshold are then reported as an average and standard deviation.

Also note that this procedure for measuring the breakdown threshold does not typically allow the operator to directly record the diagnostic signals that occur during the smallest observed discharge. Instead, subsequent RF pulses are used to represent the power level the operator considers to be the multipactor breakdown threshold. The breakdown threshold is then considered to be an average over the RF pulse. Because the RF signal does not have a well-defined rise-time when we use the Scandinova modulator, our averaging algorithm only includes the highest-power segment of each pulse. This is described further in Appendix A.

[3] Higher repetition rates may be used to compensate for low seed-electron source rates.

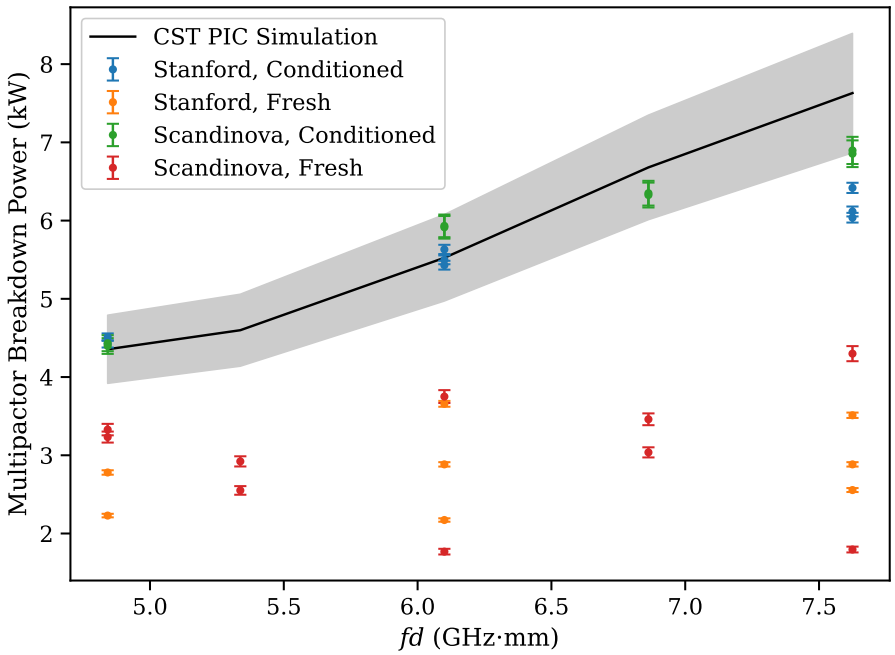

Figure 4.6: Experimentally measured multipactor susceptibility diagram. Data are shown for both "fresh" and fully conditioned surfaces. Experimental data were measured using the Stanford Modulator (originally published in the *Review of Scientific Instruments* [22]) and were later reproduced using the Scandinova modulator. These data are also compared to updated CST Particle Studio simulations (in black), with the shaded region representing 10% agreement.

Figure 4.6 shows an experimentally measured susceptibility diagram for the coaxial multipactor test cell. Two data sets are presented here. The first data set represents our original experiment published in the *Review of Scientific Instruments* [22] and was measured using the Stanford modulator. Each of these data points represent the average of ten consecutive measurements of the breakdown threshold. These data were later reproduced using the Scandinova modulator. All of the experimental data are compared with updated PIC simulations that were performed in CST Particle Studio, with the shaded region representing agreement to within 10%. These updated simulations reflect minor adjustments that were added to the as-built experimental hardware.

The data in Fig. 4.6 highlight the importance of the multipactor self-conditioning effect by comparing "fresh" surfaces (zero conditioning time) to those that had been fully conditioned (after the final conditioning step). Before conditioning, the breakdown threshold is highly inconsistent and could not be reproduced on a day-to-day basis. However, once the transmission line is fully conditioned, the data are both consistently within 10% of the CST simulations and highly repeatable between experimental trials.

CHAPTER 5

Multipactor Suppression

In this chapter, we discuss simulations and experiments for testing techniques for preventing multipactor. In particular, we will focus on how textured surfaces can reduce the secondary electron yield. By inhibiting secondary electron emission, textured surfaces will retard multipactor growth and raise the power limits for safe operation.

5.1 Transmission Line Fabrication

This work will focus on experiments using textured surfaces to prevent multipactor in the University of Michigan coaxial multipactor test cell. Textured and porous surfaces have been shown to be effective tools for preventing multipactor [76, 85–87, 89, 103]. However, their greatest challenge lies in their manufacture. In previous studies, porous surfaces were produced using lithographic etching technologies [86, 87]. These methods are based on etching patterns into a masked substrate. Various etching media can be used, including both conventional chemical methods and more advanced plasma-based technologies. The key lies in how the pattern is applied to the mask that shields the substrate. In photolithographic systems, a UV laser etches the pattern into the mask, exposing the substrate to the etching medium. In a coaxial system, the application of the pattern onto the mask becomes an issue because there is very little space inside the outer conductor. For example, the outer conductor in a 50-Ω, Type-N coaxial connector[1] is less than 1 cm in diameter [104]. Few, if any, high-power etching lasers will fit inside this component. This raises the question: how do we make a textured, coaxial transmission line?

Additive manufacturing processes form parts by fusing materials in layers. As a result, their final surface finish will contain artifacts from this layered construction. Depending on which 3D-printing methodology is used, these components can have extremely high surface roughness. Because of this texture, we can use additive manufacturing as a convenient method for introducing surface texture to transmission line structures.

[1] One of the largest commonly used connectors.

These experiments evaluated the multipactor suppressive effects from using 3D-printed surfaces. We tested coaxial transmission line structures manufactured using two different processes: selective laser melting (SLM) and atomic diffusion additive manufacturing (ADAM). Only the outer conductor was 3D-printed in this experiment. This served two purposes. First, this minimized the number of parts that need to be manufactured; since every fd requires a new inner conductor, it is convenient to pair the original machined parts tested in Chapter 4 with a single printed outer conductor.

Recall in Sec. 2.2.2, our PIC simulations showed that electrons tended to hit the outer conductor at higher energies. This implied that coaxial multipactor is driven primarily by the outer conductor and suggested that alterations to the outer conductor's SEY will have the greater effect on the multipactor susceptibility. This led to the second reason why we only modified the outer conductor: the breakdown threshold will be increased sufficiently to demonstrate proof-of-concept, but will also ensure that the breakdown threshold remains below the upper power limits of the multipactor test cell. Once we have demonstrated that 3D-printed transmission lines are an effective tool for preventing multipactor, future experiments can be performed to evaluate the full potential of this technology.

5.1.1 Selective Laser Melting (SLM)

The first 3D-printing technology we explored is Selective Laser Melting (SLM). The SLM process is a form of powder-based 3D-printing [105, 106]. Like most additive manufacturing processes, parts are produced layer-by-layer. Initially, a layer of fine, metal powder is evenly distributed over the printing bed. A high-power laser fuses the powder along the part's contours. This process is repeated for subsequent layers, with fresh powder being applied after each laser scan. Depending on the print settings, SLM-printed components can have relative densities that are either very high (99.9%) or extremely low (foam-like) [107]. Low-density parts can be extremely porous [108]. The many voids in such a material would efficiently trap secondary electrons, and thus may provide excellent resistance to multipactor. For copper in particular, high density, high purity parts can be produced with electrical properties similar to OFHC copper [108], suggesting minimal losses in signal quality. Additionally, SLM-printed parts can have very high levels of dimensional accuracy, and may need minimal post-processing [105, 106].

Selective laser melting is a powerful tool for producing high resolution parts from a wide range of materials. However, it has a number of significant drawbacks. The most obvious disadvantage is its relatively high cost; SLM 3D-printers are expensive compared to other additive manufacturing technologies, and the cost of the metal powders are several orders of magnitude more expensive than bar stock [106]. These metal powders also have a number of safety considerations. Aside from the respiratory hazard from using fine particulates, metal powders are extremely flammable. The

Figure 5.1: Photograph of the SLM-printed outer conductor segment. The total length of this part is 76.2 mm (3.0 in).

build chamber must be pressurized with inert gas to prevent explosion [106].

We tested the multipactor resistance of an SLM-printed coaxial outer conductor, which is photographed in Fig. 5.1. This part was produced from 15–53-$\mu\mathrm{m}$ copper powder with the following print settings: a laser power of 200 W, a scan speed of 300 $\mathrm{mm\,s^{-1}}$, a hatch distance of 150 $\mu\mathrm{m}$, and a layer thickness of 30 $\mu\mathrm{m}$. A casual inspection of the part's inner surface shows that it has a very significant surface roughness and should provide some protection against multipactor.

After the conclusion of the multipactor experiment, the SLM-printed outer conductor was bisected and imaged by the Michigan Center for Materials Characterization. Two scanning electron microscope (SEM) images of the part's inner surface are shown in Fig. 5.2. In the cross-section view shown in Fig. 5.2a, the surface roughness resembles a mountainous plateau. A second view of the SLM-printed surface is shown in Fig. 5.2b. From this top-down perspective, we see that deep pores are scattered over the surface.

In Sec. 5.2, when we approximate the surface structures so we can modify the SEY curve, we will represent the peaks and valleys in Fig. 5.2a as an infinite array of pyramidal pits. Although this approximation is quite extreme (and ignores the smaller, deeper pores visible in Fig. 5.2b), it will allow us to use a simple and efficient ray-tracing algorithm for predicting the SEY. These pits are characterized by a width w and height h. Based on our SEM images, we will assume that the cavities are approximately 100 $\mu\mathrm{m}$ wide and 50 $\mu\mathrm{m}$ deep.

To verify the material composition of the SLM-printed conductor, the Michigan Center for Materials Characterization also performed an energy-dispersive x-ray spectroscopy (XEDS) analysis. These results are shown in Table 5.1. Note that XEDS is only a surface-level analysis tool; the measured x-ray spectra typically only represent materials less than 100 $\mu\mathrm{m}$ from the surface [109]. To counter this, we have obtained measurements at two locations: a) the surface where multipactor

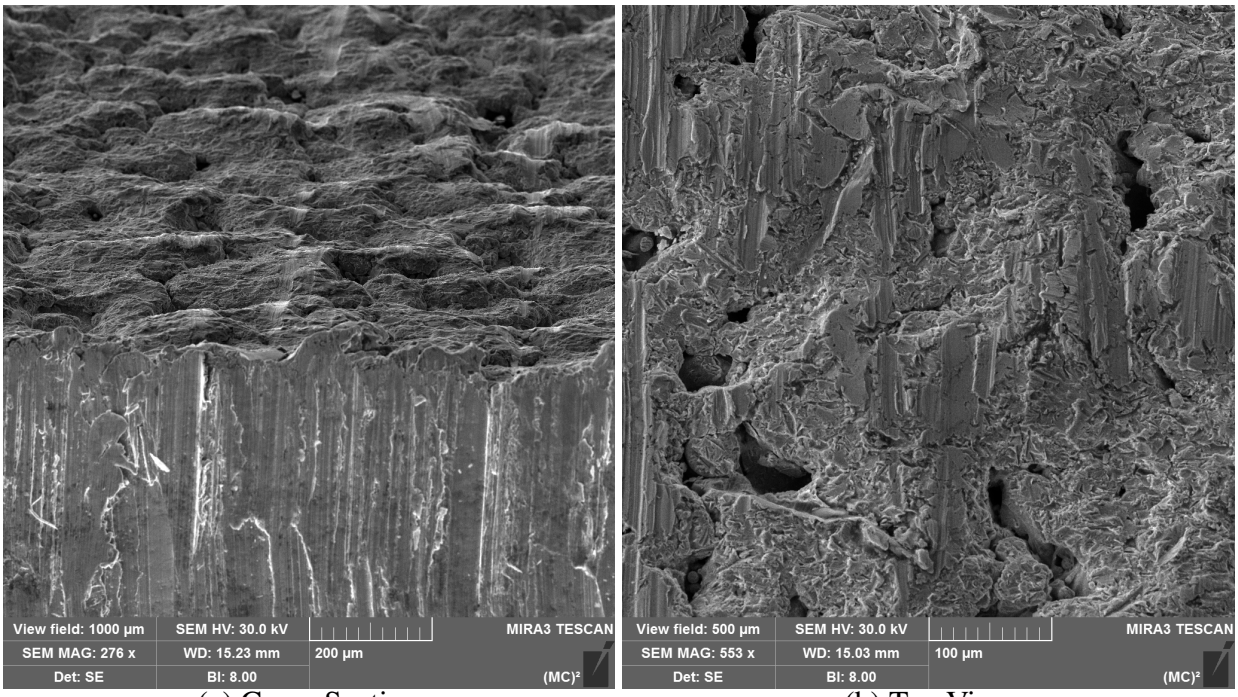

(a) Cross-Section (b) Top View

Figure 5.2: SEM micrographs highlighting the surface texture of the SLM-printed outer-conductor. Images are from the Michigan Center for Materials Characterization.

TABLE 5.1
MATERIAL COMPOSITION OF THE SLM-PRINTED CONDUCTOR

	MP Region		Cross-Section	
Element	**Weight %**	**Atom %**	**Weight %**	**Atom %**
Cu	85.22	63.22	92.55	84.69
O	9.25	27.24		
Al	3.61	6.31	4.49	9.67
Si	1.92	3.23	2.49	5.15
Fe			0.48	0.49

will occur and b) at the cross-section where the sample was cut in half. The data from the cross-section provide a better representation of the 3D-printed part's bulk material composition.

The SLM-printed conductor is principally made up of copper with some aluminum, silicon, and iron impurities. Inside the multipactor region, we see a very large oxygen concentration; this indicates the presence of a thick oxide layer. This oxide layer is likely substantially reduced during multipactor self-conditioning. Oxygen was not observed in the cross-sectional measurement, which implies minimal oxidation within the bulk structure of the conductor, likely because they were fabricated in an inert atmosphere.

5.1.2 Atomic Diffusion Additive Manufacturing (ADAM)

Atomic diffusion additive manufacturing (ADAM) is an alternative method for 3D-printing metallic structures. This newer 3D-printing concept has been recently developed by Markforged Inc. [110]. A similar process, trademarked as Bound Metal Deposition, has been patented by Desktop Metal Inc. The ADAM process is based on conventional fused deposition modeling (FDM) 3D-printers. In FDM, parts are formed by fusing layers of extruded plastic filament. This relatively inexpensive process is the technology driving the majority of consumer-grade desktop 3D-printers. Instead of a plastic filament, ADAM uses a metal wire coated in a polymer sheath; this plastic coating acts as an adhesive binder while the part is printed. After the initial printing, the "green" part is fired in a sintering oven and the binding agent is pyrolized away. Once this process is complete, only the final, metal structure will remain.

We evaluated the multipactor resistance of an ADAM-printed coaxial outer conductor. Since ADAM-printed parts are produced using an extruded filament, their surface finish is dominated by the layer-line structures. These large grooves can potentially provide significant resistance to multipactor [85, 103]. Due to size constraints of the sintering oven used by our third-party printing vendor, the multipacting segment of the coaxial transmission line needed to be shortened. To ensure multipactor does not occur between the smooth, machined surfaces, the inner conductor was also shortened such that its central multipacting region only overlaps the ADAM-printed outer conductor segment.

The ADAM-printed outer conductor was manufactured using a Markforged MetalX printer with a post-sintered layer-height of 129 μm. A photograph of our ADAM-printed outer conductor is shown in Fig. 5.3. In this image, we can clearly see the banded structure that was formed from by the filament-based printing process.

After the conclusion of the multipactor experiments, the ADAM-printed conductor was bisected and imaged by the Michigan Center for Materials Characterization. Two SEM micrographs of the ADAM-printed surface structure are shown in Fig. 5.4. The cross-sectional view in Fig. 5.4a shows

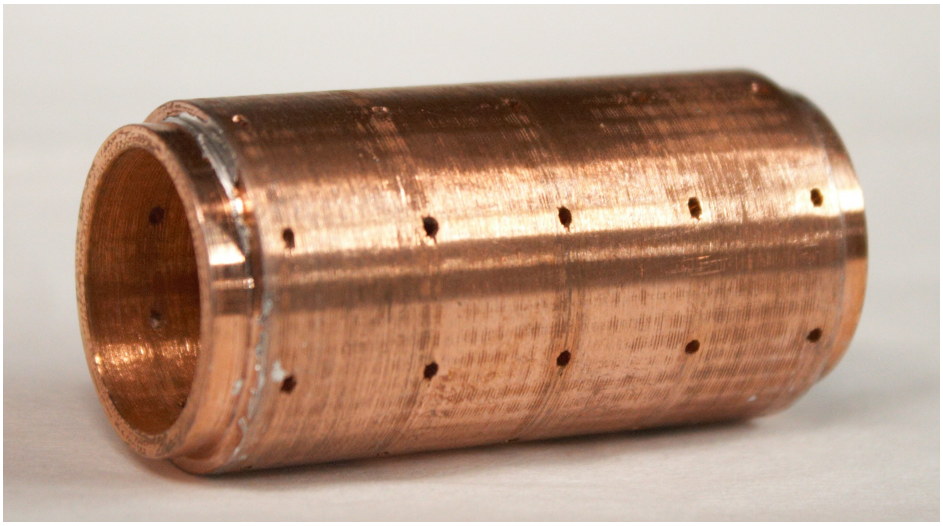

Figure 5.3: Photograph of the ADAM-printed outer conductor segment. The total length of this part is 50.8 mm (2.0 in).

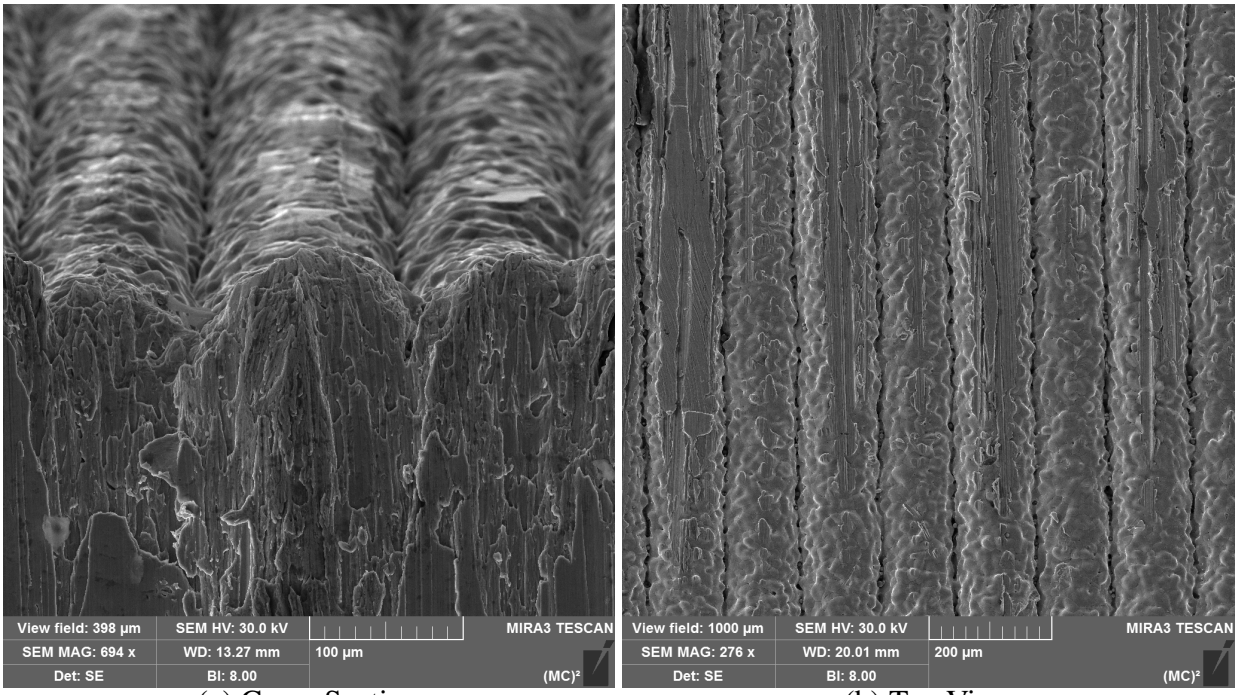

(a) Cross-Section (b) Top View

Figure 5.4: SEM micrographs highlighting the surface texture of the ADAM-printed outer-conductor. Images are from the Michigan Center for Materials Characterization.

that the surface structures are dominated by the fused cylindrical filament, resulting in an array of long trenches. At macroscopic scales, similar grooved structures have been previously shown to significantly reduce secondary electron emission [103] and increase the multipactor breakdown threshold [85].

TABLE 5.2
MATERIAL COMPOSITION OF THE ADAM-PRINTED CONDUCTOR

	MP Region		Cross-Section	
Element	**Weight %**	**Atom %**	**Weight %**	**Atom %**
Cu	86.64	66.14	100	100
O	8.07	24.47		
Al	3.64	6.54		
Si	1.65	2.86		

Once again, an XEDS analysis was performed to confirm the material composition of the 3D-printed outer conductor. On the surfaces near the multipacting region, we see a significant oxide layer and some minor aluminum and silicon impurities. However, at the cross-section where the part was cut in half, we only observed the characteristic x-rays for copper. This suggests that the bulk material has virtually no impurities; this confirms Markforged's claim of copper concentrations greater than 99.8% [111].

5.2 Modeling Surface Effects

Textured surfaces reduce the secondary emission yield by trapping electrons inside surface protrusions. As we discussed in Chapter 1, secondary electrons may be reflected within surface cavities several times before they diffuse into the bulk vacuum. Since secondary electrons are generally emitted with low kinetic energies, very few true secondaries will be emitted from these successive impacts. As a result, the effective SEY of the material can be significantly reduced. We will simulate this modification to the SEY curve by using a Monte-Carlo, ray-tracing algorithm similar to those used in previous studies [86]. The multipactor susceptibility can then be predicted by using these modified SEY curves in PIC simulations.

When calculating the texture-modified SEY curve, we must choose an emission model for the nominal, smooth surfaces. Although other SEY models that include backscattering and rediffusion will better represent the low-energy impacts between the cavity surfaces, we use the non-baked, tabulated data from Bojko *et al.* [92], as it gave the best agreement with Woo's data [15] in Fig. 2.5. This also ensures our subsequent PIC simulations are comparable to our prior work.

5.2.1 Monte-Carlo SEY Generation

The textured SEY is calculated using a Monte-Carlo algorithm based on work by Ye *et al.* [86]. We begin with several simplifications. First, we assume that these processes occur instantaneously; the lifetime of the secondary electrons trapped within the surface structures is much shorter than an RF-period. We also assume that the electrons are not influenced by electromagnetic fields (either from the applied RF or from space-charge effects) when they are near the transmission line surfaces. Finally, we use a simplified representation of the surface structures. The curvature of the coaxial transmission line is neglected, and the micro-scale surface structures are modeled as infinite arrays of geometrically-simple cavities.

Consider a single, three-dimensional cavity with an opening at its top surface, parallel to the xy-plane. An electron traveling with some energy E enters the cavity at point $\mathbf{r_0}$. The electron approaches the cavity at a polar angle θ relative to the z-axis. We do not assume the cavity is axisymmetric, so the electron is also traveling with some azimuthal angle ϕ about z. After the electron enters the cavity, it impacts a surface.

A ray-tracing algorithm (described in Sec. 5.2.2) locates the point of impact and identifies the surface. An SEY model[2] is then applied to determine the number of secondary electrons, δ, that are emitted based on the primary's energy and angle-of-impact (relative to the impact surface). Since the SEY is rarely an integer, we do not consider discrete secondary electrons; instead, we increase the primary electron's "weight" (initially, $w = 1$) by a factor of δ. The weighted secondary electron is then emitted from the surface with some new energy and direction; secondary electrons are emitted with Maxwellian energy, cosine-distributed polar angle, and uniform azimuthal angle. This procedure is iterated until the electron leaves the cavity and returns to the bulk vacuum. The weight of the escaped particle is the SEY of the textured surface.

Of course, a single seed electron is a poor statistical sample, so we instead consider several thousand particles distributed evenly in a sheet at the top surface of the cavity. The effective SEY of the textured surface is then

$$\delta_{eff} = \frac{1}{N} \sum_{i}^{N} w_i, \tag{5.1}$$

where w_i is the final weight of each electron, and N is the number of seed electrons.

[2]Any SEY model can be used; however, since the secondary electrons generally have low energies, it is best to use a model that considers the rediffusion and backscattering of low-energy primary electrons. Such models include the modified Vaughan model [26, 28] (which assumes constant SEY below some cutoff energy) or the Furman model [31] which uses a robust statistical model for backscattered and rediffused electrons.

5.2.2 Ray-Tracing Model

Our model uses a vector-based ray-tracing algorithm for quickly solving for the electron trajectories between the cavity surfaces. Consider the simplified case illustrated in Fig. 5.5 with an electron impacting a plane at angle α relative to the normal vector $\hat{\mathbf{n}}$. The set of points $\mathbf{p}$ will lie on this plane if

$$(\mathbf{p} - \mathbf{p}_0) \cdot \hat{\mathbf{n}} = 0 \tag{5.2}$$

where $\mathbf{p}_0$ is a known point on said plane. Since we assume that the electron is not accelerated, the set of points along its trajectory is expressed by the linear vector equation

$$\mathbf{r} = \mathbf{r}_0 + \hat{\mathbf{v}}s \tag{5.3}$$

where $\mathbf{r}_0$ is a known point along the trajectory (we will use the electron's origin), $\hat{\mathbf{v}}$ is the velocity unit vector, and s is a length scale. To find the point where the electron impacts the surface, we set $\mathbf{p} = \mathbf{r}$ and substitute (5.3) into (5.2). We then solve for s at the point where the electron impacts the surface:

$$s = \frac{(\mathbf{p}_0 - \mathbf{r}_0) \cdot \hat{\mathbf{n}}}{\hat{\mathbf{v}} \cdot \hat{\mathbf{n}}}. \tag{5.4}$$

With s, (5.3) evaluates to the point of impact.

So far, this algorithm has only considered a system with a single, infinite surface. When considering more than one surface, this ray-tracing method may indicate more than one point of impact. This occurs when an electron impacts outside the bounded domain of the surface cavity. We must now filter these impacts to only include those that occur within the finite cavity faces.

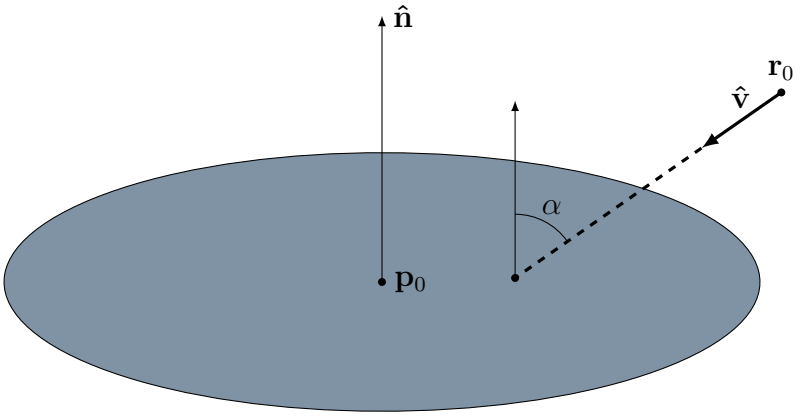

Figure 5.5: Illustration of the vector analysis used to determine the point-of-impact of an electron against a single plane.

For the SLM-printed metals, we will assume that the pyramidal cavities have triangular faces[3]. Consider the case where an electron's trajectory intersects a plane (with surface normal $\hat{\mathbf{n}}$) at point P. The cavity's face is the triangle ABC whose edges are the vectors $AB = B - A$, $BC = C - B$, are $CA = A - C$. Now, let us define the vectors $AP = P - A$, $BP = P - B$, and $CP = P - C$. Since all of these points are on the same plane, the cross-products $AB \times AP$, $BC \times BP$, and $CA \times CP$ will have a single component in the $\hat{\mathbf{n}}$-direction. If the point of impact, P, lies within ABC, then the $\hat{\mathbf{n}}$-component of all three cross-products will have the same sign.

In a trench structure[4] similar to the one we will use for the ADAM-printed metals, the cavity's surfaces are a pair of infinitely long rectangular faces intersecting along the x-axis. Valid points of impact will only occur between the xy-plane and the top of the trench.

5.2.3 SEY Modified by SLM-Printed Surfaces

At the microscopic scale, the surface of the SLM-printed outer conductor resembles a mountainous plateau with numerous peaks and valleys. We will represent this as an infinite array of three-dimensional pyramidal pits, each with width w and depth h. An example of one of these pits is

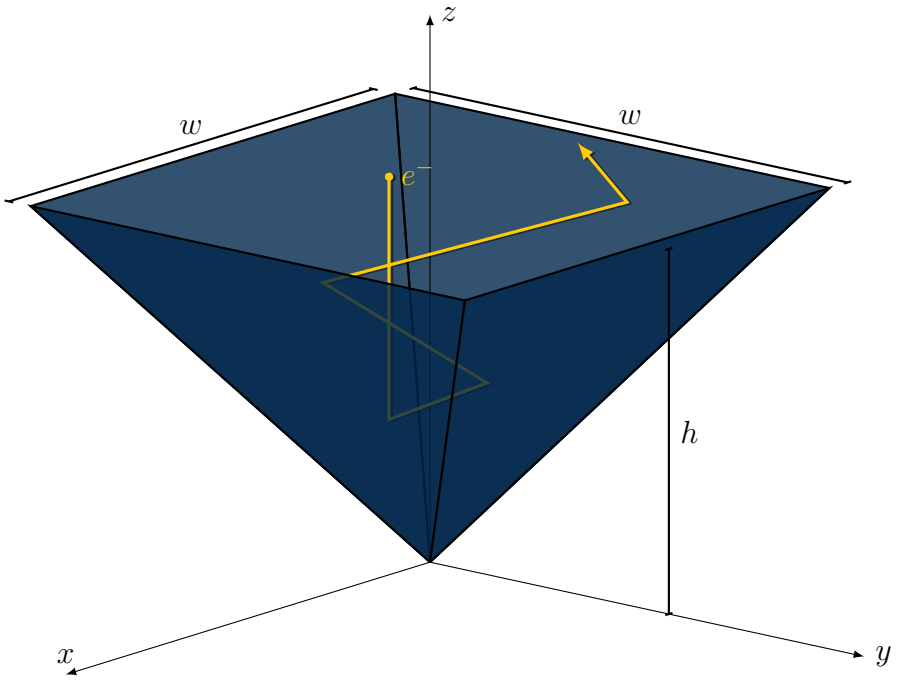

Figure 5.6: Illustration of the pyramidal cavity structure representing the micro-scale surface structures of the SLM-printed metals.

[3]This structure will be discussed in detail in Sec. 5.2.3.
[4]This structure will be discussed in detail in Sec. 5.2.4.

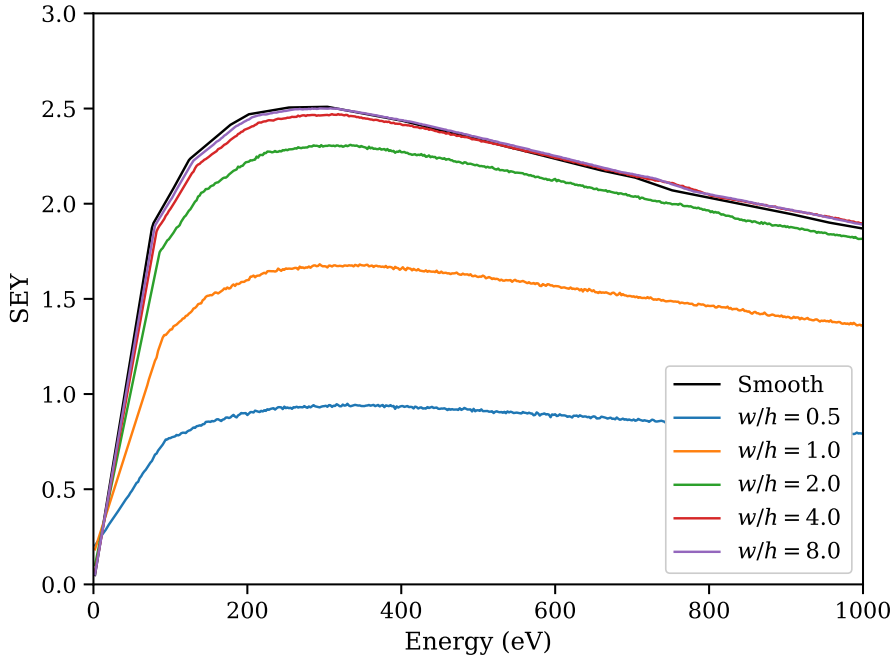

Figure 5.7: Secondary electron yield for electrons impacting normal to the SLM-printed surfaces. Data are shown for several aspect ratios for the depth and width of the pyramidal structures and are compared to the nominal smooth surface. To generate these data, the cavity depth was chosen arbitrarily as $h = 50\ \mu\mathrm{m}$.

shown in Fig. 5.6. This model is a simplification of bowl-structures used by Kawata *et al.* [112]. Since all motion is perfectly linear, only the aspect ratio, w/h, is important.

The textured SEY curves for these pyramidal cavities are shown in Fig. 5.7. Each data point in these curves was generated by using 10^5 electrons impacting normal to the bulk surface, and data are shown for cavities with several aspects ratios. Secondary electrons are also assumed to be emitted with Maxwellian-distributed energies with a temperature of 7.5 eV; this matches the emission energy distribution used in our prior CST Particle Studio simulations.

In general, secondary electron emission is suppressed by the surface structures. This is particularly the case when the pits are deeper than they are wide ($h > w$); when $h = w$, the peak SEY is reduced by 40%. Lowering the aspect ratio, w/h, further causes the SEY to be universally below unity; since impacting electrons are not fully replaced, multipactor will be impossible. The high trapping efficiency for such a structure is illustrated in Fig. 5.8 which shows a cross-section of a cavity where $w/h = 0.5$. Let us consider an "average" case where an initial seed electron penetrates halfway into the cavity's depth. Secondary electrons will be emitted with a cosine-distributed polar angle, α, relative to the surface. Half of the secondary electrons will be emitted with $\alpha \leq 30°$; this is represented by the shaded region. If we ignore backscattering effects, then these low-energy

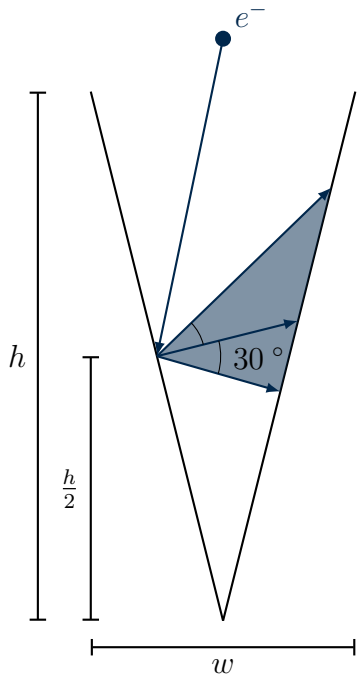

Figure 5.8: Illustration demonstrating the efficient electron trapping mechanism when $w/h = 0.5$.

secondaries will be reabsorbed. From this diagram, it is clear that the majority of electrons will undergo multiple impacts before leaving the cavity, drastically reducing the SEY. This proves that these types of structures can be extremely effective for preventing multipactor. As one would expect, extremely wide cavities ($w >> h$) negligibly affect the SEY and asymptotically approach the original SEY curve.

When electrons impact a surface at an angle, the SEY is typically enhanced because electrons will "skim" along the surfaces [113]. Since they will not penetrate as deeply into the surfaces, more electrons will be emitted back into the vacuum. Let us now examine this effect, which is shown in Fig. 5.9. Although we will be unable to use the angular-dependent SEY curve in our CST PIC simulations, we are including it here to demonstrate some interesting consequences from using the textured surfaces. Since the pyramidal cavities are not axi-symmetric about the z-axis, these data are averaged over all azimuthal angles. These data are also compared with a scaling law based on the Vaughan model [26]. This scaling law, which is used by CST Particle Studio for tabulated SEY data [91], considers the electrons to impact with an effective energy

$$E_{eff} = (E_0 - E_{threshold}) \frac{2\pi}{2\pi + \theta^2} + E_{threshold}, \tag{5.5}$$

where E_0 is the true impact energy, θ is the impact angle (expressed in radians) relative to the

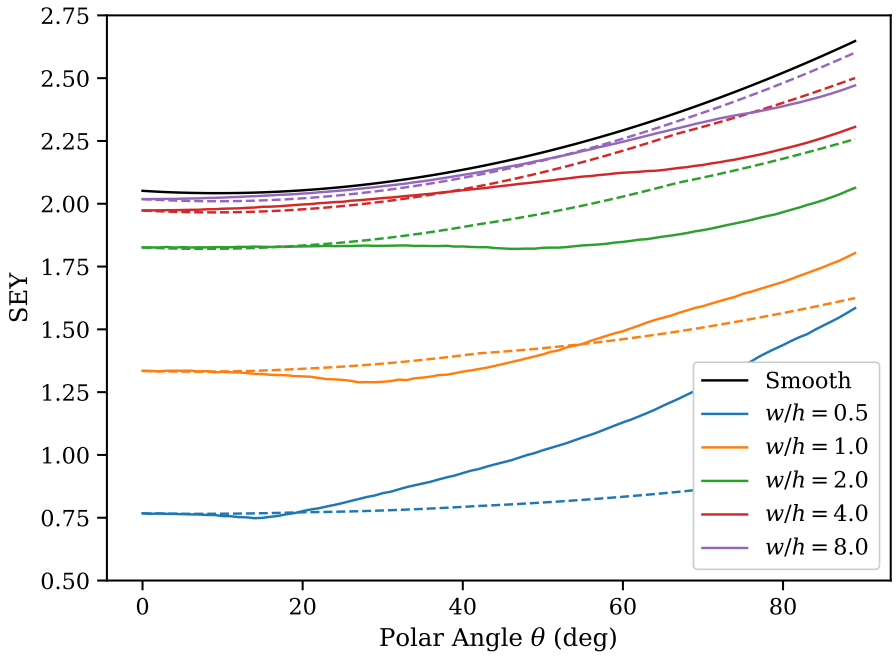

Figure 5.9: Calculated SEY (solid lines) of SLM-printed surfaces as a function of incidence angle relative to the surface normal. Dashed lines are calculated by modifying the non-angular data using a scaling law based on the Vaughan model [26, 91]. These data are for 100-eV electrons and are averaged over all azimuthal incidence angles.

surface normal, and $E_{threshold}$ is an energy threshold such that $\delta(E_0 \leq E_{threshold}) = 0$. The angular-dependent SEY is then

$$\delta(E_0, \theta) = \delta(E_{eff}, 0)\left(1 + \frac{\theta^2}{2\pi}\right). \tag{5.6}$$

Although the textured SEY data follows the scaling law at low polar angles, the two models quickly diverge. For now, let us examine the case where $w = h$; the same behavior is observed regardless of the aspect ratio, but is most visible for this case. When electrons impact the surface at a low polar angle, secondary electron emission is reduced. Initially, increasing the polar angle will reduce the SEY—this is a direct contradiction to the scaling law used in Vaughan's model. Further increases in the polar angle will eventually reach a critical point where the SEY will begin increasing. For very deep cavities (low aspect ratios), the SEY will eventually surpass the scaling law; at high polar angles, secondary electron emission will be enhanced by the surface texture. This enhancement occurs because of a combination of two effects: electrons impact the cavities' walls at highly oblique angles and release more secondary electrons, and they are unable to penetrate the

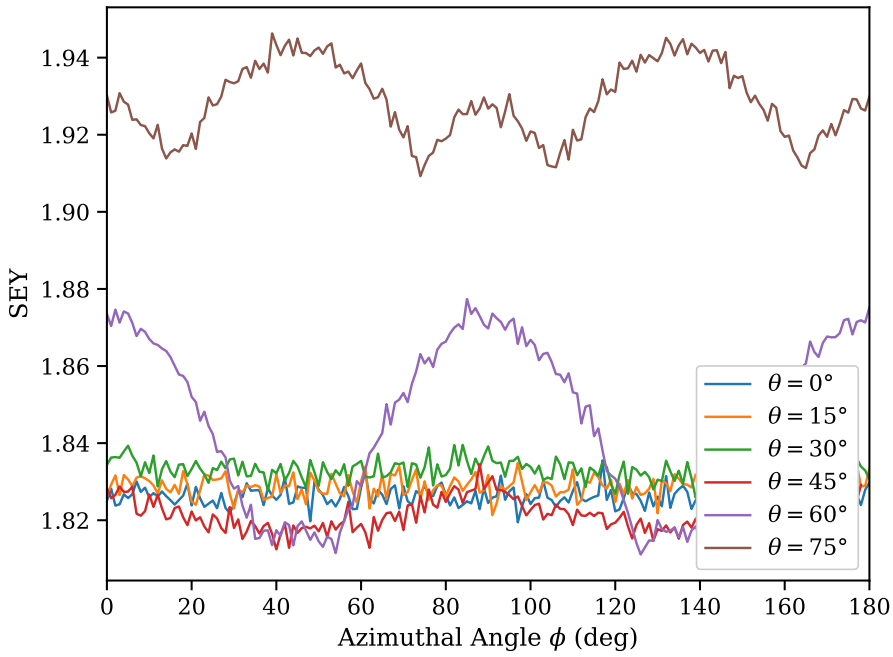

Figure 5.10: Secondary electron yield of the SLM-printed surface as a function of the incident azimuthal angle. Data are shown for 100 eV electrons impacting a pyramidal cavity with $w = 100$ mm and $h = 50$ mm.

cavities' full depths, allowing more electrons to escape from the surface.

So far, all of the SEY curves we have discussed have been averaged over all azimuthal angles. Although this is a reasonable approximation of the random distribution of the SLM-printed surface structures we saw in Fig. 5.2, for completeness, let us now examine the azimuthal dependence. These data, which are for 100-eV electrons impacting a surface with $w = 100$ mm and $h = 50$ mm ($w/h = 2$), are shown in Fig. 5.10. Several curves are shown, corresponding to a range of polar impact angles. In general, the SLM-printed surfaces' azimuthal dependence is relatively mild. At its greatest, the SEY only varies by ~3%. As a result, we do not expect the actual orientation of the pyramidal cavities to be very important. Also, note that the SEY is periodic in 90° increments due to the pyramids' square bases.

5.2.4 SEY Modified by ADAM-Printed Surfaces

Atomic diffusion additive manufacturing is a form of FDM 3D-printing. As a result, the surface texture of ADAM-printed parts is dominated by the strata that forms when successive layers of extruded filament are fused together. In our SEM images, we saw this as long trenches formed between the layers' circular profiles. In our Monte-Carlo ray-tracing model, we represent this as an

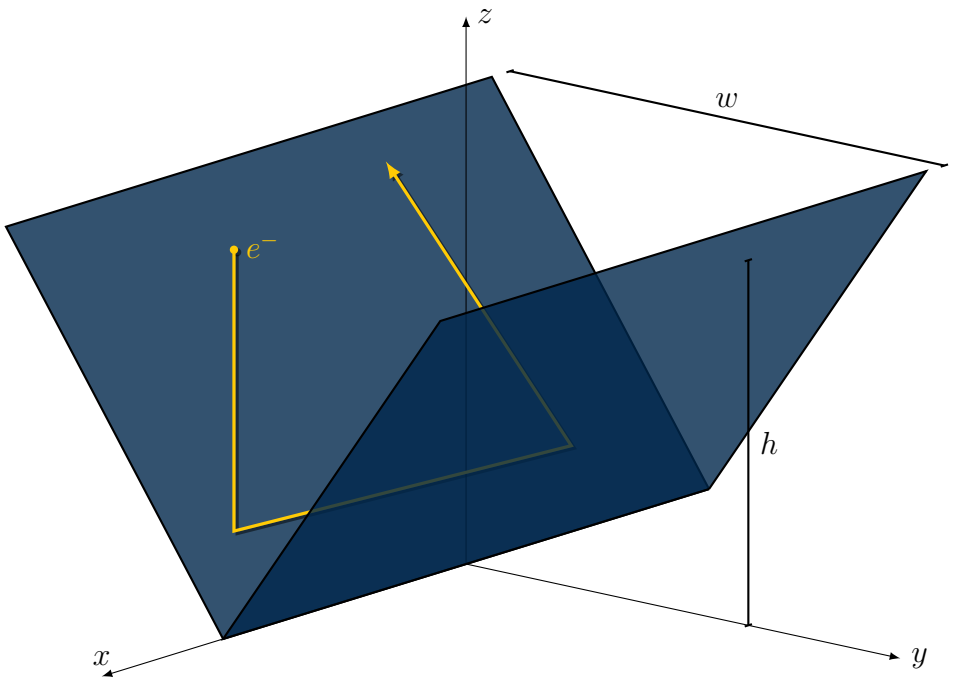

Figure 5.11: Illustration of the triangular trench structure representing the micro-scale surface structures of the ADAM-printed metals.

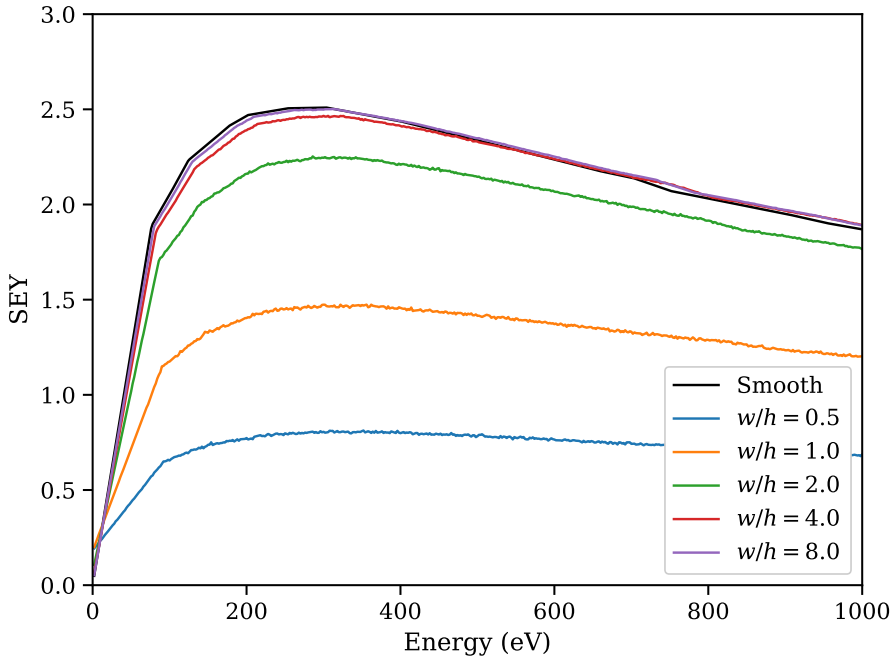

Figure 5.12: Secondary electron yield for electrons impacting normal to the ADAM-printed surfaces. Data are shown for several aspect ratios for the depth and width of the triangular structures. For comparison, data for smooth surfaces are shown in black.

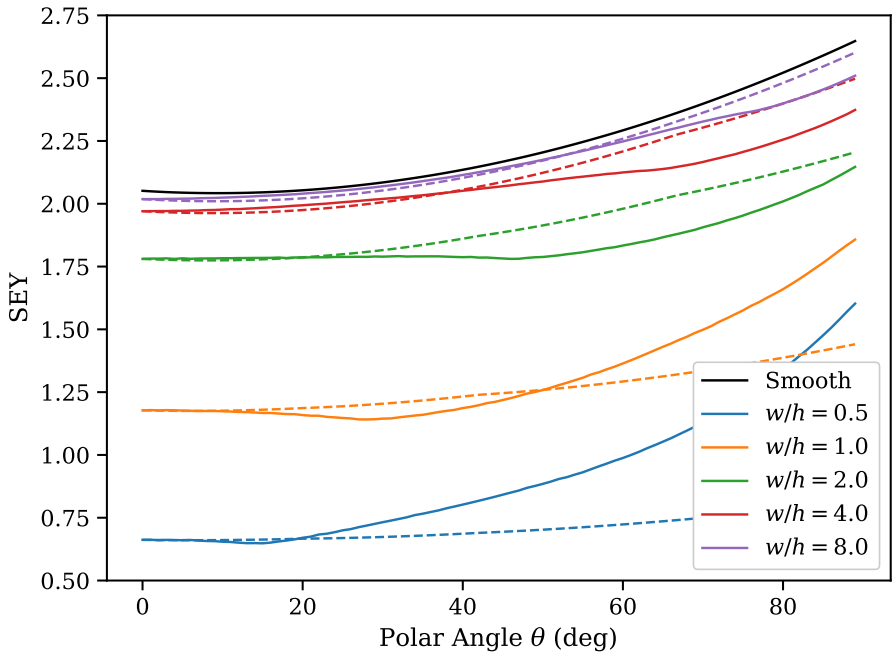

Figure 5.13: Calculated SEY (solid lines) of ADAM-printed surfaces as a function of incidence angle relative to the surface normal. Dashed lines are calculated by modifying the non-angular data using a scaling law based on the Vaughan model [26, 91]. These data are for 100-eV electrons and are averaged over all azimuthal incidence angles.

infinitely long triangular trench, as illustrated in Fig. 5.11. These trenches have some width w and height h. Since all electron paths are perfectly linear, the absolute length-scale of these trenches are unimportant, and the SEY is only affected by the ratio of the width relative to the height.

The SEY curves for electrons impacting the trenches normal to the bulk surface are shown in Fig. 5.12. These results are very similar to the data from the pyramidal cavities used to describe the SLM-printed materials. At high aspect ratios, the SEY is nearly identical to the SLM model. However, low-aspect-ratio trenches do appear to be somewhat more effective at suppressing secondary electron emission. This trend is continued when we examine the SEY as a function of polar impact angle, as shown in Fig. 5.13.

So far, the SEY modified by the ADAM-printed surfaces is not significantly different from the SLM data. However, these similarities end when we examine the SEY as a function of the incident azimuthal angle ϕ. Figure 5.14 shows the azimuthally-dependent SEY curves for 100 eV electrons impacting both narrow ($w/h = 1$, in (**a**)) and wide ($w/h = 2$, in (**b**)) triangular trench structures. The azimuthal angle, ϕ, is measured relative to the x-axis in Fig. 5.11, and data are shown for several polar impact angles θ.

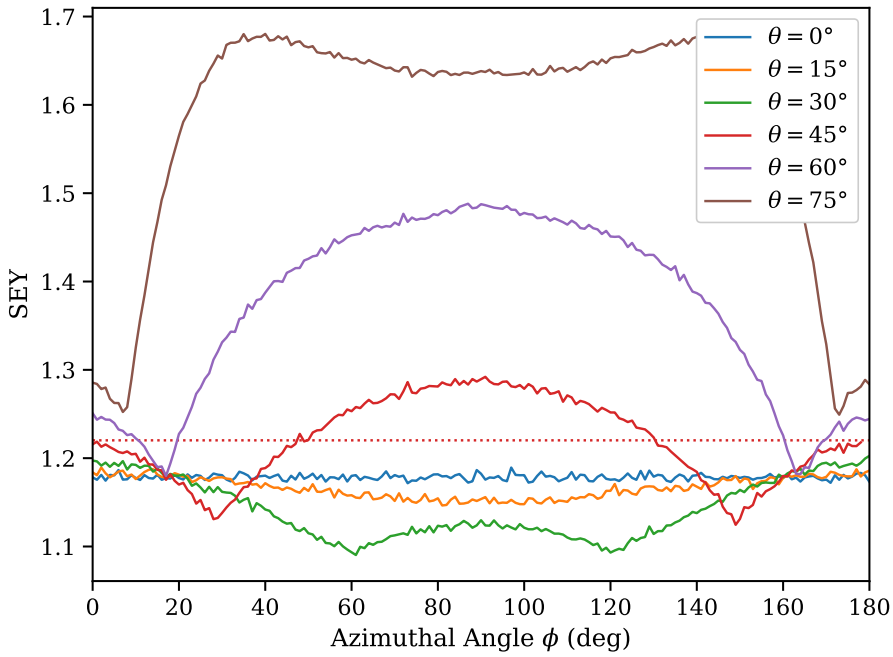

(a) Narrow trench, $w/h = 1$

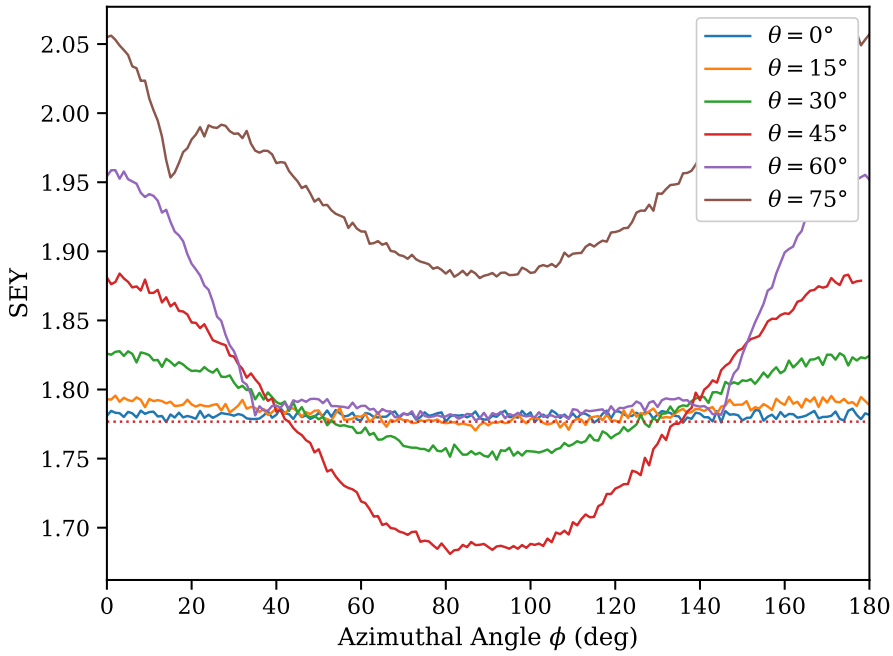

(b) Wide trench, $w/h = 2$

Figure 5.14: SEY of ADAM-printed surfaces as a function of azimuthal angle about the z-axis. Data are shown for 100 eV electrons impacting either a narrow ($w/h = 1$, in (**a**)) or wide ($w/h = 2$, in (**b**)) triangular trench structure with width $w = 100$ µm. Data are shown for several polar angles, θ, relative to the global z-axis. Azimuthal angles, ϕ, of 0° and 180° represent electrons traveling parallel to the trench.

The first feature we note from Fig. 5.14 is that the azimuthal dependence is periodic on a 180° interval and is greatest when the polar angle is large (the electrons are nearly parallel to the bulk surface). The SEY's azimuthal behavior changes depending on whether we are examining a narrow or wide trench. For both cases, the effects are enhanced at high polar angles; these represent glancing hits against the surface. In Fig. 5.14a, the SEY is greatest when electrons are traveling perpendicular to the narrow trench ($\phi = 90°$). Since the path-length between consecutive trenches is relatively small, the electrons cannot penetrate very deeply before striking the surface structures. This reduces the probability for subsequent impacts, preventing electron absorption and enhancing the SEY. Conversely, when electrons are traveling parallel to the trenches ($\phi = 0°$), they will penetrate more deeply, suppressing secondary emission. Because the trenches are infinite in length, this will result in a much higher azimuthal dependence when compared to the SLM-printed surfaces.

Interestingly, the azimuthal dependence reverses for wider trenches, as seen in Fig. 5.14b. When an electron is traveling parallel to the trench, its polar angle is higher relative to the structure's wall than to the global surface normal. This means that the primary electron-impact will *enhance* secondary emission. In a narrow trench, this is overshadowed by the electron-trapping effect. In a wider trench, however, the trapping is sufficiently inhibited that the overall SEY will be enhanced. Note that, regardless of the aspect ratio, the SEY will always be lower than the original, smooth surfaces.

By inspecting our SEM micrographs, we can infer that $w = 125\ \mu\text{m}$ and $h = 50\ \mu\text{m}$ ($w/h = 2.5$). According to Fig. 5.12, the reduction in SEY from the textured surface is relatively minor. In Sec. 5.3.2, we will see that the ADAM-printed surfaces still significantly reduce multipactor. As a result, we must assume that our current model is incomplete. This is likely due to our assumption that we can model the grooved structures as triangular trenches. However, as we saw in Fig. 5.4, the triangular profile does not represent the real groove structure.

Instead of a triangular trench, let us now consider a "seagull" profile structure, which is illustrated in Fig 5.15. We now assume that the trenches are formed from the intersection of two elliptical[5] cylinders; this more closely resembles the profile formed from the fusion of filament layers. Let us now compare with our previous triangular trench model, which is indicated by the dashed lines. At any position along the z-axis, the width across the seagull model is significantly narrower. This will enhance the electron trapping and further reduce the SEY.

The ray tracing model we presented in Sec. 5.2.2 only considers perfectly flat surfaces. Instead of adopting an entirely new computational model, we will approximate the seagull profile as a superposition of two triangular trenches: an average-width trench (with w_{avg} and h_{avg}) and the original trench (with w and h). The width, w_{avg}, is the average separation between the two elliptical arcs in the seagull profile; h_{avg} is the corresponding height that intersects the profile. The effective

[5]We do not assume that the 3D-printer filament retains its circular cross-section.

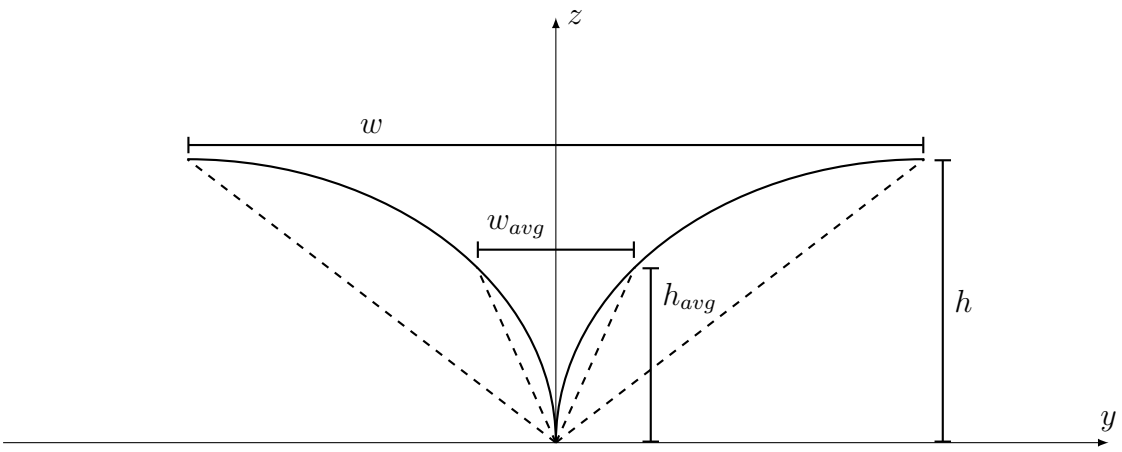

Figure 5.15: Basic illustration of the "seagull" profile that more accurately represents the ADAM-printed surfaces.

SEY is obtained by combining these two trenches:

$$\delta_{eff} = \delta_{w,h}\left(1 - \frac{w_{avg}}{w}\right) + \delta_{w_{avg},h_{avg}}\frac{w_{avg}}{w} \tag{5.7}$$

where $\delta_{w_{avg},h_{avg}}$ is the SEY of the average-width trench.

To find w_{avg} and h_{avg}, we begin by considering that the groove is symmetric about the xz-plane and its walls are 90° elliptical arcs with equations

$$\frac{z^2}{h^2} + \frac{\left(y \pm \frac{w}{2}\right)^2}{\left(\frac{w}{2}\right)^2} = 1 \tag{5.8}$$

with the sign in the second term dependent on whether they lie on positive or negative side of the y-axis. Since the groove profile is symmetric about the xz-plane, let us only consider the arc with $y \geq 0$ and solve (5.8) for $y(z)$:

$$y(z) = \frac{w}{2}\left[1 - \sqrt{1 - \frac{z^2}{h^2}}\right]. \tag{5.9}$$

The average width can now be expressed as $w_{avg} = 2\bar{y}$ where $\bar{y}$ is the average value of $y(z)$. By applying the mean value theorem, we can evaluate $\bar{y}$ as

$$\bar{y} = \frac{1}{h}\int_0^h y(z)dz = \frac{1}{h}\int_0^h \frac{w}{2}\left[1 - \sqrt{1 - \frac{z^2}{h^2}}\right]dz = \frac{w}{8}(4 - \pi), \tag{5.10}$$

and solve for our average width:

$$w_{avg} = \frac{w}{4}(4 - \pi). \tag{5.11}$$

To obtain h_{avg}, we first solve (5.8) for $z(y)$:

$$z(y) = h\sqrt{1 - \frac{\left(y - \frac{w}{2}\right)^2}{\left(\frac{w}{2}\right)^2}}. \tag{5.12}$$

After evaluating at $y = \bar{y}$ and simplifying, we obtain the average height

$$h_{avg} = h\sqrt{1 - \frac{\pi^2}{16}}. \tag{5.13}$$

Recall that our ADAM-printed outer conductor has width $w = 125$ µm and height $h = 50$ µm ($w/h = 2.5$); this corresponds to $w_{avg} = 26.8$ µm and $h_{avg} = 30.9$ µm ($w_{avg}/h_{avg} = 0.87$). We can now use these data to generate a new set of SEY curves, which are shown in Fig. 5.16. Four sets of SEY data are shown here. First is the nominal, smooth data. Next are the SEY curves for both the original triangular trench model and the average-width trench. Although the SEY was

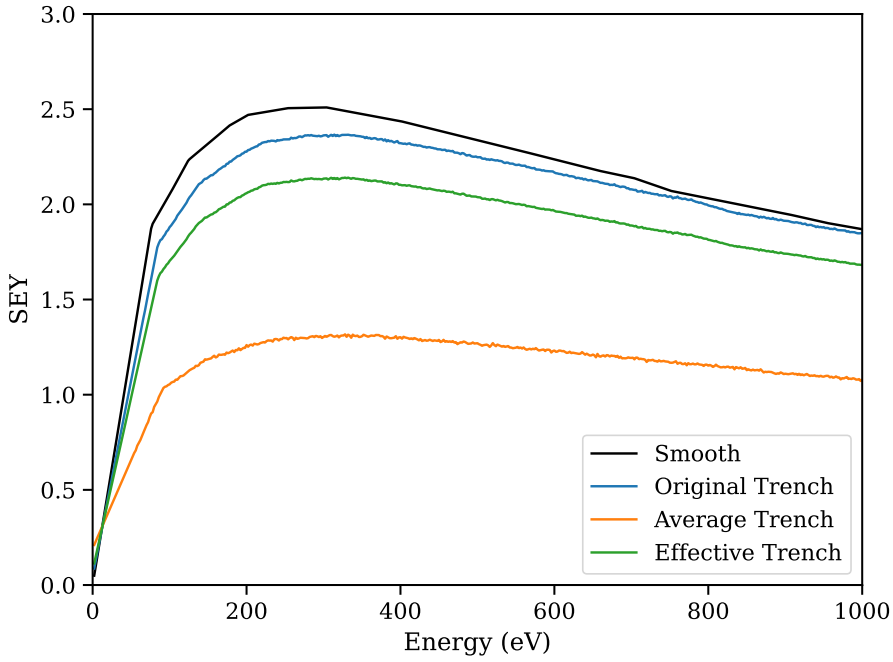

Figure 5.16: Secondary electron yield for electrons impacting normal to the ADAM-printed surface as approximated using the effective trench model. For comparison, data are also shown for smooth surfaces as well both the original and averaged trenches.

minimally affected by the original model, the average-width trench severely reduced secondary electron emission. After combining these data, we can now present the effective SEY curve for the ADAM-printed surfaces. Although the ADAM-printed surfaces only reduce the maximum SEY by 14.7%, our PIC simulations will show that this will result in significantly altering the multipactor properties of our transmission line.

5.2.5 Susceptibility PIC Simulations

Now that we have SEY curves that represent the textured surfaces of the 3D-printed outer conductors, we can run CST Particle Studio simulations to predict when multipactor will occur. These simulations follow the procedure we outlined in Chapter 2. Once again, we consider the entire stepped coaxial transmission line, but now use a segmented outer conductor to account for the 3D-printed region. For the SLM-printed outer conductor, we use the transmission line pictured in Fig. 5.17; a similar model with a shorter 3D-printed segment is used for simulating the ADAM-printed configuration. The dimensions shown in Fig. 5.17 represent the case with an SLM-printed outer conductor and $d = 2.00$ mm; the dimensions for all of the simulated configurations match the as-built hardware that are detailed in Appendix C.

As we discussed before, CST Particle Studio only allows for the direct import of SEY data for electrons impacting normal to the surface. Instead, it will use the scaling law based on the Vaughan model. Although we have shown that the textured surfaces have a significant effect on the angular-dependent SEY, this approximation allows us to generate rough predictions on how the 3D-printed surfaces will affect multipactor. The SEY data that are used for these PIC simulations are

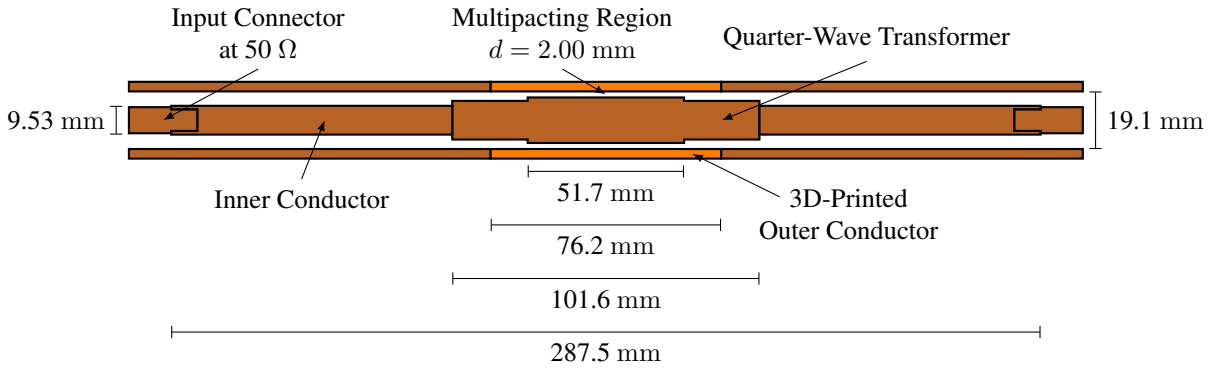

Figure 5.17: Illustration of the stepped coaxial transmission line used for PIC simulations of the 3D-printed transmission line. Dimensions are shown for the case with the SLM-printed outer conductor where $d = 2.00$ mm. Simulations for all other configurations were performed using dimensions matching the as-built hardware, which are detailed in Appendix C.

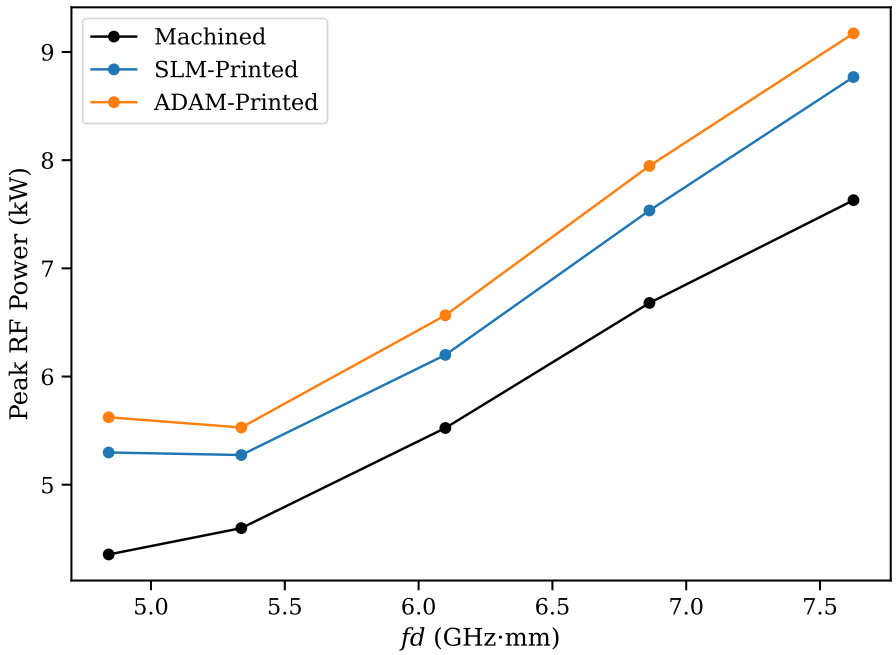

Figure 5.18: Simulated susceptibility diagram for coaxial multipactor with a 3D-printed, textured outer conductor. Data are shown for both the SLM and ADAM-printed structures and are compared to simulations for smooth surfaces [68].

generated for 500 values for the initial electron energy (ranging from 0 to 1000 eV); for each data point, the Monte-Carlo algorithm is seeded with 10^5 initial electrons that are randomly distributed at the top of the surface cavities. For the simulations of the SLM-printed outer conductor, we used $w = 100$ µm and $h = 50$ µm; simulations of the ADAM-printed case used the SEY data for the "effective trench" in Fig. 5.16.

The results of the PIC simulations are shown in Fig. 5.18. These data were generated using the procedure we described in Chapter 2 and are compared with our simulations of the smooth, copper transmission line. Based on these simulations, we expect the 3D-printed surfaces to cause a modest increase in the breakdown threshold. This improvement is approximately uniform over the full range of fd, and the ADAM-printed surfaces have a somewhat larger effect.

5.3 Experimental Results

In our simulations, we saw that the 3D-printed coaxial outer conductors can reduce the presence of multipactor in our transmission line. We now present experimental results to demonstrate that these predictions correlate to real-world events. For these tests, we have replaced the center segment of the coaxial transmission line with one of the 3D-printed outer conductors.

5.3.1 Cold Test Data

When we replace the outer conductor of the coaxial transmission line, there is the potential that the 3D-printed structure may affect the RF signals. A series of cold tests were performed to demonstrate that the attenuation across the vacuum chamber is not significantly altered by the 3D-printed outer conductors.

Cold test results for the coaxial transmission line with an SLM-printed outer conductor are shown in Fig. 5.19. Also shown is a comparison (indicated by dashed lines) with the data from the original, machined surfaces. To highlight the shift in the transmission properties, we only present data near the operating frequency of 3.05 GHz. These data show that the 3D-printed segment does not significantly alter the transmission line's S-parameters; the attenuation is only increased by $\sim$0.1 dB. Reflections are affected somewhat more significantly, though S_{11} remains within a tolerable range. The modest shift in attenuation, which is on the order of the uncertainties in our power measurements, shows that replacing components with their SLM-printed counterparts will not significantly reduce their performance.

This is further supported when we look at the cold test data for the ADAM-printed outer conductor. These data are shown in Fig. 5.20. Although we use a different set of inner conductors for testing the ADAM-printed segment's multipactor properties, these cold tests use the same inner conductors as the original machined transmission line. This provides a better assessment on how the ADAM-printed structures will affect the transmission line. Again, we see that the S-parameters do not significantly change when we use the 3D-printed segment.

These data have all shown that replacing part of a coaxial transmission line with a 3D-printed alternative will not significantly alter the S-parameters. This suggests that 3D-printed components have the potential to be used as drop-in replacements without significantly attenuating or reflecting the drive signal. This presents manufacturers with the opportunity to replace existing parts with 3D-printed alternatives that can potentially prevent multipactor.

Finally, we present cold test data for the ADAM-printed outer conductor coupled with the inner conductors that we will use for the susceptibility measurements. These data, shown in Fig. 5.21, reflect a slight improvement in performance when compared to the original machined transmission line. This is likely due to a minor shift in the quarter-wave transformers' dimensions when the newer inner conductors were machined.

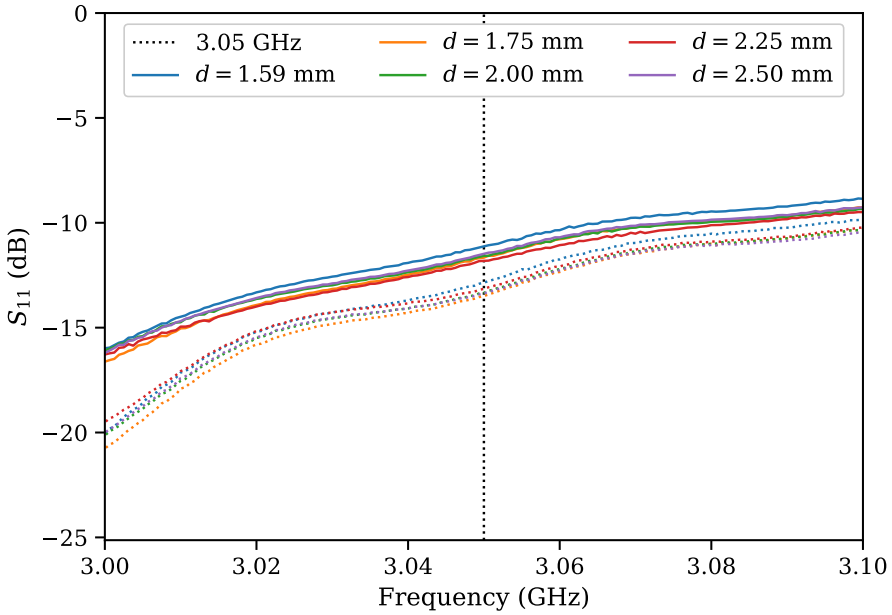

(a) Reflected power, S_{11}

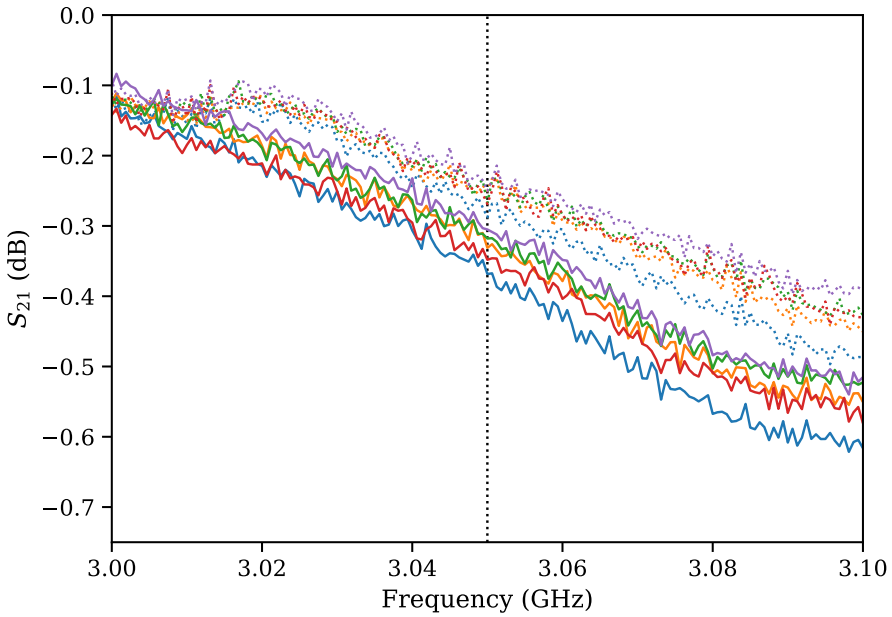

(b) Transmitted power, S_{21}

Figure 5.19: Cold test data of the coaxial transmission line with an SLM-printed outer conductor, with S_{11} in (**a**) and S_{21} in (**b**). These data are compared to data from the fully-machined structures, which are shown as dotted lines. The vertical, dotted line represents the 3.05-GHz drive signal used in the experiment.

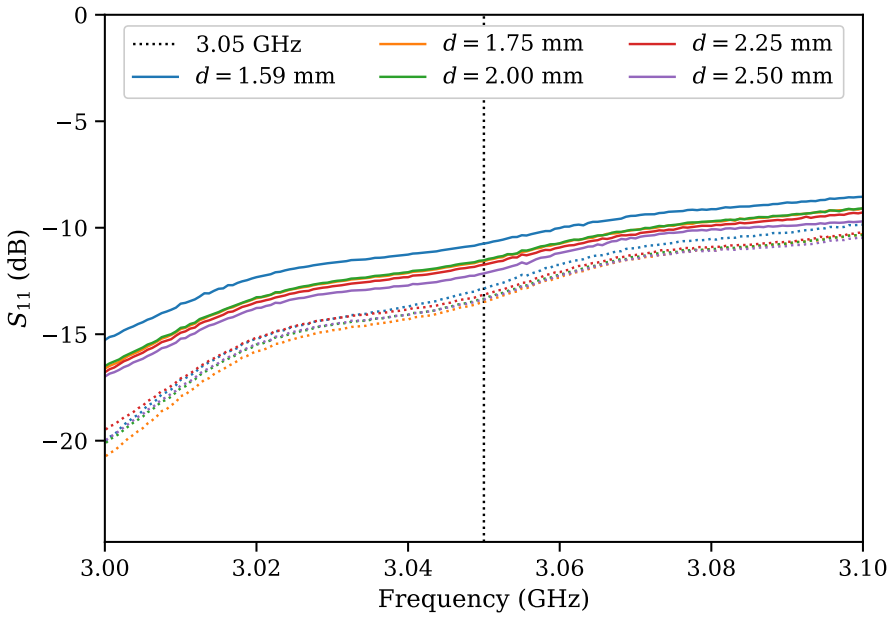

(a) Reflected power, S_{11}

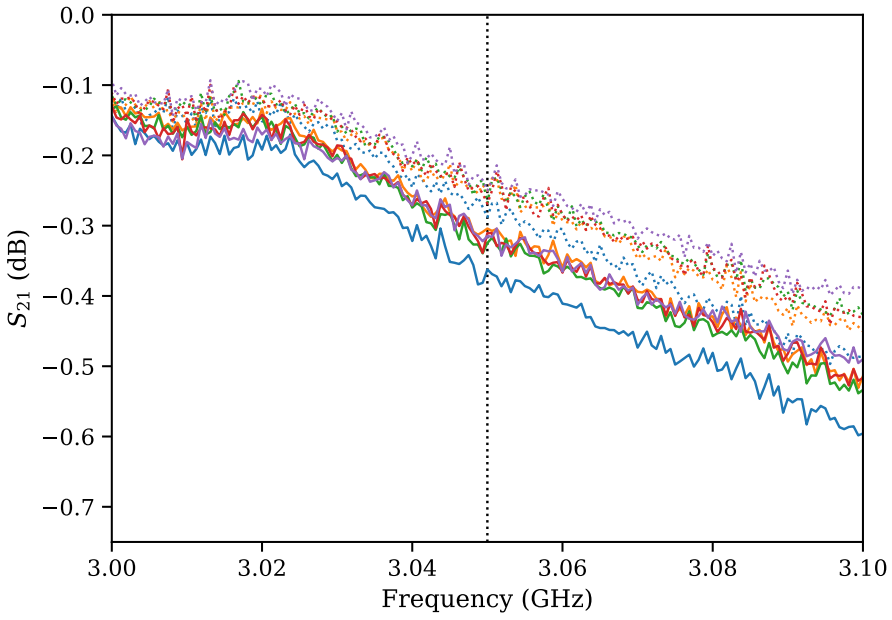

(b) Transmitted power, S_{21}

Figure 5.20: Cold test data of the coaxial transmission line with an ADAM-printed outer conductor, with S_{11} in (**a**) and S_{21} in (**b**). This test used the same inner conductors used for the machined and SLM-printed experiments to allow for better comparisons with the fully-machined structures, which are shown as dotted lines. The vertical, dotted line represents the 3.05-GHz drive signal used in the experiment.

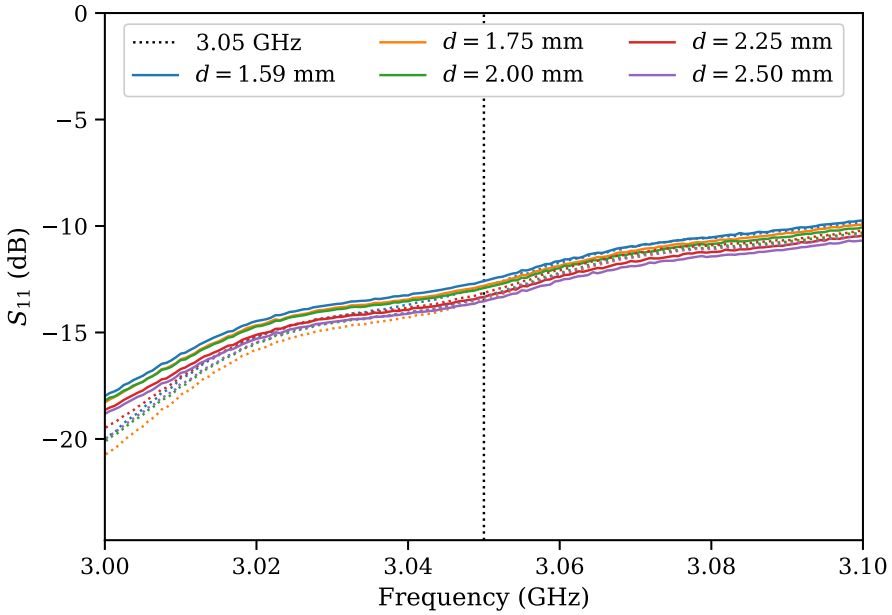

(a) Reflected power, S_{11}

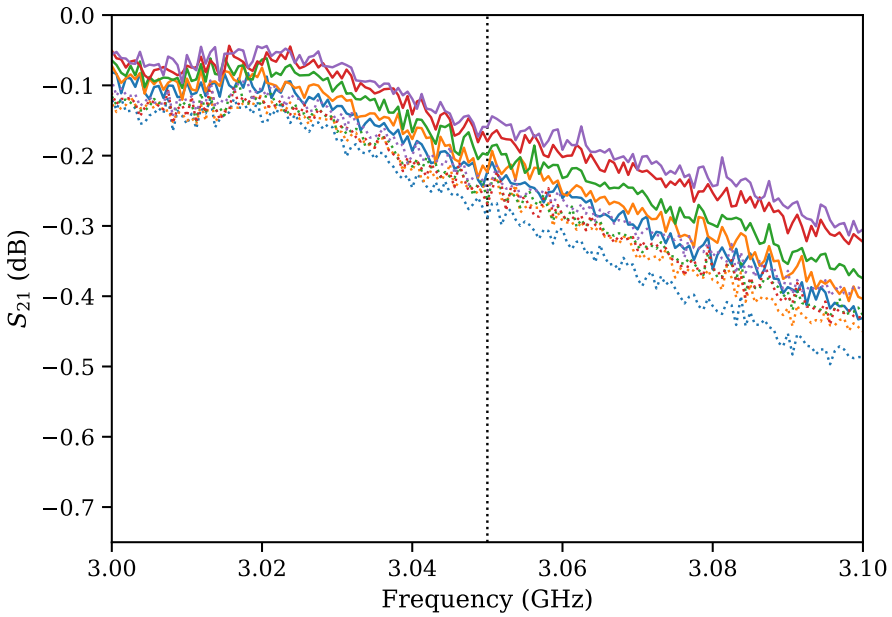

(b) Attenuated power, S_{21}

Figure 5.21: Cold test data of the coaxial transmission line with an SLM-printed outer conductor and the shortened inner conductors used for multipactor breakdown testing, with S_{11} in (**a**) and S_{21} in (**b**). These data are compared to data from the fully-machined structures, which are shown as dotted lines.

5.3.2 Multipactor Susceptibility

Experimental measurements of the 3D-printed coaxial transmission line's susceptibility diagram are presented in Fig. 5.22. These data are compared to the original machined surfaces, in black. We present the results for both the SLM and ADAM-printed outer conductors, with comparisons to CST PIC simulations shown as dashed lines. Our first, and most obvious, observation is that the 3D-printed surfaces have a profound effect on the multipactor susceptibility. When we introduced the SLM-printed outer conductor, the breakdown threshold consistently increased by 2.5 kW over the full range of fd;[6] even higher gains were achieved when we used the ADAM-printed outer conductor. Overall, the 3D-printed structures have proven to be extremely effective for preventing multipactor.

In Fig. 5.22, we see that the 3D-printed outer conductors far out-performed our simulations. This discrepancy is due to the highly approximate models we used to represent the 3D-printed metals' surface structures. Although we attempted to correct for this when modeling the ADAM-printed SEY, the SLM-printed surfaces only vaguely resemble the infinite array of pyramidal cavities that

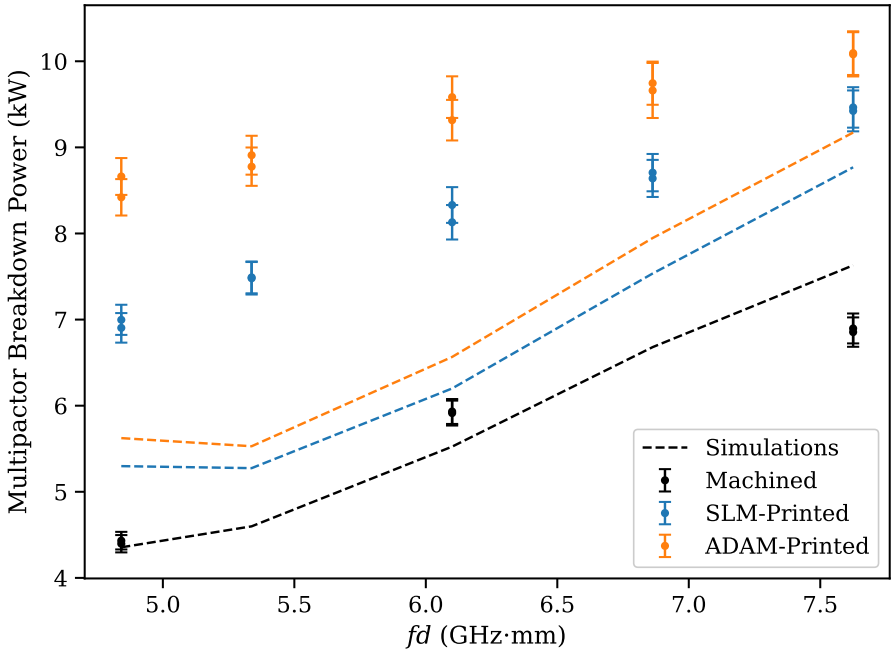

Figure 5.22: Experimentally measured susceptibility diagram of a coaxial transmission line with a 3D-printed outer conductor. Also shown are experimental data for the original machined surfaces (in black) and the PIC simulations of the printed transmission line (dashed lines).

.

[6]These increases are tabulated in decibel units in Chapter 6.

we assumed. We chose these models because they are convenient; they allow us to implement very simple ray-tracing algorithms to calculate the SEY. We reduced complex surface structures such that they can be described by only two parameters: a cavity width and depth.

More accurate simulations could certainly have been achieved if we used a full, three-dimensional representation of the real surface structure. Laser-scanning microscopes can generate 3D maps of the surface morphology, which then could be coupled to an advanced ray-tracing model to track the electron motion. Although previous studies have used these maps to characterize surfaces for multipactor simulations, they only used a simple ray-tracing algorithm (like ours) to generate SEY data, and they represented the surfaces as infinite arrays of perfectly cylindrical pores [86, 87]. Although more robust ray-tracing models that can consider extremely complex geometries do exist [114], they are generally focused on rendering video graphics, and their implementation is beyond the scope of this work.

CHAPTER 6

Conclusions and Suggestions for Future Work

Multipactor discharges are extremely dangerous. Not only will they disrupt the operation of vacuum electronics, but they can potentially destroy them. In space communication systems, preventing multipactor is of utmost importance because it is impractical, or even impossible, to repair or replaced damaged components. Unfortunately, to prevent multipactor we must know when it will occur.

We have discussed how multipactor theory is deceptively simple. The classical, resonant model fails to describe the effects from realistic, distributed electron energies and completely ignores chaotic and high-periodicity electron dynamics. A more modern theoretical model based on chaos theory addresses these issues and offers a near-perfect representation of multipactor as it is understood today. Unfortunately, this advanced theory is extremely computationally expensive and its implementation is often impractical, particularly for complex geometries. Simulations can fill in the blanks left by the theory, but are dependent on difficult-to-characterize material parameters. Experiments can characterize the multipactor behavior of real devices, but have generally been limited to sub-gigahertz frequencies and low-fd regimes.

This work broadens our understanding of multipactor by presenting a new experimental platform for studying multipactor in a coaxial transmission line. This experiment operates at higher frequencies than previous work and extends to high-fd conditions that had previously been unexplored.

The multipactor test cell was designed based on CST Particle Studio simulations. These particle-in-cell simulations, and our chosen SEY model, were initially benchmarked against published experimental results. After confirming that our simulations agreed with Woo's classic experiment to within a few percentage points, we simulated a design for a stepped-impedance coaxial transmission line. We later confirmed that the predicted breakdown threshold power from our simulations agreed with our experimental measurements within a margin of 10%.

Our experimental investigation also characterized the multipacting self-conditioning phenomenon. During this process, the multipacting electrons directly alter the transmission line's surface properties. This is likely due to a combination of effects. First, the ongoing electron

bombardment can heat up the conductors' surfaces. This can simulate a bake-out procedure and release trapped gases from the metal surfaces. Copper oxide layers, which generally enhance secondary electron emission and encourage multipactor, may also be damaged—either through sputtering or outgassing—and cause the breakdown threshold to increase significantly. Multipactor self-conditioning may also cause micro-scale surface structures to melt and deform. This will reduce surface protrusions and remove field enhancement points. Future experiments may attempt to characterize these surface alterations by comparing SEM images and XEDS analyses from before and after multipactor conditioning. We also found that multipactor self-conditioning is relatively rapid on human time-scales. Our ninety-minute-long conditioning experiments correspond to only a few hundred milliseconds of continuous multipactor. In a continuous-wave experiment, these effects may occur before measurements are possible.

Several diagnostic systems are present in the test cell for characterizing multipactor discharges. These include both direct and indirect methods for measuring the multipactor electrons. An electron multiplier tube and an electron probe directly sample the current of electrons striking the outer conductor, and two directional couplers sample the RF-power signals entering and leaving the multipacting transmission line, providing an indirect indication of multipactor. In particular, we have found that the reflected power signals are the most sensitive to multipactor. These measurements have become our primary indicator of breakdown when measuring the test cell's susceptibility to multipactor.

Potential improvements to the multipactor test cell include enhancements to our diagnostic suite. Several additional diagnostics will not only provide additional indicators for multipactor, but will also allow us to better characterize the nature of the multipactor discharges. One such diagnostic is an improvement on our electron probes. Currently, we use an unbiased electron probe. Although this means that it is an extremely simple device, this limits both the probe's sensitivity and measurement capabilities. A biased electron probe, similar to a conventional Langmuir probe used for characterizing gas discharges, can be used to quantify the multipactor electrons' energy spectrum. This information can allow us to tailor the transmission line's secondary emission properties to maximize multipactor suppression.

Our RF power measurements can also be used to provide an additional diagnostic signal. Multipactor can cause a microwave signal to shift in phase. This can be an extremely sensitive indicator for multipactor. By using an RF phase-shifter and signal combiner to cancel out the forward and transmitted power signals, any phase-shift caused by multipactor will be readily apparent. Unfortunately, initial attempts to implement a phase-nulling diagnostic in our experiment have so far been unsuccessful. This may be due to non-linearities in our variable attenuator combined with frequency-pushing effects in the magnetron [115] that are enhanced by the Scandinova modulator's long rise-time.

TABLE 6.1
INCREASE IN BREAKDOWN POWER THRESHOLD FROM 3D-PRINTED SURFACES

	SLM-Printed		ADAM-Printed	
fd	**Simulation**	**Experiment**	**Simulation**	**Experiment**
$4.84\ \mathrm{GHz \cdot mm}$	$0.85\ \mathrm{dB}$	$1.97 \pm 0.10\ \mathrm{dB}$	$1.11\ \mathrm{dB}$	$2.87 \pm 0.10\ \mathrm{dB}$
$6.10\ \mathrm{GHz \cdot mm}$	$0.50\ \mathrm{dB}$	$1.43 \pm 0.11\ \mathrm{dB}$	$0.75\ \mathrm{dB}$	$2.03 \pm 0.11\ \mathrm{dB}$
$7.63\ \mathrm{GHz \cdot mm}$	$0.60\ \mathrm{dB}$	$1.38 \pm 0.11\ \mathrm{dB}$	$0.80\ \mathrm{dB}$	$1.67 \pm 0.11\ \mathrm{dB}$

Textured surfaces reduce secondary electron emission by trapping electrons within microscopic structures. Because these trapped electrons are unable to reach the bulk vacuum, they cannot contribute to multipactor. Additive manufacturing is a convenient tool for producing these textured surfaces. We have proposed and explored a method for suppressing multipactor by implementing a partially 3D-printed transmission line.

We have adapted a Monte-Carlo model to simulate the texture-modified SEY curves. This model uses a simple ray-tracing algorithm to track the electrons that are reflected by the surface microstructures. These simulations revealed that textured surfaces exhibit interesting behavior when electrons impact at oblique angles. Highly textured surfaces will stray from the frequently-used scaling law that was originally introduced as part of the Vaughan model [26, 27]. This suggests that multipactor simulation platforms must include user-input angular SEY curves to ensure accurate results.

Particle-in-cell simulations based on our textured SEY model suggested that the breakdown threshold will increase significantly if we used a partially 3D-printed transmission line. Our experimental investigation, whose results are summarized in Table 6.1, showed improvements that our simulations significantly under-predicted. According to our simulations, an SLM-printed transmission line will increase the breakdown threshold by 0.50–0.85 dB, depending on fd; an ADAM-printed structure was predicted to have a somewhat larger effect on the breakdown threshold.

Our experimental results on the on 3D-printed transmission line consistently outperformed our simulations, and they were extremely effective for preventing multipactor. In particular, the ADAM-printed outer conductor nearly doubled the breakdown threshold at our low-fd limit. These experiments have proven that 3D-printed, textured coaxial transmission lines can act as drop-in replacements in existing devices and provide valuable margin from multipactor.

Future experiments can build on this work to explore the limits on preventing multipactor with 3D-printed components. Such experiments may include quantifying the additional benefit from also implementing a 3D-printed inner conductor. It will also be interesting to investigate how the printing parameters may affect the multipactor susceptibility. Macroscopic surface perforations have been shown to be an effective tool for suppressing multipactor [89]. When the surface porosity

was sufficiently high, electron-leakage through the conductor's surface completely eliminated multipactor in a microstripline [89]. Adapting this method to a coaxial transmission line presents unique difficulties. Manufacturing a highly-perforated cylindrical conductor using traditional machining techniques would be both time consuming and expensive, with no guarantee for success. However, producing such a part via additive manufacturing would be trivial; 3D-printers can easily produce arbitrarily shaped components that would otherwise be non-machinable. Such a component will combine multipactor suppression effects from both the surface perforations and the 3D-printed surface texture.

Several recent studies have suggested several other novel techniques for preventing multipactor. These methods include implementing modulated (both digital and analog) signals [19, 82], multi-carrier drive frequencies [60, 116], and even non-sinusoidal RF excitations [66]. These methods provide a unique opportunity to prevent multipactor in existing systems where hardware changes are not an option. However, testing them in our high-fd experimental platform will require a high-power, wideband microwave generator.

We do not claim that we have solved multipactor. However, we have shown that our coaxial multipactor test cell at the University of Michigan is a powerful tool for researching this phenomenon. This new experimental platform will continue to be used to demonstrate novel methods for suppressing multipactor. Hopefully, this work will allow us to someday eliminate multipactor once and for all.

APPENDIX A

High Voltage Modulators

Two high voltage modulators were used in this experiment for driving the magnetron. Their specifications are summarized in Table A.1. The Stanford modulator has been previously discussed by Exelby [117], so we will focus on the Scandinova M1.

A.1 Scandinova M1 Modulator

The Scandinova M1 is a software-controlled, solid-state magnetron modulator; an approximate circuit model is shown in Fig. A.1. Unlike a hard-tube modulator or a pulse forming network, the Scandinova modulator does not operate by adding high voltage pulses. Instead, it uses a split-core transformer to step-up a lower voltage input pulse. Three solid-state IGBT switches convert a DC high voltage, V_{dc} into three square pulses that are applied to the transformer's six primary coils. The transformer combines these pulses, which are then stepped up by a factor of $N \approx 40$. An additional low-voltage DC power supply, which floats on top of the modulator's output pulses, provides current to heat the magnetron's thermionic cathode.

The modulator's output voltage is controlled by adjusting the DC high voltage power supply. To power the E2V MG5223F magnetron used in this experiment, we use $V_{dc} = 230$ V. A peaking

TABLE A.1
HIGH VOLTAGE MODULATOR SPECIFICATIONS

	Stanford 334M		**Scandinova M1**	
	Minimum	**Maximum**	**Minimum**	**Maximum**
Output Voltage		40 kV	~14 kV	47 kV
Output Current		30 A		100 A
Repetition Rate	16.8 Hz	2000 Hz	Triggered	300 Hz
Pulse Width	0.1 µs	5 µs		5 µs
Heater Voltage		25 V		10 V
Heater Current		2 A		10 A

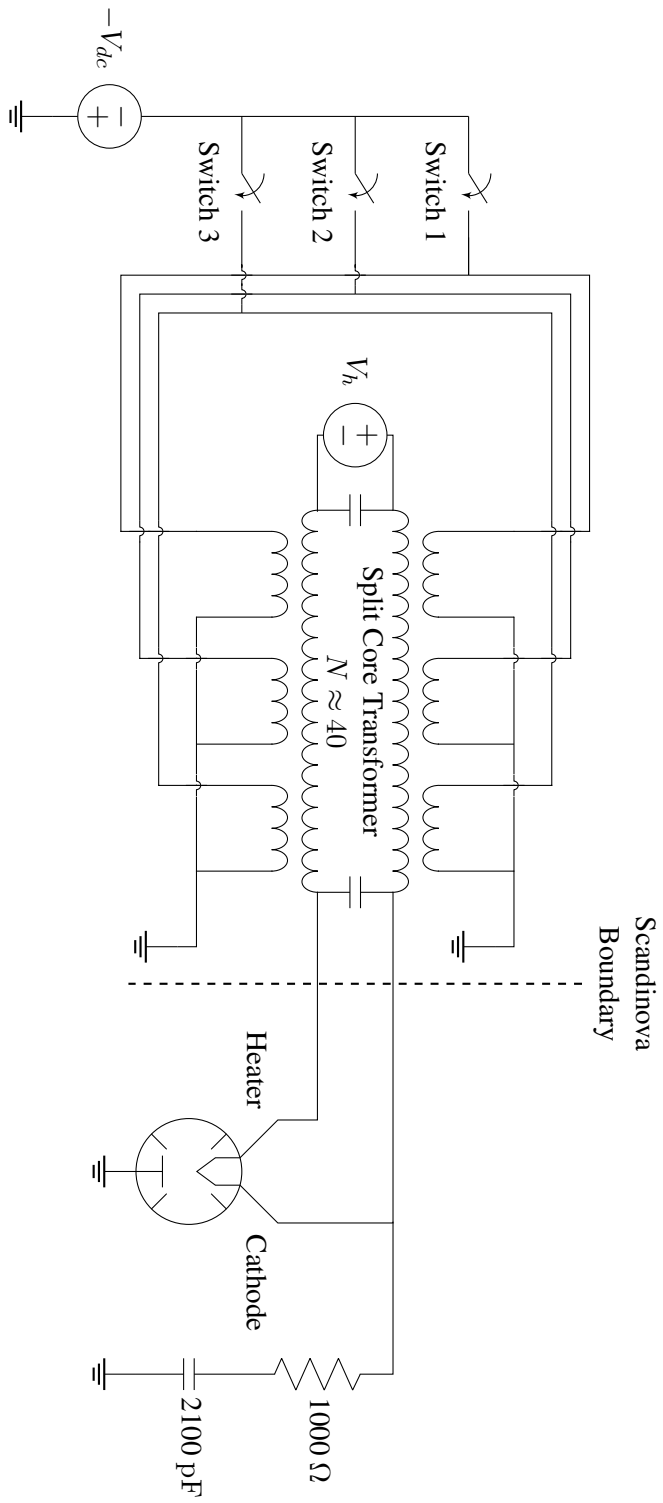

Figure A.1: Approximate circuit diagram for the Scandinova M1 modulator.

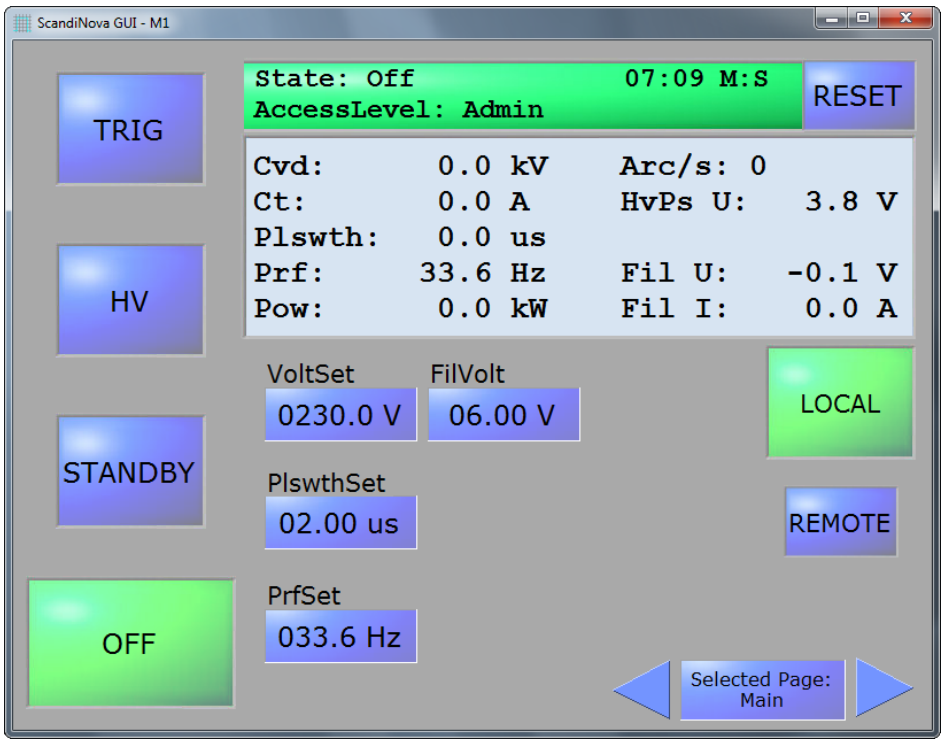

Figure A.2: Screenshot of the graphical user interface for the Scandinova modulator. The setting shown here represent the typical set-points used when running our experiments.

capacitor ($C = 2100$ pF) and resistor ($R = 1000\ \Omega$) parallel to the magnetron matches the load impedance and improves the output pulse-shape. A screenshot of the Scandinova control interface is shown in Fig. A.2, highlighting the settings we typically use when running our experiments.

A.2 Effect on Diagnostic Signals

The two modulators have a dramatic effect on the diagnostic signals. This is particularly important for the EMT and the electron probe; these signals are highly sensitive to noise at the start and end of the modulators' voltage pulses. Eliminating this noise experimentally has proven to be difficult; however, we can extract the diagnostics' signals during post-processing. Note that this signal noise was much more significant when using the Stanford modulator and would completely obscure the EMT and electron probe signals when operating near the multipactor breakdown threshold.

The diagnostic noise was evident when we examine the raw probe data in Figs. 4.2, 4.3, and 4.4. Fortunately, the low-frequency component of the noise is consistent on a shot-to-shot basis. The diagnostic signals are revealed by subtracting a reference shot—recorded at low power and with no multipactor—from the raw data. We then use a digital, low-pass filter to eliminate the random,

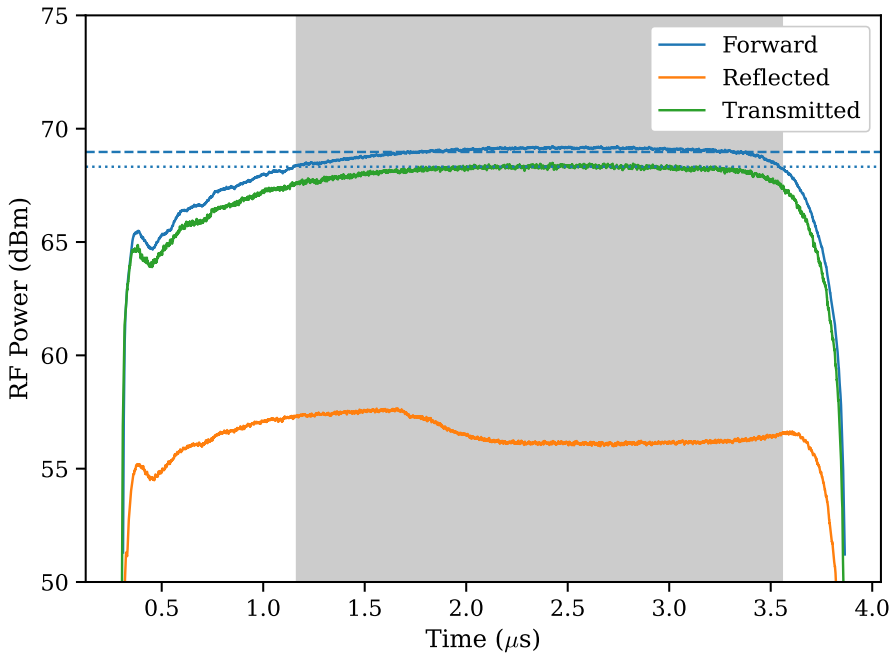

Figure A.3: Power signal data used for calculating the average power when using the Scandinova modulator.

high-frequency noise component.

The choice in high voltage modulator also affects the RF power signals. When measuring the multipactor breakdown threshold, we typically use the average power during a shot. When the Stanford modulator is used to drive the magnetron, this is not an issue because the RF power is supplied in near-perfect square pulses; the average power will be representative of the RF power at the time of multipactor onset. However, voltage pulses from the Scandinova modulator have a relatively long rise-time. As a result, averaging over the full pulse-length will under represent the RF-power at multipactor onset. This is illustrated in Fig. A.3, which shows the RF power (in units of dBm). When averaged over the entire pulse—represented as a dotted line—the forward power level is significantly lower than the pulse's flat-top.

Because of this, we will only use the data that corresponds to when the forward-power Schottky diode signal is greater than 90% of its maximum value; this is indicated by the shaded region in Fig A.3. This average—represented as a dashed line—better represents the flat-top. When the overall power level is close the breakdown threshold, multipactor should occur during the highest-power segment of the RF pulse. This means that our reported data will be a better representation of the multipactor discharge. Our average power measurements are also presented with the standard deviation over the high-power segment of the pulse.

APPENDIX B

RF Power Calibrations

In this appendix, we present updated procedures for calibrating our RF power measurements.

B.1 High Precision Line Attenuation Measurements

We measure the RF power using a set of Schottky diodes. Figure B.1 illustrates the basic setup for these measurements. The RF power is first sampled by a directional coupler and then travels to the screen room via a long coaxial cable. A series of attenuators reduces the power level before it is measured by the Schottky diode and recorded as a voltage trace on an oscilloscope. A set of calibrations (described in Sec. B.2) relates the voltage signal to the power absorbed by the diode. To determine the power level at the experiment, we must account for the attenuation from each component in Fig. B.1.

In the past, we would separately measure the attenuation of each component using a vector network analyzer (VNA). However, this often requires several gender-adapters, and the cable attenuation could not be measured directly. Ordinarily, their effect would be unimportant, but this experiment requires us to minimize the uncertainty in our power measurements so we can reliably describe multipactor.

We propose an alternative method—illustrated in Fig. B.2—for precisely measuring the total line attenuation. Instead of using a VNA and measuring each component separately, we use a pair of bolometers (Agilent models E4412A and 8481A) and a signal generator (Agilent model E4422B). Data from the bolometers are obtained using two HP/Agilent E4418B power meters. A 3.05-GHz signal is injected into the directional coupler. A bolometer measures the power transmitted through

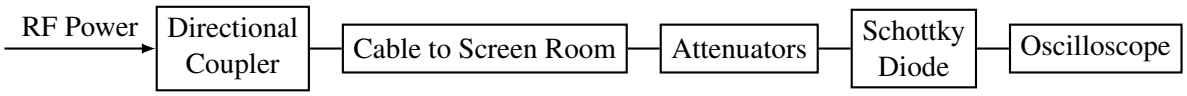

Figure B.1: Block diagram of the equipment for measuring the RF power.

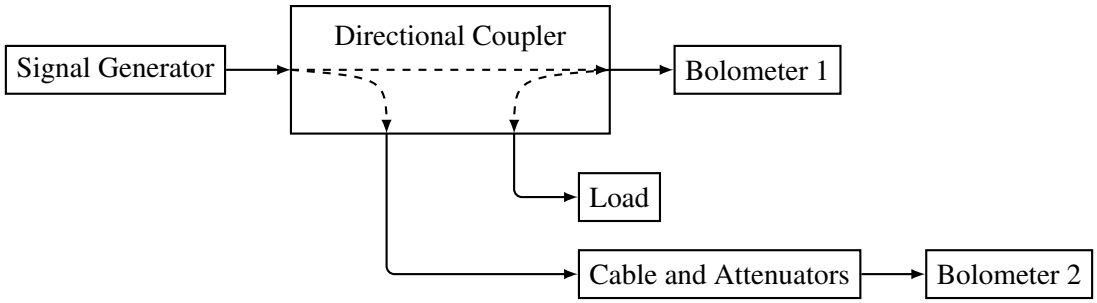

Figure B.2: Block diagram representing the apparatus used for precisely measuring the line-attenuation.

the directional coupler; this represents the signal that would be deliver to or reflected by the vacuum chamber. In the control room, a second directional coupler measures the power that would be delivered to the Schottky diode after it has passed through the directional coupler, cable, and attenuators. The line attenuation is the difference between these two measurements.

B.2 Schottky Diode Calibrations

Our Schottky diode calibrations are based on the procedure originally presented by Greening [94] in his dissertation. We now present an update to this procedure to reflect changes in our equipment. The principal apparatus are: two bolometers (Agilent models E4412A and 8481A), two power meters (Agilent/HP E4418B), two circulators, an HP 489 traveling wave tube (TWT) amplifier, an Agilent E4422B Signal Generator, a Narda 3042B-10 coaxial directional coupler, and an oscilloscope. Each of the four Schottky diodes (HP/Agilent 8472B) used in this experiment were calibrated using this procedure. Due to limitations from our TWT, this procedure is performed at $1\ \mathrm{GHz}$. Despite this, our measurements at $3.05\ \mathrm{GHz}$ should be correct to within $\pm 0.2\ \mathrm{dB}$ [118].

This calibration is performed in two steps, which are illustrated in Fig. B.3. First, we use the two bolometers to correlate the two output ports on the directional coupler. The coupler's directivity is the difference between the two bolometer measurements. This is generally performed over a range of input powers to verify the coupler's linearity.

After calibrating the directional coupler, we replace Bolometer 1 with one of the Schottky diodes, which is then connected to an oscilloscope. The diode's signal voltage—corrected for the DC-offset on each of the oscilloscope's voltage scales—is then measured as a function of the input power, as indicated by the remaining bolometer and the coupler's directivity.

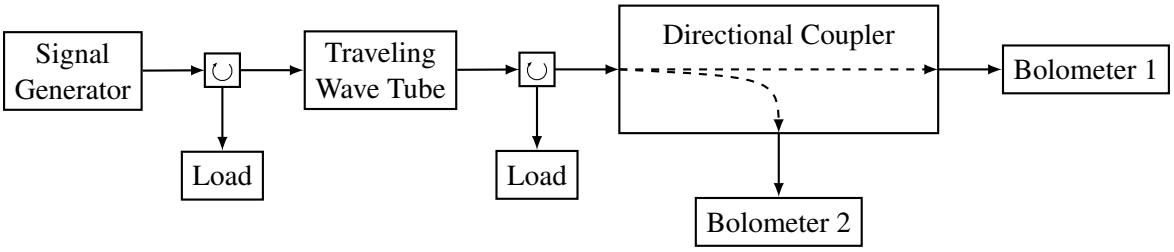

(a) Two-bolometer setup for calibrating the directional coupler.

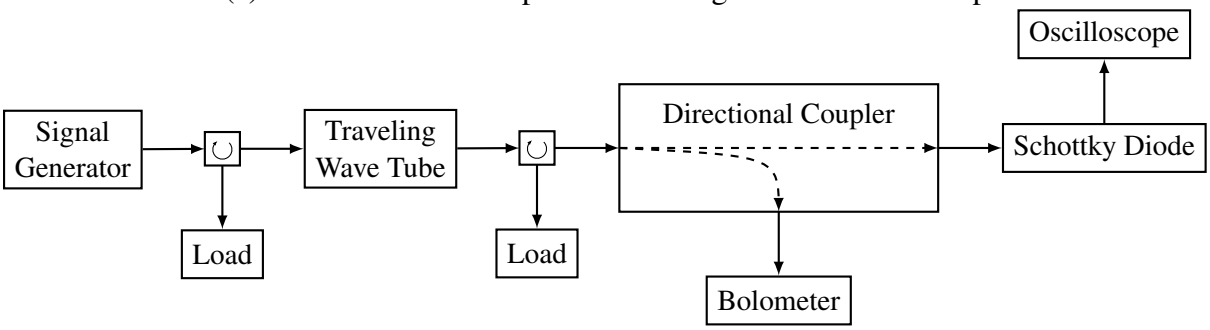

(b) One-bolometer setup for calibrating the Schottky diodes.

Figure B.3: Block diagram representing the apparatus used for the Schottky diode calibrations.

APPENDIX C

Technical Drawings and Schematics

This appendix presents technical drawings and schematics of the components that were manufactured to support this work.

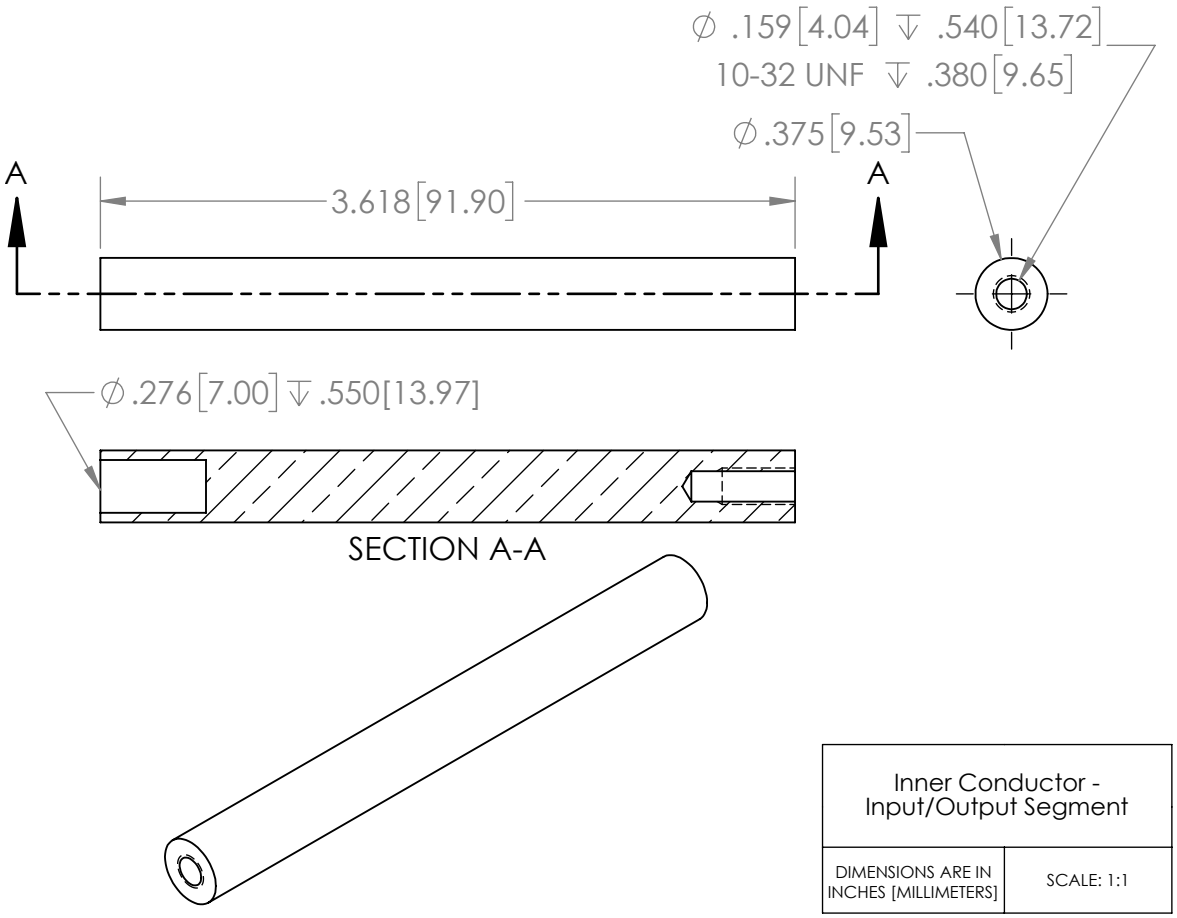

Figure C.1: Inner conductor input/output segment.

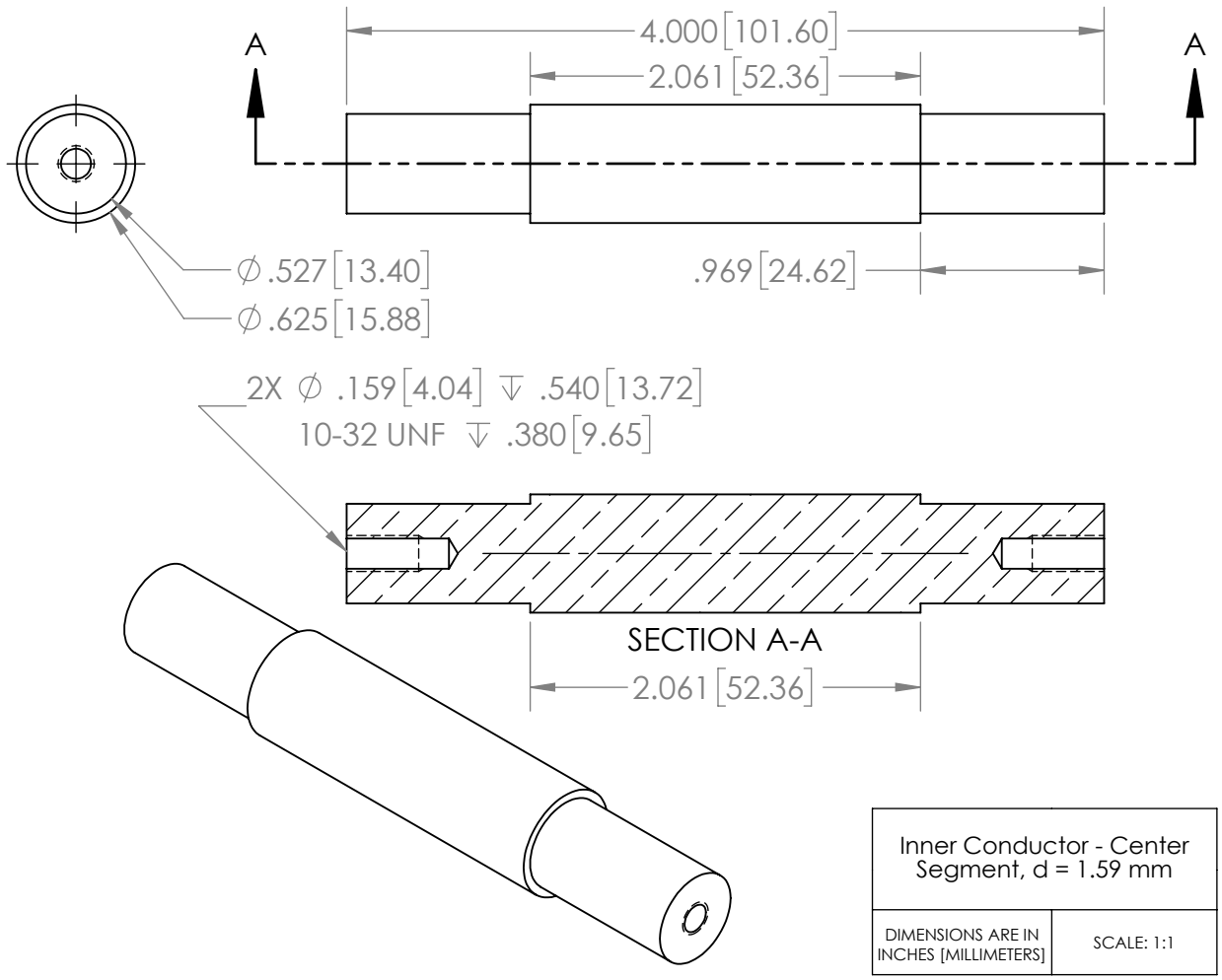

Figure C.2: Inner conductor center segment for case with $d = 1.59$ mm.

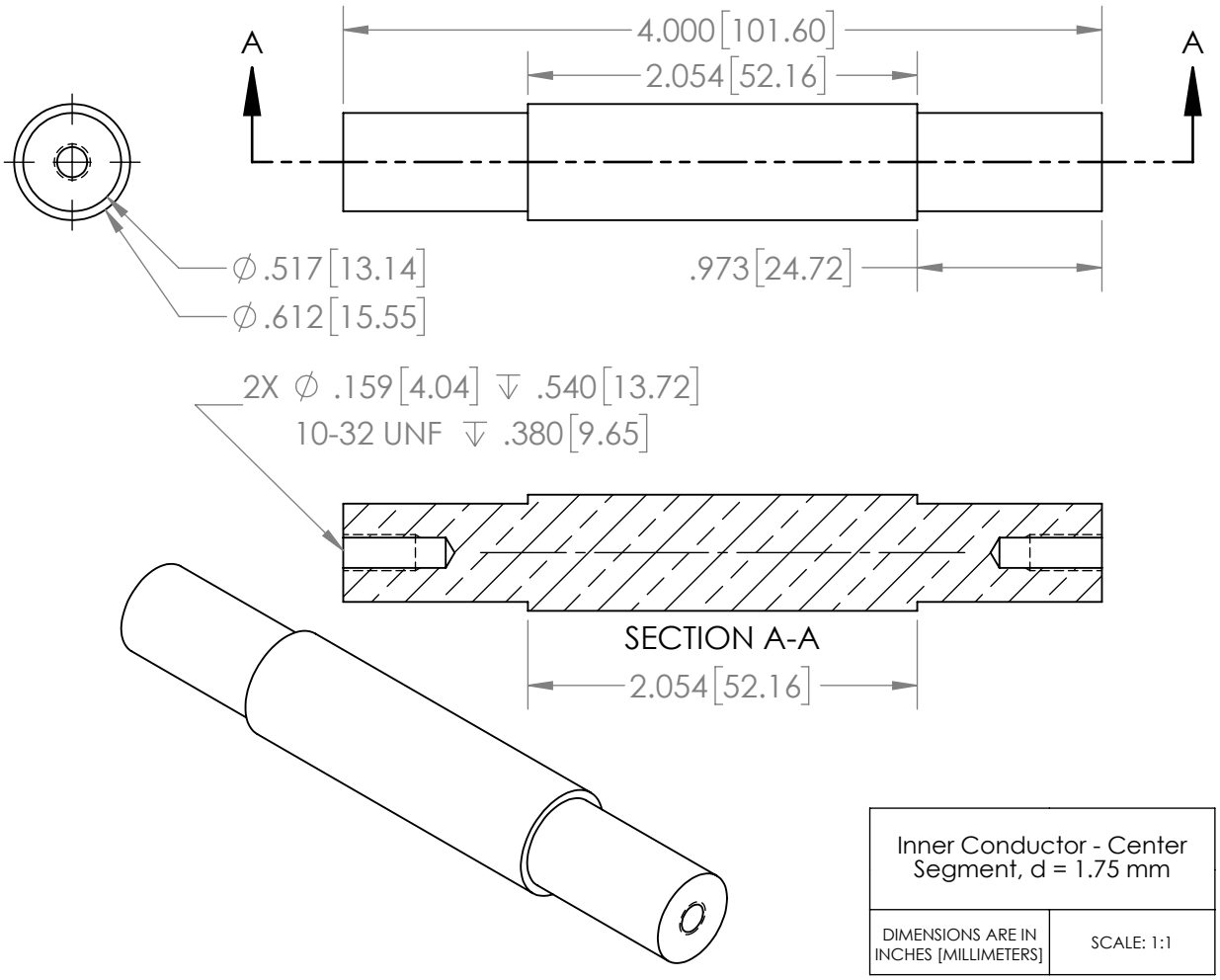

Figure C.3: Inner conductor center segment for case with $d = 1.75$ mm.

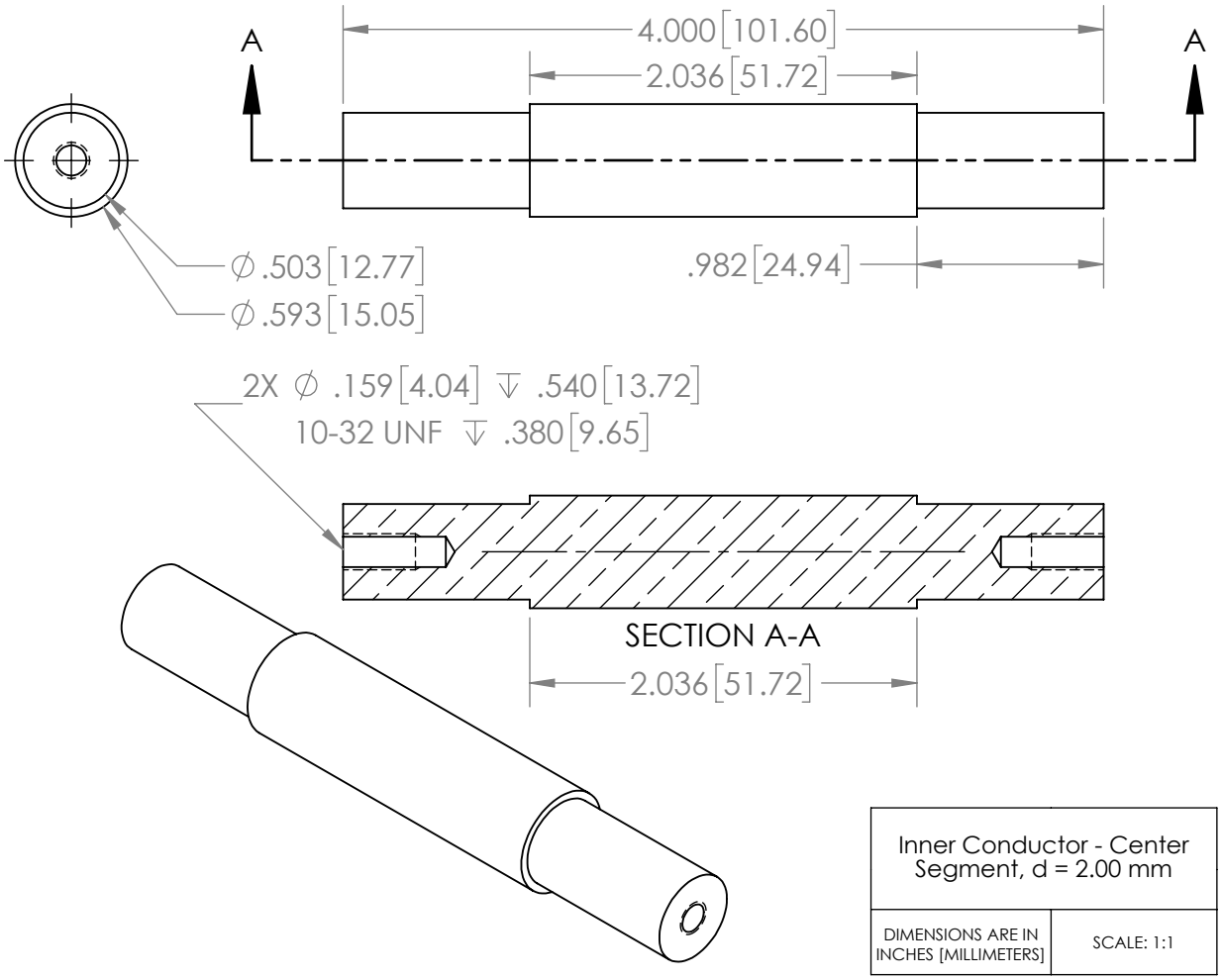

Figure C.4: Inner conductor center segment for case with $d = 2.00$ mm.

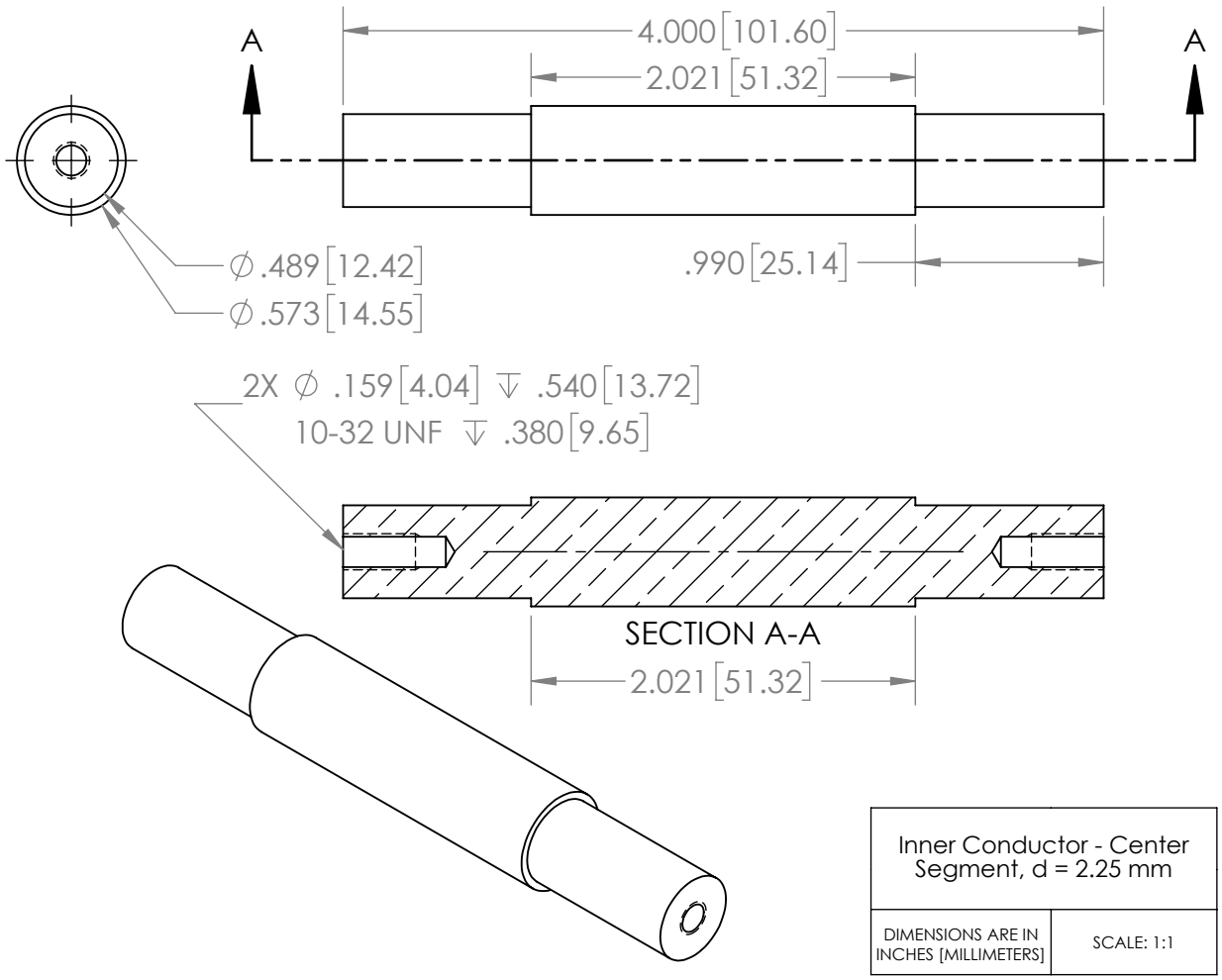

Figure C.5: Inner conductor center segment for case with $d = 2.25$ mm.

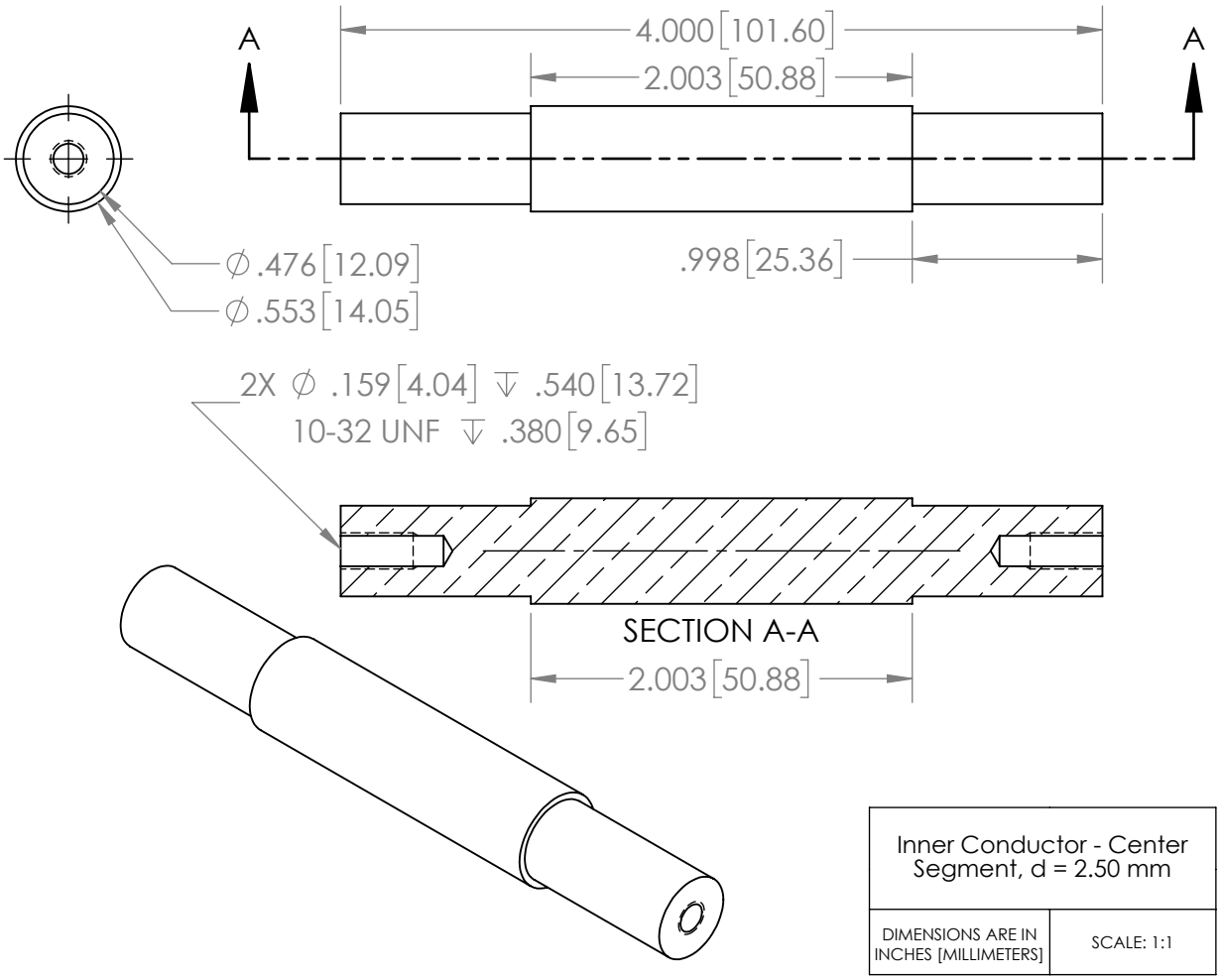

Figure C.6: Inner conductor center segment for case with $d = 2.50$ mm.

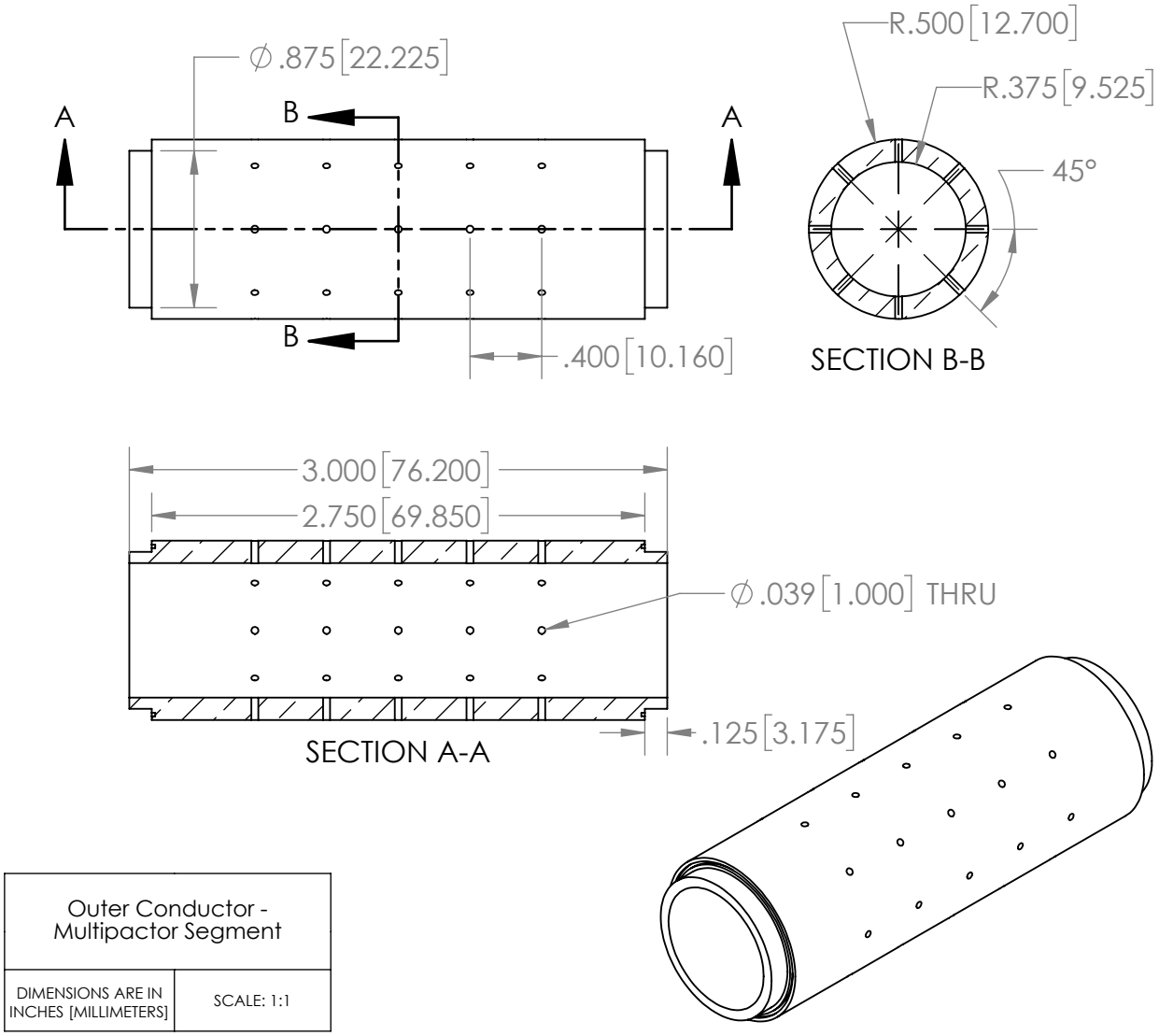

Figure C.7: Outer conductor multipacting segment.

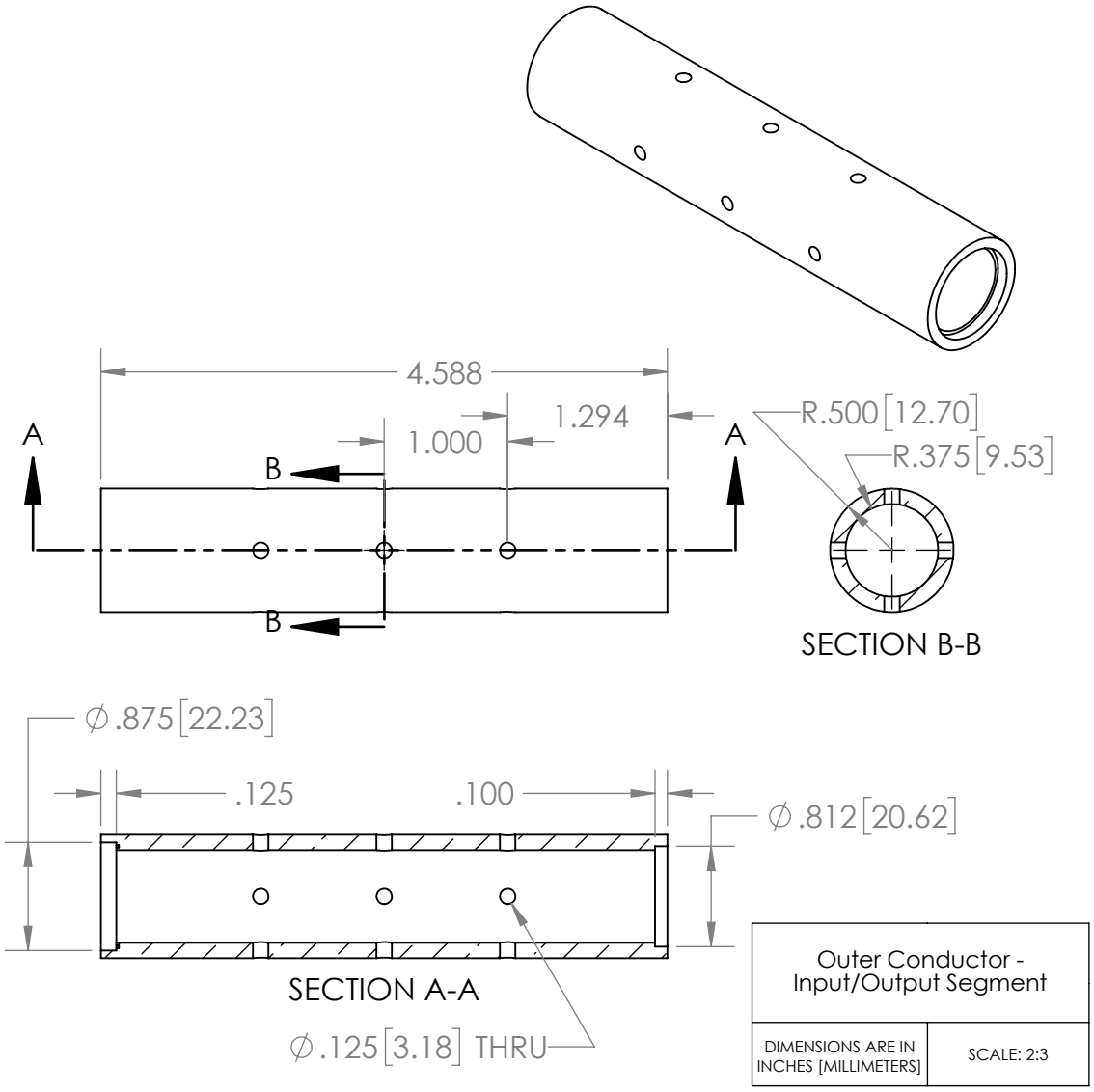

Figure C.8: Outer conductor input/output segment.

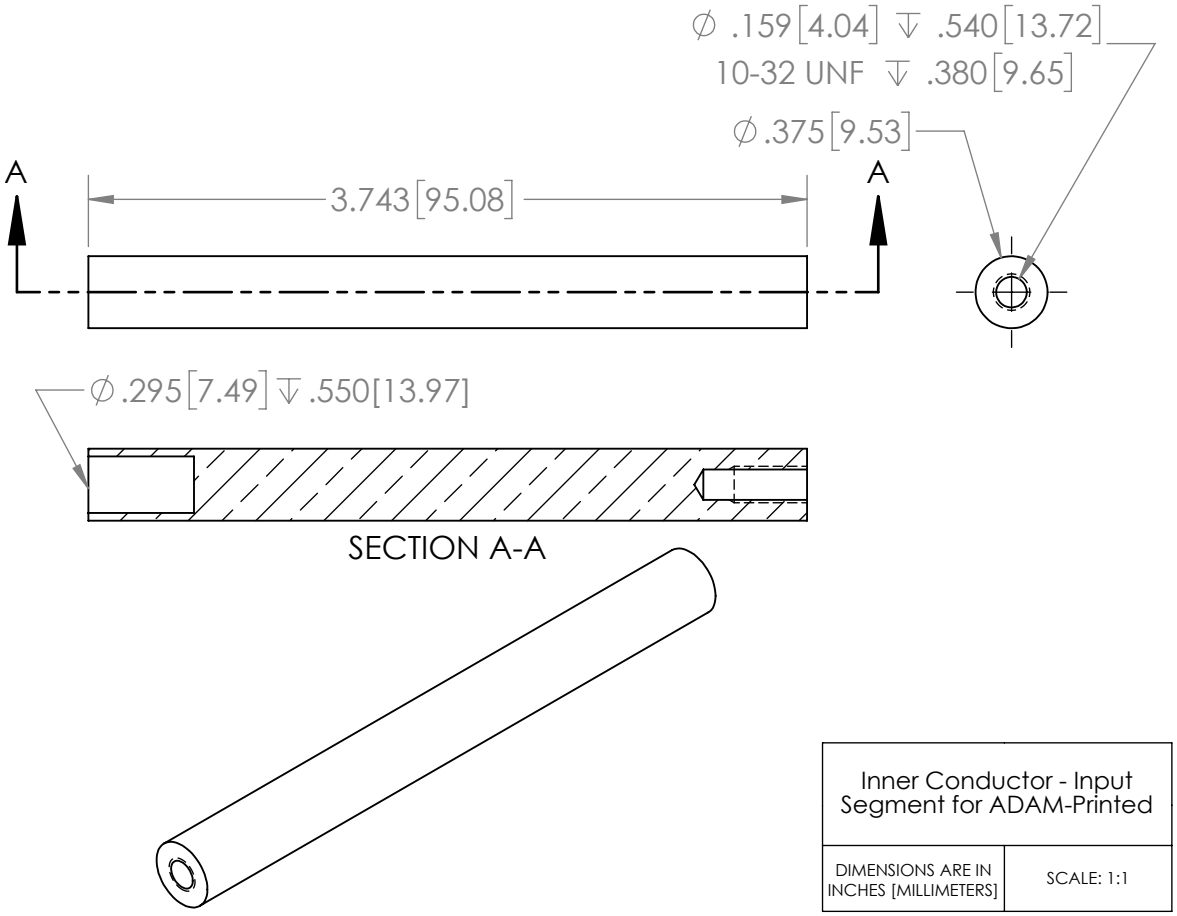

Figure C.9: Inner conductor input segment for use with the ADAM-printed outer conductor.

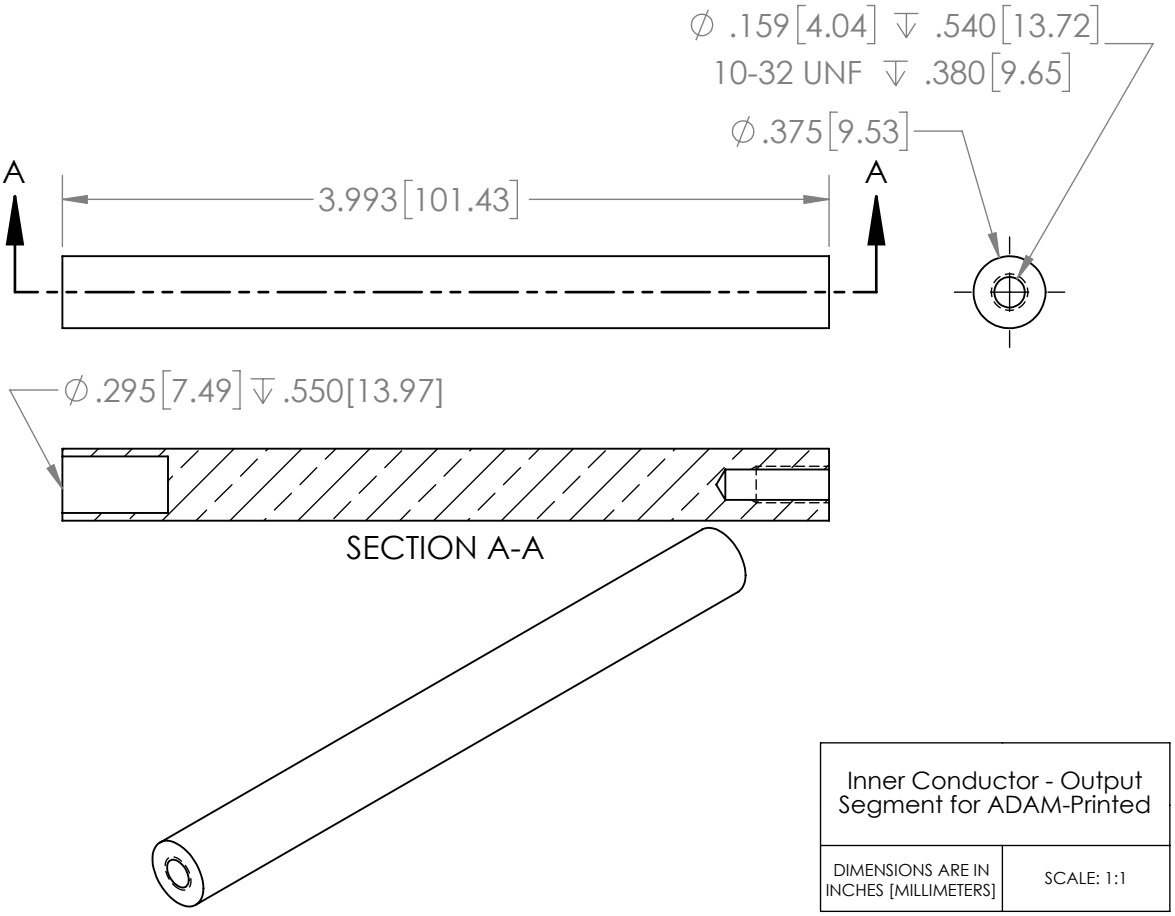

Figure C.10: Inner conductor output segment for use with the ADAM-printed outer conductor.

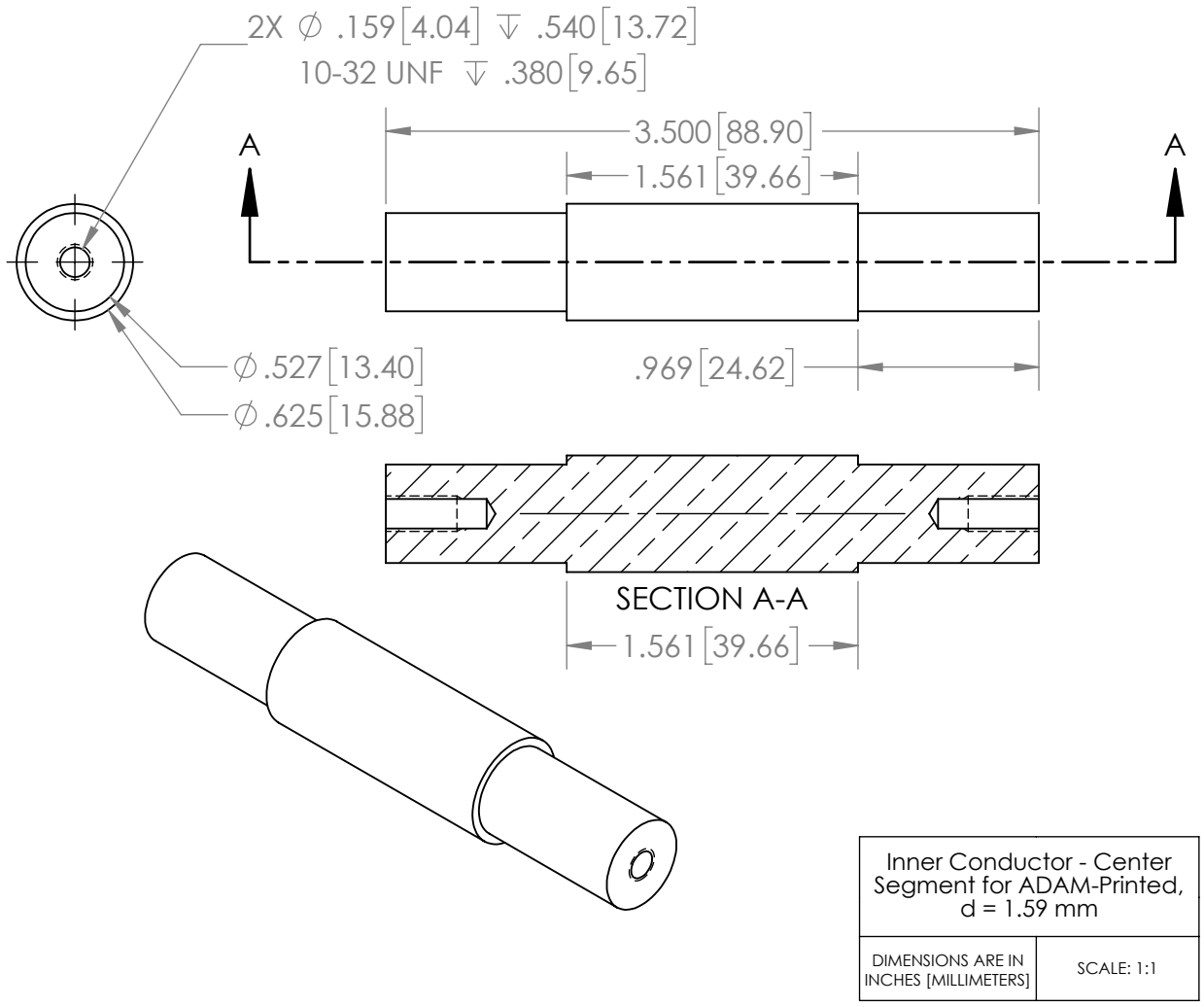

Figure C.11: Inner conductor center segment for use with the ADAM-printed outer conductor and with $d = 1.59\ \mathrm{mm}$.

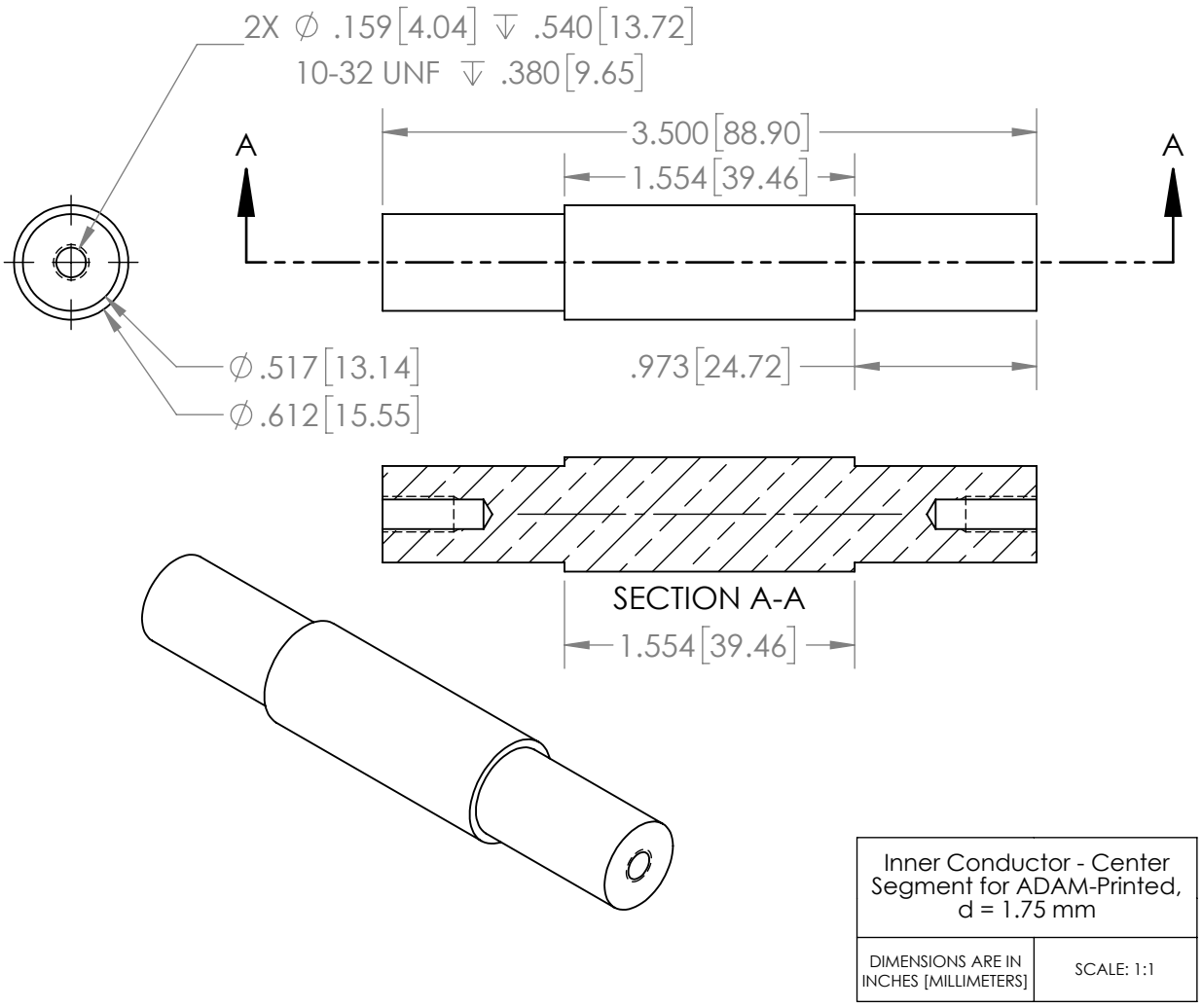

Figure C.12: Inner conductor center segment for use with the ADAM-printed outer conductor and with $d = 1.75$ mm.

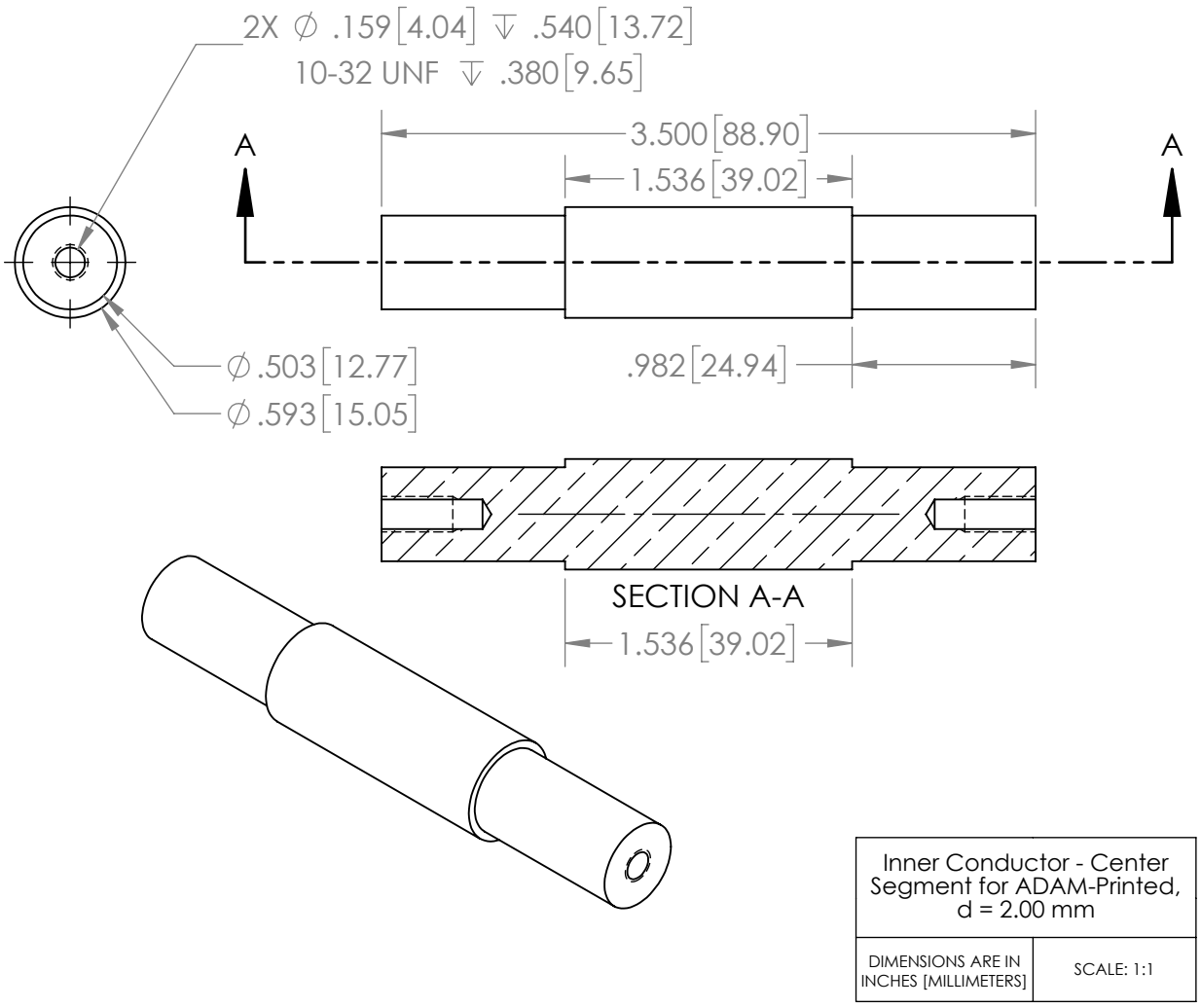

Figure C.13: Inner conductor center segment for use with the ADAM-printed outer conductor and with $d = 2.00$ mm.

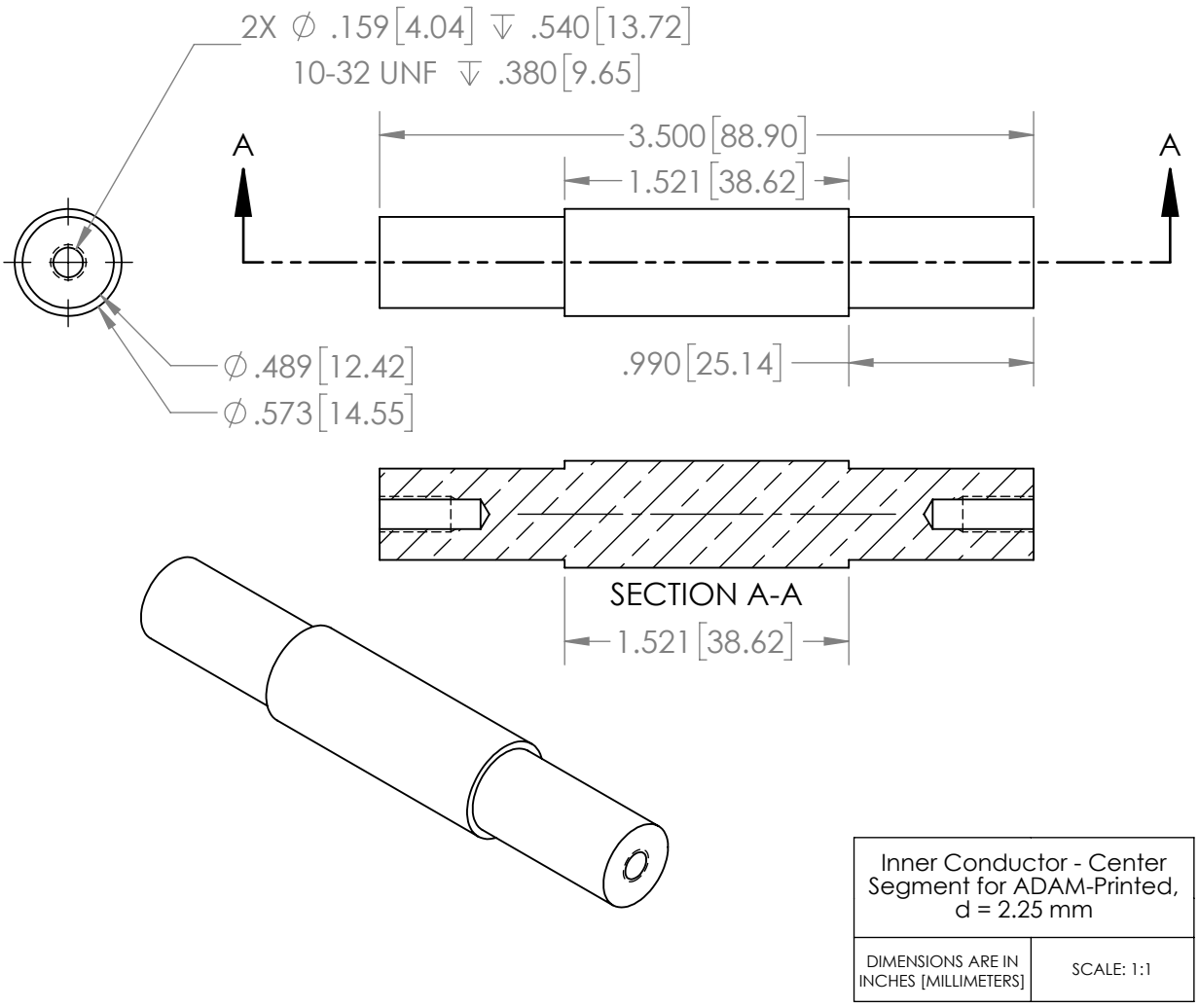

Figure C.14: Inner conductor center segment for use with the ADAM-printed outer conductor and with $d = 2.25$ mm.

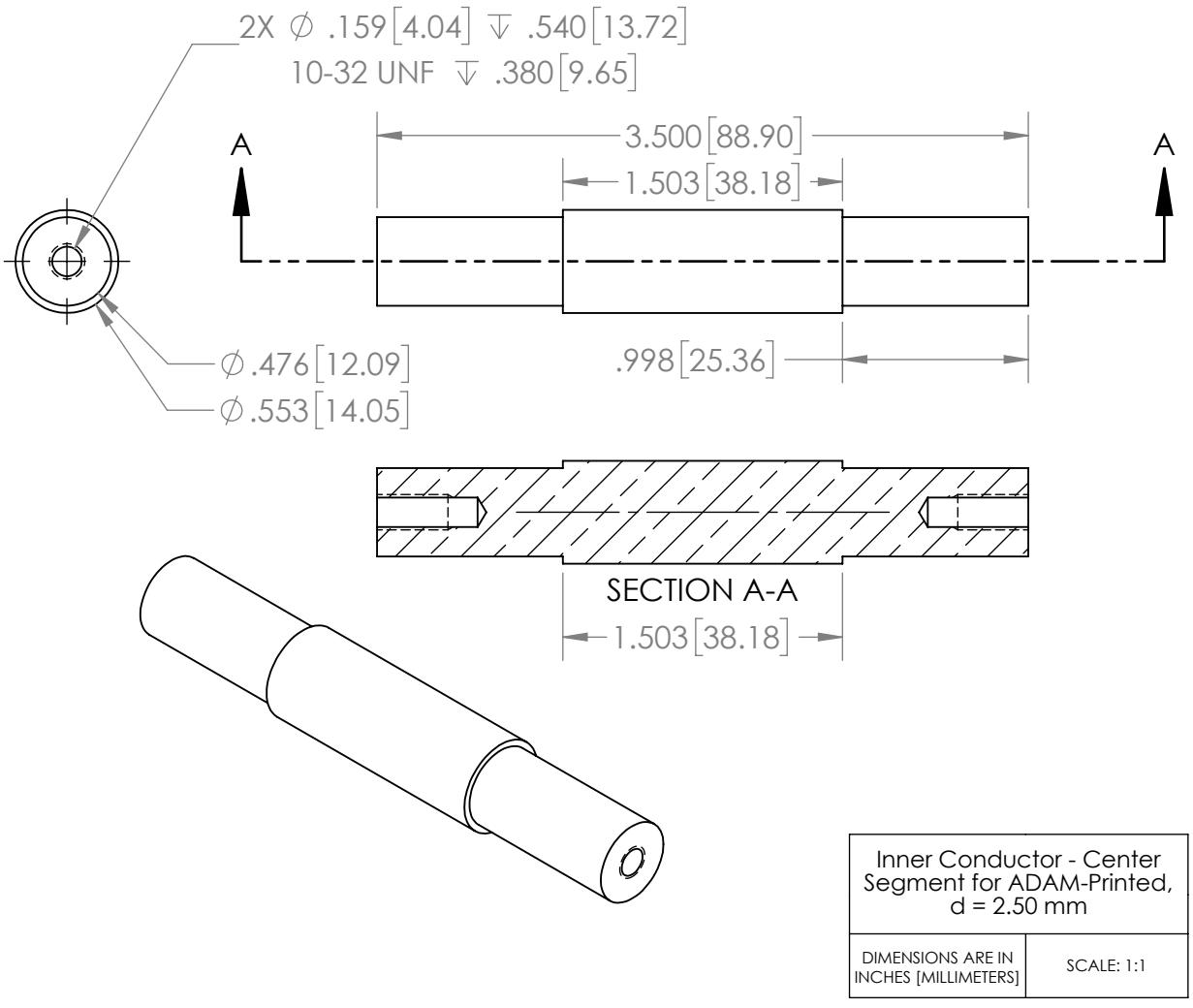

Figure C.15: Inner conductor center segment for use with the ADAM-printed outer conductor and with $d = 2.50$ mm.

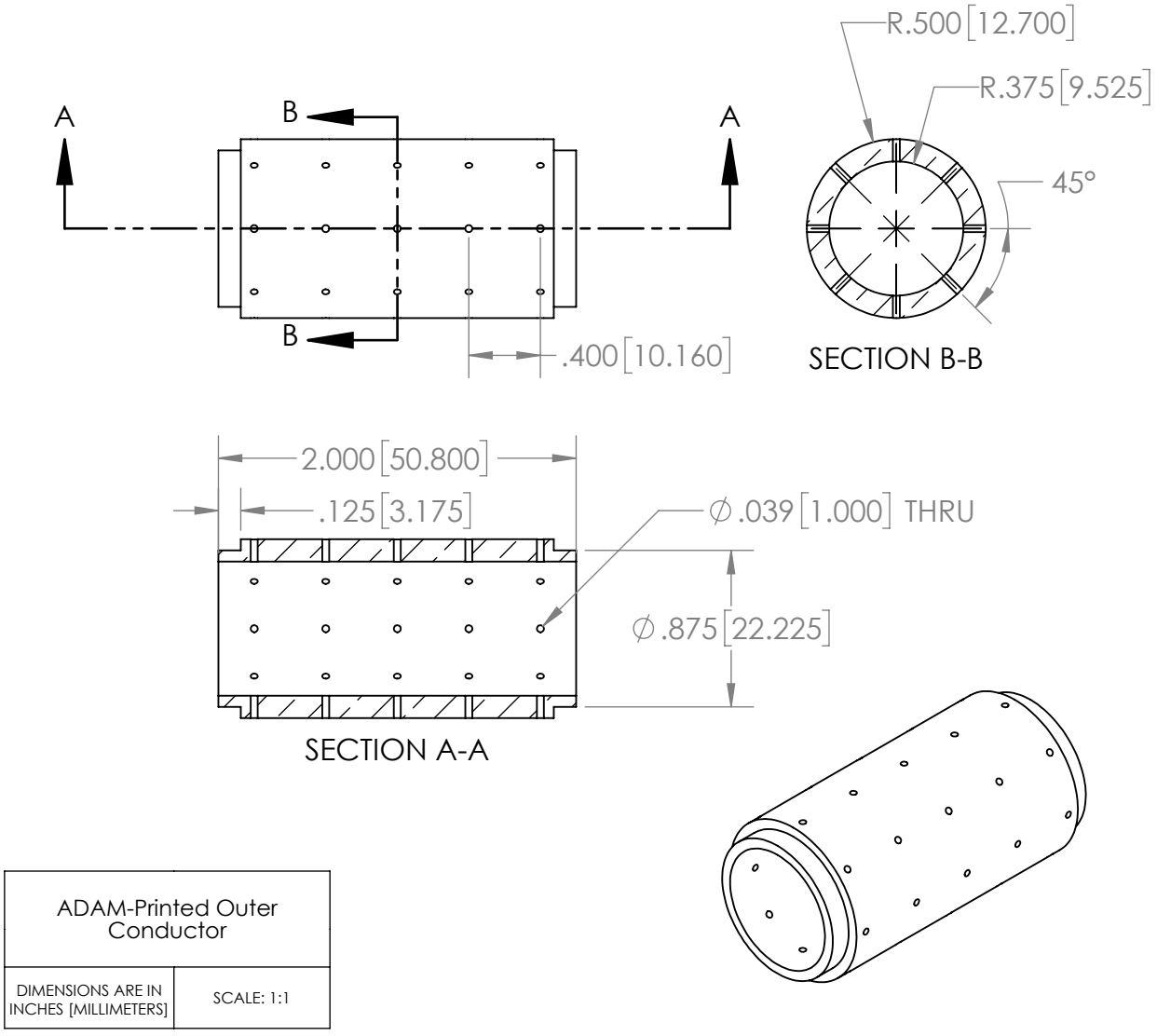

Figure C.16: ADAM-printed outer conductor.

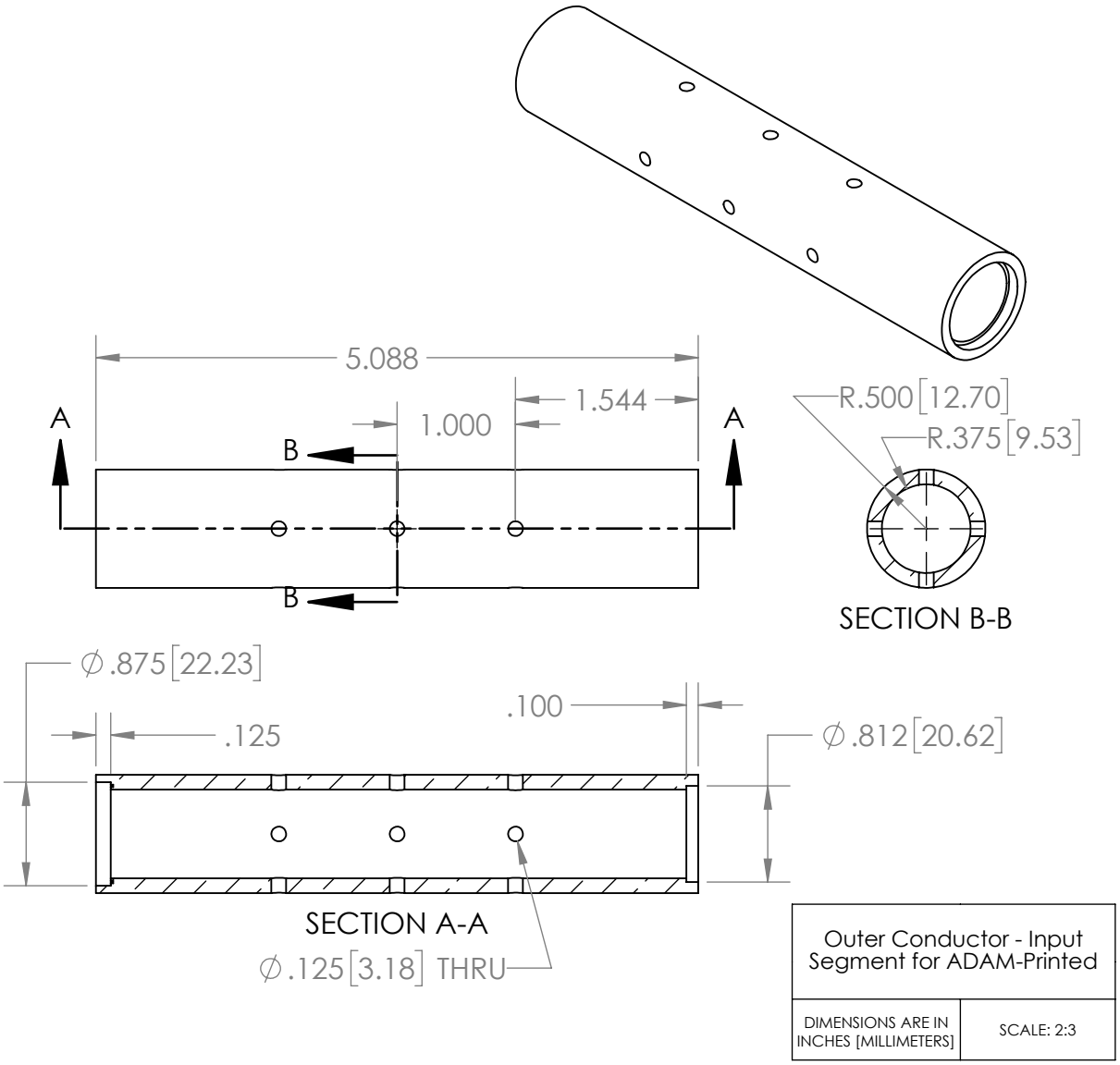

Figure C.17: Input segment for use with the ADAM-printed outer conductor.

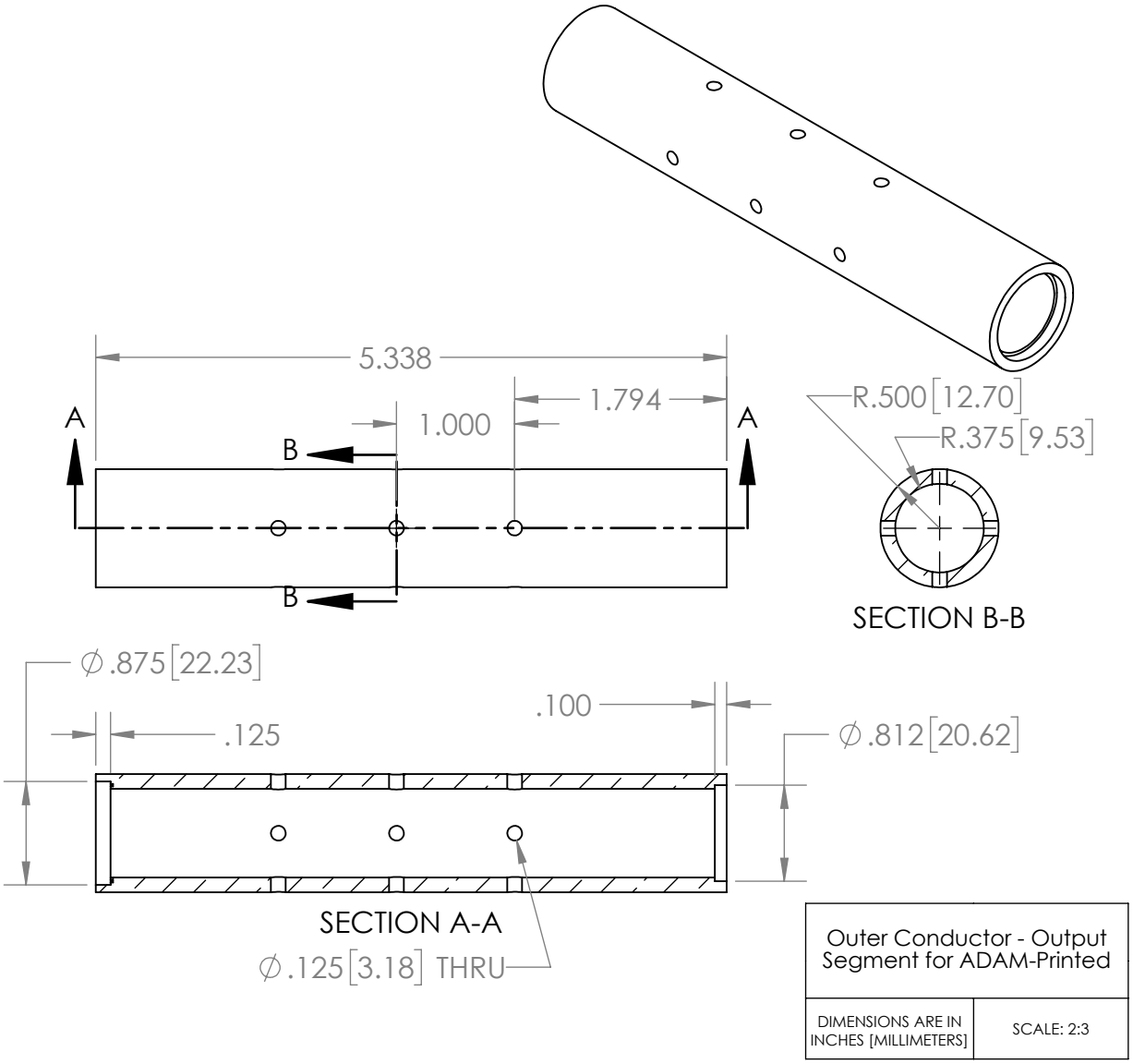

Figure C.18: Output segment for use with the ADAM-printed outer conductor.

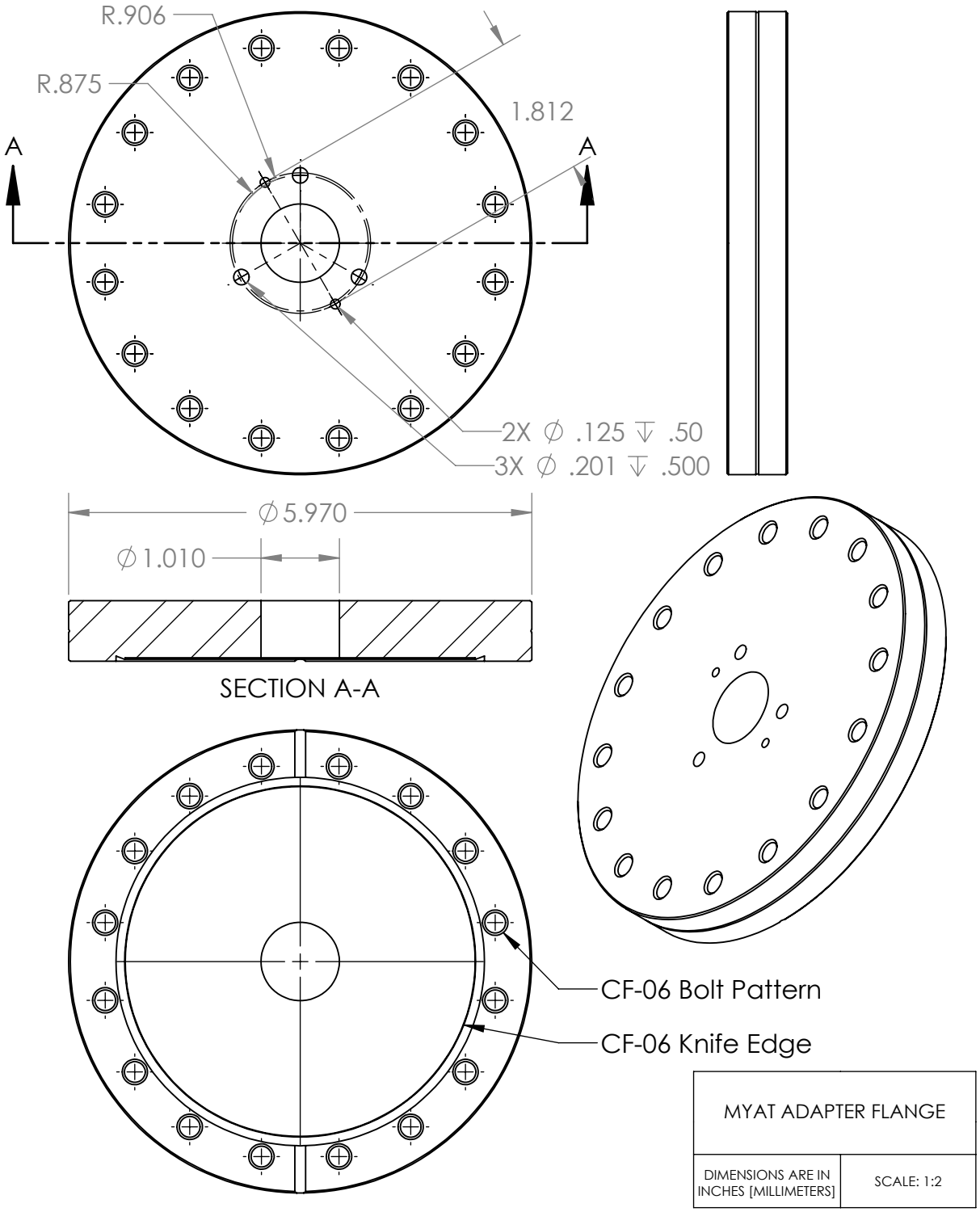

Figure C.19: MYAT adapter flange.

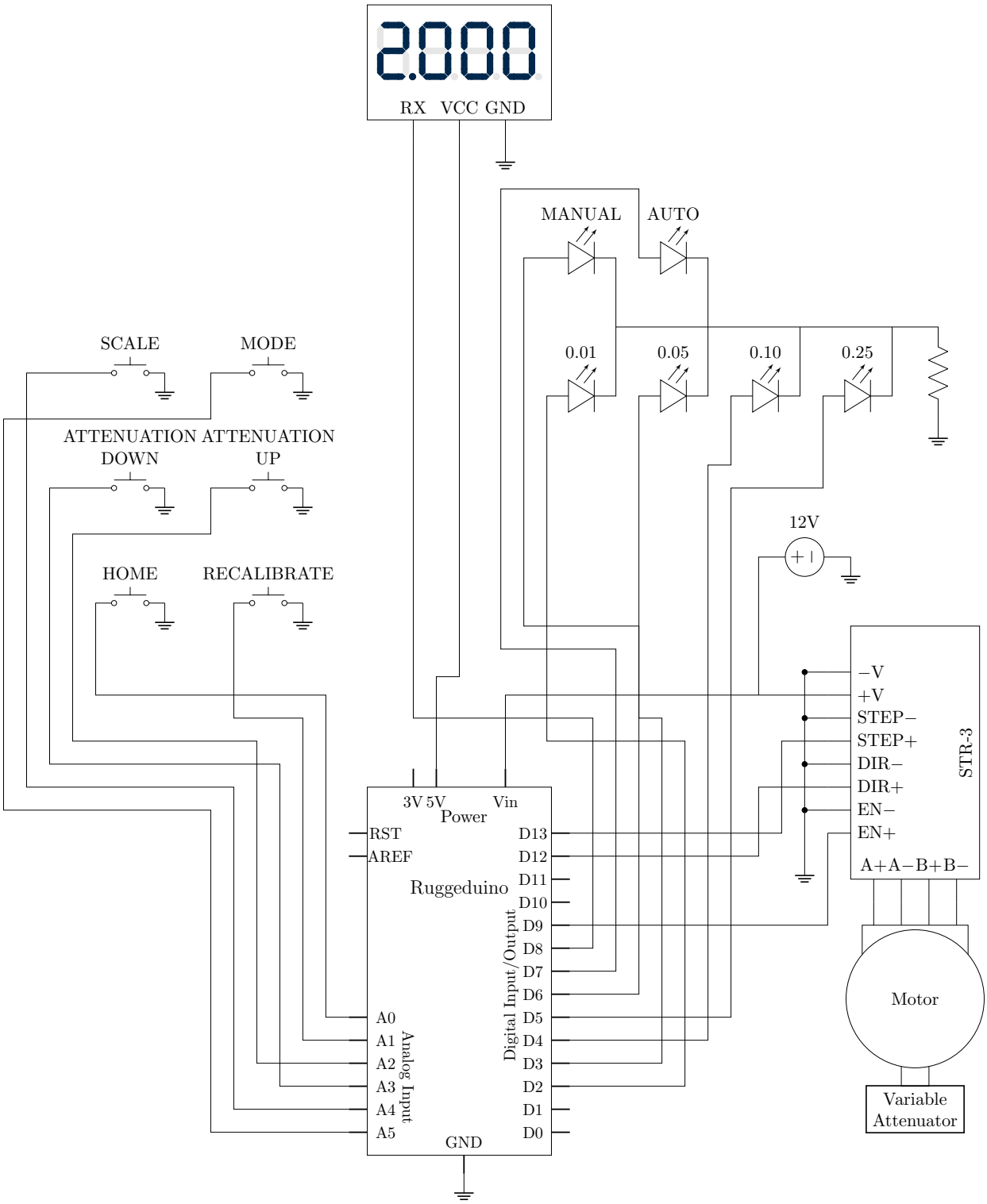

Figure C.20: Electrical schematic for the Arduino-based stepper motor controller used for adjusting the variable attenuator.

BIBLIOGRAPHY

[1] J. Vaughan, "Multipactor", *IEEE Transactions on Electron Devices*, vol. 35, no. 7, pp. 1172–1180, Jul. 1988. DOI: 10.1109/16.3387.

[2] R. A. Kishek, "Interaction of Multipactor Discharge and RF Structures", Ph.D. dissertation, University of Michigan, Ann Arbor, MI, 1997.

[3] S. Humphries, "Principles of Charged Particle Acceleration", in Mineola, NY: Dover, 1986.

[4] G. Devanz, "Multipactor simulations in superconducting cavities and power couplers", *Physical Review Special Topics - Accelerators and Beams*, vol. 4, no. 1, p. 012 001, Jan. 5, 2001. DOI: 10.1103/PhysRevSTAB.4.012001.

[5] P. Y. Wong, Y. Y. Lau, P. Zhang, N. Jordan, R. M. Gilgenbach, and J. Verboncoeur, "The effects of multipactor on the quality of a complex signal propagating in a transmission line", *Physics of Plasmas*, vol. 26, no. 11, p. 112 114, Nov. 2019. DOI: 10.1063/1.5125408.

[6] J. Vaughan, "Some high-power window failures", *IRE Transactions on Electron Devices*, vol. 8, no. 4, pp. 302–308, Jul. 1961. DOI: 10.1109/T-ED.1961.14804.

[7] D. Preist and R. Talcott, "On the heating of output windows of microwave tubes by electron bombardment", *IRE Transactions on Electron Devices*, vol. 8, no. 4, pp. 243–251, Jul. 1961. DOI: 10.1109/T-ED.1961.14797.

[8] A. J. Hatch and H. B. Williams, "The Secondary Electron Resonance Mechanism of Low-Pressure High-Frequency Gas Breakdown", *Journal of Applied Physics*, vol. 25, no. 4, pp. 417–423, Apr. 1954. DOI: 10.1063/1.1721656.

[9] A. J. Hatch and H. B. Williams, "Multipacting Modes of High-Frequency Gaseous Breakdown", *Physical Review*, vol. 112, no. 3, pp. 681–685, Nov. 1, 1958. DOI: 10.1103/PhysRev.112.681.

[10] R. Udiljak, D. Anderson, M. Lisak, V. E. Semenov, and J. Puech, "Multipactor in a coaxial transmission line. I. Analytical study", *Physics of Plasmas*, vol. 14, no. 3, p. 033 508, Mar. 2007. DOI: 10.1063/1.2710464.

[11] S. Anza, C. Vicente, J. Gil, V. E. Boria, B. Gimeno, and D. Raboso, "Nonstationary statistical theory for multipactor", *Physics of Plasmas*, vol. 17, no. 6, p. 062 110, Jun. 2010. DOI: 10.1063/1.3443128.

[12] M. Siddiqi and R. A. Kishek, "A predictive model for two-surface multipactor stability and growth based on chaos theory", *Physics of Plasmas*, vol. 26, no. 4, p. 043 104, Apr. 2019. DOI: 10.1063/1.5087586.

[13] Z. C. Shaw, A. Garcia, M. Powell, J. C. Dickens, J. J. Mankowski, and A. A. Neuber, "Direct observation of electrons in microwave vacuum components", *Review of Scientific Instruments*, vol. 90, no. 5, p. 054 702, May 2019. DOI: 10.1063/1.5089764.

[14] M. Mirmozafari, N. Behdad, and J. H. Booske, "Calculating multipactor susceptibility chart using a semi-analytic approach with improved accuracy", *Physics of Plasmas*, vol. 27, no. 11, p. 113 510, Nov. 2020. DOI: 10.1063/5.0024858.

[15] R. Woo, "Multipacting Discharges between Coaxial Electrodes", *Journal of Applied Physics*, vol. 39, no. 3, pp. 1528–1533, Feb. 15, 1968. DOI: 10.1063/1.1656390.

[16] T. P. Graves, "Experimental Investigation of Electron Multipactor Discharges at Very High Frequencies", Ph.D. dissertation, Massachusetts Institute of Technology, Cambridge, MA, 2006.

[17] D. Gonzalez-Iglesias *et al.*, "Multipactor in a Coaxial Line Under the Presence of an Axial DC Magnetic Field", *IEEE Electron Device Letters*, vol. 33, no. 5, pp. 727–729, May 2012. DOI: 10.1109/LED.2012.2186952.

[18] D. González-Iglesias *et al.*, "Multipactor Mitigation in Coaxial Lines by Means of Permanent Magnets", *IEEE Transactions on Electron Devices*, vol. 61, no. 12, pp. 4224–4231, Dec. 2014. DOI: 10.1109/TED.2014.2361172.

[19] D. Gonzalez-Iglesias, O. Monerris, B. G. Martinez, M. E. Diaz, V. E. Boria, and P. M. Iglesias, "Multipactor RF Breakdown in Coaxial Transmission Lines With Digitally Modulated Signals", *IEEE Transactions on Electron Devices*, vol. 63, no. 10, pp. 4096–4103, Oct. 2016. DOI: 10.1109/TED.2016.2596801.

[20] Y. Gómez Martínez *et al.*, "First Measurements on Multipactor Study", *Proceedings of the 12th International Particle Accelerator Conference*, vol. IPAC2021, in collab. with L. Liu (Ed.), B. M. (Ed.) John, R. Neuenschwander (Ed.), P. Renan (Ed.), and S. W. (Ed.) Volker R., 3 pages, 0.720 MB, 2021. DOI: 10.18429/JACOW-IPAC2021-WEPAB396.

[21] I. A. Kossyi *et al.*, "Experimental and numerical investigation of multipactor discharges in a coaxial waveguide", *Journal of Physics D: Applied Physics*, vol. 43, no. 34, p. 345 206, Aug. 2010. DOI: 10.1088/0022-3727/43/34/345206.

[22] S. V. Langellotti, N. M. Jordan, Y. Y. Lau, and R. M. Gilgenbach, "Multipactor experiments on an S-band coaxial test cell", *Review of Scientific Instruments*, vol. 92, no. 12, p. 124 706, Dec. 1, 2021. DOI: 10.1063/5.0074464.

[23] R. Kishek and Y. Y. Lau, "Interaction of Multipactor Discharge and rf Circuit", *Physical Review Letters*, vol. 75, no. 6, pp. 1218–1221, Aug. 7, 1995. DOI: 10.1103/PhysRevLett.75.1218.

[24] R. A. Kishek and Y. Y. Lau, "Multipactor Discharge on a Dielectric", *Physical Review Letters*, vol. 80, no. 1, pp. 193–196, Jan. 5, 1998. DOI: 10.1103/PhysRevLett.80.193.

[25] J. Vaughan, "Observations of multipactor in magnetrons", *IEEE Transactions on Electron Devices*, vol. 15, no. 11, pp. 883–889, Nov. 1968. DOI: 10.1109/T-ED.1968.16532.

[26] J. Vaughan, "A new formula for secondary emission yield", *IEEE Transactions on Electron Devices*, vol. 36, no. 9, pp. 1963–1967, Sep. 1989. DOI: 10.1109/16.34278.

[27] R. Vaughan, "Secondary emission formulas", *IEEE Transactions on Electron Devices*, vol. 40, no. 4, p. 830, Apr. 1993. DOI: 10.1109/16.202798.

[28] C. Vicente, M. Mattes, D. Wolk, H. Hartnagel, J. R. Mosig, and D. Raboso, "Contribution to the RF Breakdown in Microwave Devices and its Prediction", in *Conference Record of the 2006 Twenty-Seventh International Power Modulator Symposium*, May 2006, pp. 22–27. DOI: 10.1109/MODSYM.2006.365174.

[29] R. A. Kishek, "Ping-Pong Modes: A New Form of Multipactor", *Physical Review Letters*, vol. 108, no. 3, p. 035 003, Jan. 19, 2012. DOI: 10.1103/PhysRevLett.108.035003.

[30] R. A. Kishek, "Ping-pong modes and higher-periodicity multipactor", *Physics of Plasmas*, vol. 20, no. 5, p. 056 702, May 2013. DOI: 10.1063/1.4802838.

[31] M. Furman and M. Pivi, "Probabilistic model for the simulation of secondary electron emission", *Physical Review Special Topics - Accelerators and Beams*, vol. 5, no. 12, p. 124 404, Dec. 31, 2002. DOI: 10.1103/PhysRevSTAB.5.124404.

[32] G. Everson, *The Story of Television: The Life of Philo T. Farnsworth*. New York: Arno Press, 1974, 266 pp.

[33] P. T. Farnsworth, "Television by electron image scanning", *Journal of the Franklin Institute*, vol. 218, no. 4, pp. 411–444, Oct. 1934. DOI: 10.1016/S0016-0032(34)90415-4.

[34] R. A. Kishek, Y. Y. Lau, L. K. Ang, A. Valfells, and R. M. Gilgenbach, "Multipactor discharge on metals and dielectrics: Historical review and recent theories", *Physics of Plasmas*, vol. 5, no. 5, pp. 2120–2126, May 1998. DOI: 10.1063/1.872883.

[35] P. T. Farnsworth, "Multipactor", U.S. Patent 2 135 615, Nov. 8, 1938.

[36] P. T. Farnsworth, "Multipactor oscillator and amplifier", U.S. Patent 2 091 439, Aug. 31, 1938.

[37] P. T. Farnsworth, "Electron Multiplier", U.S. Patent 1 969 399, Aug. 7, 1934.

[38] V. Zworykin, G. Morton, and L. Malter, "The Secondary Emission Multiplier-A New Electronic Device", *Proceedings of the Institute of Radio Engineers*, vol. 24, no. 3, pp. 351–375, Mar. 1936. DOI: 10.1109/JRPROC.1936.226435.

[39] V. Zworykin and J. Rajchman, "The Electrostatic Electron Multiplier", *Proceedings of the IRE*, vol. 27, no. 9, pp. 558–566, Sep. 1939. DOI: 10.1109/JRPROC.1939.228753.

[40] J. Slepian, "Hot Cathode Tube", U.S. Patent 1 450 265, Apr. 3, 1923.

[41] K. W. Jarvis, "Electron Tube", U.S. Patent 1 903 569, Apr. 11, 1933.

[42] H. Iams and B. Salzberg, "The Secondary Emission Phototube", *Proceedings of the Institute of Radio Engineers*, vol. 23, no. 1, pp. 55–64, Jan. 1935. DOI: 10.1109/JRPROC.1935.227243.

[43] E. W. B. Gill, A. von Engel, and F. A. Lindemann, "Starting potentials of high-frequency gas discharges at low pressure", *Proceedings of the Royal Society of London. Series A. Mathematical and Physical Sciences*, vol. 192, no. 1030, pp. 446–463, Feb. 18, 1948. DOI: 10.1098/rspa.1948.0018.

[44] J. Vaughan, "Multipactor in the Brambilla grill", *Proceedings of the IEEE*, vol. 70, no. 2, pp. 203–203, Feb. 1982. DOI: 10.1109/PROC.1982.12268.

[45] S. Riyopoulos, D. Chernin, and D. Dialetis, "Theory of electron multipactor in crossed fields", *Physics of Plasmas*, vol. 2, no. 8, pp. 3194–3213, Aug. 1995. DOI: 10.1063/1.871151.

[46] S. Riyopoulos, D. Chernin, and D. Dialetis, "Effect of random secondary delay times and emission velocities in electron multipactors", *IEEE Transactions on Electron Devices*, vol. 44, no. 3, pp. 489–497, Mar. 1997. DOI: 10.1109/16.556160.

[47] R. A. Kishek and Y. Y. Lau, "A novel phase focusing mechanism in multipactor discharge", *Physics of Plasmas*, vol. 3, no. 5, pp. 1481–1483, May 1996. DOI: 10.1063/1.872027.

[48] R. B. Anderson, "Multipactor Experiment on a Dielectric Surface", Ph.D. dissertation, University of Michigan, Ann Arbor, MI, 2001.

[49] R. B. Anderson, W. D. Getty, M. L. Brake, Y. Y. Lau, R. M. Gilgenbach, and A. Valfells, "Multipactor experiment on a dielectric surface", *Review of Scientific Instruments*, vol. 72, no. 7, pp. 3095–3099, Jul. 2001. DOI: 10.1063/1.1380687.

[50] M. Berz, B. Erdélyi, and K. Makino, "Fringe field effects in small rings of large acceptance", *Physical Review Special Topics - Accelerators and Beams*, vol. 3, no. 12, p. 124 001, Dec. 6, 2000. DOI: 10.1103/PhysRevSTAB.3.124001.

[51] K. Sakamoto, Y. Ikeda, and T. Imai, "Numerical study of RF discharge caused by secondary electron emission", *Journal of Physics D: Applied Physics*, vol. 22, no. 12, p. 1840, Dec. 1989. DOI: 10.1088/0022-3727/22/12/007.

[52] T. P. Graves, B. LaBombard, S. Wukitch, and I. Hutchinson, "The coaxial multipactor experiment (CMX): A facility for investigating multipactor discharges", *Review of Scientific Instruments*, vol. 77, no. 1, p. 014 701, Jan. 2006. DOI: 10.1063/1.2162749.

[53] E. Sorolla, A. Sounas, and M. Mattes, "Space charge effects for multipactor in coaxial lines", *Physics of Plasmas*, vol. 22, no. 3, p. 033 512, Mar. 2015. DOI: 10.1063/1.4915130.

[54] P. Y. Wong, P. Zhang, J. Verboncoeur, and S. Lin, "The Effects of Angular Momentum on Multipactor in Coaxial Lines", in *2021 22nd International Vacuum Electronics Conference (IVEC)*, Apr. 2021, pp. 1–2. DOI: 10.1109/IVEC51707.2021.9722464.

[55] S. Lin *et al.*, "Multipactor threshold calculation of coaxial transmission lines in microwave applications with nonstationary statistical theory", *Physics of Plasmas*, vol. 22, no. 8, p. 082 114, Aug. 2015. DOI: 10.1063/1.4928421.

[56] M. Siddiqi and R. Kishek, "A Predictive Model for Multipactor Discharge in Coaxial Systems Based on Chaos Theory", *IEEE Transactions on Electron Devices*, vol. 66, no. 10, pp. 4403–4407, Oct. 2019. DOI: 10.1109/TED.2019.2934457.

[57] M. Siddiqi and R. Kishek, "Map-Based Multipactor Theory for Cross-Field Devices", *IEEE Transactions on Electron Devices*, vol. 66, no. 7, pp. 3162–3167, Jul. 2019. DOI: 10.1109/TED.2019.2914343.

[58] M. Siddiqi and R. Kishek, "A Model for Multipactor Discharge on a Dielectric Based on Chaos Theory", *IEEE Transactions on Electron Devices*, vol. 66, no. 10, pp. 4387–4391, Oct. 2019. DOI: 10.1109/TED.2019.2932878.

[59] M. Siddiqi and R. Kishek, "Construction of Multipactor Susceptibility Diagrams From Map-Based Theory", *IEEE Transactions on Electron Devices*, vol. 66, no. 8, pp. 3587–3591, Aug. 2019. DOI: 10.1109/TED.2019.2922147.

[60] M. Siddiqi and R. A. Kishek, "A predictive model for long-term multipactor discharge under two-carrier operation based on chaos theory", *Physics of Plasmas*, vol. 26, no. 11, p. 113 111, Nov. 2019. DOI: 10.1063/1.5126275.

[61] M. Siddiqi, "Application of Map-Based Multipactor Theory to Alternate Periodic Radio Frequency Waveforms", *IEEE Transactions on Plasma Science*, vol. 48, no. 9, pp. 3083–3087, Sep. 2020. DOI: 10.1109/TPS.2020.3014187.

[62] M. Mirmozafari, N. Behdad, and J. H. Booske, "Ultrawideband, high-power, microstripline test setup for experimental study and characterization of multipactor", *Review of Scientific Instruments*, vol. 92, no. 8, p. 084 706, Aug. 1, 2021. DOI: 10.1063/5.0058049.

[63] R. E. Gutierrez, I. Matanovic, M. P. Polak, R. S. Johnson, D. Morgan, and E. Schamiloglu, "First principles inelastic mean free paths coupled with Monte Carlo simulation of secondary electron yield of Cu-Ni, Cu-Zn, and Mo-Li", *Journal of Applied Physics*, vol. 129, no. 17, p. 175 105, May 7, 2021. DOI: 10.1063/5.0049522.

[64] M. P. Polak and D. Morgan, "MAST-SEY: MAterial Simulation Toolkit for Secondary Electron Yield. A monte carlo approach to secondary electron emission based on complex dielectric functions", *Computational Materials Science*, vol. 193, p. 110 281, Jun. 1, 2021. DOI: 10.1016/j.commatsci.2021.110281.

[65] A. Iqbal, J. Verboncoeur, and P. Zhang, "Two surface multipactor discharge with two-frequency rf fields and space-charge effects", *Physics of Plasmas*, vol. 29, no. 1, p. 012 102, Jan. 2022. DOI: 10.1063/5.0070889.

[66] D.-Q. Wen, A. Iqbal, P. Zhang, and J. P. Verboncoeur, "Suppression of single-surface multipactor discharges due to non-sinusoidal transverse electric field", *Physics of Plasmas*, vol. 26, no. 9, p. 093 503, Sep. 2019. DOI: 10.1063/1.5111734.

[67] D. Li, P. Y. Wong, D. Chernin, and Y. Y. Lau, "Induced Current Due to Electromagnetic Shock Produced by Charge Impact on a Conducting Surface", *IEEE Transactions on Plasma Science*, vol. 50, no. 9, pp. 2838–2844, Sep. 2022. DOI: 10.1109/TPS.2022.3187667.

[68] S. V. Langellotti, N. M. Jordan, Y. Y. Lau, and R. M. Gilgenbach, "CST Particle Studio Simulations of Coaxial Multipactor and Comparison With Experiments", *IEEE Transactions on Plasma Science*, vol. 48, no. 6, pp. 1942–1949, Jun. 2020. DOI: 10.1109/TPS.2020.2981257.

[69] V. E. Semenov, N. Zharova, R. Udiljak, D. Anderson, M. Lisak, and J. Puech, "Multipactor in a coaxial transmission line. II. Particle-in-cell simulations", *Physics of Plasmas*, vol. 14, no. 3, p. 033 509, Mar. 2007. DOI: 10.1063/1.2710466.

[70] S. Yamaguchi, Y. Saito, S. Anami, and S. Michizono, "Trajectory simulation of multipactoring electrons in an S-band pillbox RF window", *IEEE Transactions on Nuclear Science*, vol. 39, no. 2, pp. 278–282, Apr. 1992. DOI: 10.1109/23.277497.

[71] V. E. Semenov, E. I. Rakova, D. Anderson, M. Lisak, and J. Puech, "Importance of Reflection of Low-Energy Electrons on Multipactor Susceptibility Diagrams for Narrow Gaps", *IEEE Transactions on Plasma Science*, vol. 37, no. 9, pp. 1774–1781, Sep. 2009. DOI: 10.1109/TPS.2009.2026754.

[72] Y. Y. Lau, "Fluid description of kinetic modes", *Physics of Plasmas*, vol. 1, no. 9, pp. 2816–2821, Sep. 1994. DOI: 10.1063/1.870930.

[73] M. Angelucci, A. Novelli, L. Spallino, A. Liedl, R. Larciprete, and R. Cimino, "Minimum thickness of carbon coating for multipacting suppression", *Physical Review Research*, vol. 2, no. 3, p. 032 030, Aug. 4, 2020. DOI: 10.1103/PhysRevResearch.2.032030.

[74] A. Hatch, "Suppression of multipacting in particle accelerators", *Nuclear Instruments and Methods*, vol. 41, no. 2, pp. 261–271, May 1966. DOI: 10.1016/0029-554X(66)90010-3.

[75] Y. Saito, S. Michizono, S. Anami, and S. Kobayashi, "Surface flashover on alumina RF windows for high-power use", *IEEE Transactions on Electrical Insulation*, vol. 28, no. 4, pp. 566–573, Aug. 1993. DOI: 10.1109/14.231539.

[76] D. Wu *et al.*, "Fabrication of Porous Ag/TiO2/Au Coatings with Excellent Multipactor Suppression", *Scientific Reports*, vol. 7, no. 1, p. 43 749, Mar. 2017. DOI: 10.1038/srep43749.

[77] E. Al Hajj Sleiman, J. Hillairet, M. Belhaj, and S. Dadouch, "Evaluation of multipactor thresholds for coaxial lines subject to surface conditioning for the WEST ion cyclotron antenna", *Fusion Engineering and Design*, vol. 185, p. 113 325, Dec. 1, 2022. DOI: 10.1016/j.fusengdes.2022.113325.

[78] C. Chang, G. Z. Liu, C. X. Tang, C. H. Chen, H. Shao, and W. H. Huang, "Suppression of high-power microwave dielectric multipactor by resonant magnetic field", *Applied Physics Letters*, vol. 96, no. 11, p. 111 502, Mar. 15, 2010. DOI: 10.1063/1.3360853.

[79] R. L. Geng, H. Padamsee, S. Belomestnykh, P. Goudket, D. M. Dykes, and R. G. Carter, "Suppression of multipacting in rectangular coupler waveguides", *Nuclear Instruments and Methods in Physics Research Section A: Accelerators, Spectrometers, Detectors and Associated Equipment*, vol. 508, no. 3, pp. 227–238, Aug. 11, 2003. DOI: 10.1016/S0168-9002(03)01660-7.

[80] C. Jing *et al.*, "Observation of multipactor suppression in a dielectric-loaded accelerating structure using an applied axial magnetic field", *Applied Physics Letters*, vol. 103, no. 21, p. 213 503, Nov. 18, 2013. DOI: 10.1063/1.4832326.

[81] X. Zhang, Y. Xiao, and B. Gimeno, "Multipactor Suppression by a Resonant Static Magnetic Field on a Dielectric Surface", *IEEE Transactions on Electron Devices*, vol. 67, no. 12, pp. 5723–5728, Dec. 2020. DOI: 10.1109/TED.2020.3027271.

[82] V. Semenov, A. Kryazhev, D. Anderson, and M. Lisak, "Multipactor suppression in amplitude modulated radio frequency fields", *Physics of Plasmas*, vol. 8, no. 11, pp. 5034–5039, Nov. 2001. DOI: 10.1063/1.1410980.

[83] W.-Z. Cui *et al.*, "An efficient multipaction suppression method in microwave components for space application", *Chinese Physics B*, vol. 25, no. 6, p. 068 401, Jun. 2016. DOI: 10.1088/1674-1056/25/6/068401.

[84] C. Chang, G. Z. Liu, H. J. Huang, C. H. Chen, and J. Y. Fang, "Suppressing high-power microwave dielectric multipactor by the sawtooth surface", *Physics of Plasmas*, vol. 16, no. 8, p. 083 501, Aug. 2009. DOI: 10.1063/1.3200900.

[85] D. Wright, Z. C. Shaw, J. J. Mankowski, J. C. Dickens, J. Stephens, and A. A. Neuber, "Multipactor suppression via asymmetric grooves in S-band waveguide", *Physics of Plasmas*, vol. 29, no. 6, p. 063 108, Jun. 2022. DOI: 10.1063/5.0094591.

[86] M. Ye *et al.*, "Suppression of secondary electron yield by micro-porous array structure", *Journal of Applied Physics*, vol. 113, no. 7, p. 074 904, Feb. 21, 2013. DOI: 10.1063/1.4792514.

[87] M. Ye *et al.*, "Investigation into anomalous total secondary electron yield for micro-porous Ag surface under oblique incidence conditions", *Journal of Applied Physics*, vol. 114, no. 10, p. 104 905, Sep. 14, 2013. DOI: 10.1063/1.4821138.

[88] M. Ye, Y. Li, Y. He, and M. Daneshmand, "Study of multipactor suppression of microwave components using perforated waveguide technology for space applications", *Physics of Plasmas*, vol. 24, no. 5, p. 052 109, May 2017. DOI: 10.1063/1.4982665.

[89] E. D. Weber, M. Mirmozafari, N. Behdad, and J. H. Booske, "Experimental Verification of Multipactor Suppression in Microstripline Using High Porosity Surfaces", *IEEE Transactions on Plasma Science*, vol. 50, no. 1, pp. 43–49, Jan. 2022. DOI: 10.1109/TPS.2021.3134493.

[90] N. Fil, M. Belhaj, J. Hillairet, and J. Puech, "Multipactor threshold sensitivity to total electron emission yield in small gap waveguide structure and TEEY models accuracy", *Physics of Plasmas*, vol. 23, no. 12, p. 123 118, Dec. 2016. DOI: 10.1063/1.4972571.

[91] Dassault Systems, *CST Studio Suite 2020 Help*. 2020.

[92] I. Bojko, N. Hilleret, and C. Scheuerlein, "Influence of air exposures and thermal treatments on the secondary electron yield of copper", *Journal of Vacuum Science & Technology A: Vacuum, Surfaces, and Films*, vol. 18, no. 3, pp. 972–979, May 2000. DOI: 10.1116/1.582286.

[93] D. M. Pozar, *Microwave Engineering*, 4th ed. Hoboken, NJ: Wiley, 2012, 732 pp.

[94] G. Greening, "Multi-Frequency Recirculating Planar Magnetrons", Ph.D. dissertation, University of Michigan, Ann Arbor, MI, 2017.

[95] R. G. Wilson, "Vacuum Thermionic Work Functions of Polycrystalline Be, Ti, Cr, Fe, Ni, Cu, Pt, and Type 304 Stainless Steel", *Journal of Applied Physics*, vol. 37, no. 6, pp. 2261–2267, May 1966. DOI: 10.1063/1.1708797.

[96] D. Raboso and A. Woode, "A new method of electron seeding used for accurate testing of multipactor transients", in *25th European Microwave Conference, 1995*, Bologna, Italy: IEEE, Oct. 1995, pp. 190–193. DOI: 10.1109/EUMA.1995.336944.

[97] M. S. Shur and R. Gaska, "Deep-Ultraviolet Light-Emitting Diodes", *IEEE Transactions on Electron Devices*, vol. 57, no. 1, pp. 12–25, Jan. 2010. DOI: 10.1109/TED.2009.2033768.

[98] G. K. Christiansen, "Toy building brick", U.S. Patent 3 005 282, Oct. 1961.

[99] C. N. Berglund and W. E. Spicer, "Photoemission Studies of Copper and Silver: Experiment", *Physical Review*, vol. 136, A1044–A1064, 4A Nov. 16, 1964. DOI: 10.1103/PhysRev.136.A1044.

[100] S. N. Sami, L. Diaz, M. Sanati, and R. P. Joshi, "Simulations of field emission from copper electrodes with inclusion of oxygen surface layer and work function changes based on first-principles calculations", *Journal of Applied Physics*, vol. 128, no. 22, p. 223 302, Dec. 14, 2020. DOI: 10.1063/5.0031568.

[101] A. S. Sakharov, V. A. Ivanov, Y. A. Tarbeeva, and M. E. Konyzhev, "Theoretical and experimental study of microwave power absorption by a single-sided multipactor discharge on a dielectric", *Plasma Physics Reports*, vol. 38, no. 13, pp. 1090–1098, Dec. 2012. DOI: 10.1134/S1063780X12080235.

[102] M. A. Lieberman and A. J. Lichtenberg, *Principles of Plasma Discharges and Materials Processing*, 2nd ed. Hoboken, N.J: Wiley-Interscience, 2005, 757 pp.

[103] M. Pivi, F. K. King, R. E. Kirby, T. O. Raubenheimer, G. Stupakov, and F. Le Pimpec, "Sharp reduction of the secondary electron emission yield from grooved surfaces", *Journal of Applied Physics*, vol. 104, no. 10, p. 104 904, Nov. 15, 2008. DOI: 10.1063/1.3021149.

[104] "MIL-STD-348", Department of Defense, Apr. 20, 1988.

[105] C. Y. Yap *et al.*, "Review of selective laser melting: Materials and applications", *Applied Physics Reviews*, vol. 2, no. 4, p. 041 101, Dec. 2015. DOI: 10.1063/1.4935926.

[106] "The Evolution of an Idea: A Brief Typology of 3D Printing", in *3D Printing*. The MIT Press, 2019. DOI: 10.7551/mitpress/11800.003.0006.

[107] F. Caiazzo, S. L. Campanelli, F. Cardaropoli, N. Contuzzi, V. Sergi, and A. D. Ludovico, "Manufacturing and characterization of similar to foam steel components processed through selective laser melting", *The International Journal of Advanced Manufacturing Technology*, vol. 92, no. 5, pp. 2121–2130, Sep. 1, 2017. DOI: 10.1007/s00170-017-0311-4.

[108] T. Q. Tran *et al.*, "3D Printing of Highly Pure Copper", *Metals*, vol. 9, no. 7, p. 756, 7 Jul. 2019. DOI: 10.3390/met9070756.

[109] E. P. Bertin, *Introduction to X-Ray Spectrometric Analysis*. Boston, MA: Springer US, 1978. DOI: 10.1007/978-1-4899-2204-5.

[110] M. Galati and P. Minetola, "Analysis of Density, Roughness, and Accuracy of the Atomic Diffusion Additive Manufacturing (ADAM) Process for Metal Parts", *Materials*, vol. 12, no. 24, p. 4122, 24 Jan. 2019. DOI: 10.3390/ma12244122.

[111] "Copper Material Datasheet, Rev. 1.1", Markforged, Jan. 15, 2022. [Online]. Available: https://www-objects.markforged.com/craft/materials/Copper-V1.1.pdf.

[112] J. Kawata, K. Ohya, and K. Nishimura, "Simulation of secondary electron emission from rough surfaces", *Journal of Nuclear Materials*, Plasma-Surface Interactions in Controlled Fusion Devices, vol. 220–222, pp. 997–1000, Apr. 1, 1995. DOI: 10.1016/0022-3115(94)00460-9.

[113] H. Seiler, "Secondary electron emission in the scanning electron microscope", *Journal of Applied Physics*, vol. 54, no. 11, R1–R18, Nov. 1983. DOI: 10.1063/1.332840.

[114] P. Shirley and R. K. Morley, *Realistic Ray Tracing*, 2nd ed. Natick, Mass: AK Peters, 2003, 225 pp.

[115] A. S. Gilmour, *Klystrons, Traveling Wave Tubes, Magnetrons, Crossed-Field Amplifiers, and Gyrotrons* (Artech House Microwave Library). Boston, MA: Artech House, 2011, 859 pp.

[116] S. Anza, C. Vicente, J. Gil, V. E. Boria, and D. Raboso, "Experimental verification of multipactor prediction methods in multicarrier systems", in *2016 46th European Microwave Conference (EuMC)*, London, United Kingdom: IEEE, Oct. 2016, pp. 226–229. DOI: 10.1109/EuMC.2016.7824319.

[117] S. C. Exelby, "Recirculating Planar Crossed-Field Amplifiers", Ph.D. dissertation, University of Michigan, Ann Arbor, MI, 2019.

[118] "Agilent 423B, 8470B, 8472B, 8473B/C Low Barrier Schottky Diode Detectors", Agilent Technologies, Oct. 18, 2013.